# NANOSTRUCTURED $Co_{1-x}Ni_x$ LAYERED DOUBLE HYDROXIDES AS ELECTRODE MATERIAL FOR REDOX SUPERCAPACITORS

A THESIS SUBMITTED TO

**SHIVAJI UNIVERSITY, KOLHAPUR**

FOR THE DEGREE OF

**DOCTOR OF PHILOSOPHY**

IN

**PHYSICS**

UNDER THE FACULTY OF SCIENCE

BY

**Mr. SACHIN BABASAHEB KULKARNI**

M.Sc.

UNDER THE GUIDANCE OF

**Prof. C. D. LOKHANDE**

M.Sc., Ph.D.

**DEPARTMENT OF PHYSICS,**

**SHIVAJI UNIVERSITY,**

**KOLHAPUR-416 004**

**INDIA.**

**2011**

## *DECLARATION*

*I hereby declare that, the thesis entitled "**NANOSTRUCTURED $Co_{1-x}Ni_x$ LAYERED DOUBLE HYDROXIDES AS ELECTRODE MATERIAL FOR REDOX SUPERCAPACITORS**" submitted for the award of degree of **Doctor of Philosophy** in the faculty of Science of the Shivaji University, Kolhapur is completed and written by me, has not previously formed the basis for the award of any Degree or Diploma or other similar title of this or any other University or examining body to the best of my knowledge.*

*Place: Kolhapur*

*Date:* 16/09/2011

*Mr. Sachin Babasaheb Kulkarni*

*Research Student*

***SHIVAJI UNIVERSITY***

***DEPARTMENT OF PHYSICS***

## *CERTIFICATE*

*This is to certify that, the thesis entitled "**NANOSTRUCTURED $Co_{1-x}Ni_x$ LAYERED DOUBLE HYDROXIDES AS ELECTRODE MATERIAL FOR REDOX SUPERCAPACITORS**" which is being submitted herewith for the award of the **Degree of Doctor of Philosophy** in **Physics** of Shivaji University, Kolhapur, is the result of the original research work completed by **Mr. Sachin Babasaheb Kulkarni** under my supervision and guidance and to the best of my knowledge and belief the work embodied in this thesis has not formed earlier the basis for the award of any Degree of similar title of this or any other university or examining body.*

*Place: Kolhapur*

*Date:* 16/09/2011

*Research Guide*

**Prof. C. D. Lokhande**

*Department of Physics,*

*Shivaji University,*

*Kolhapur.*

*Forwarded through,*

Dr. C. H. Bhosale
Prof. & Head
Department of Physics,
Shivaji University,
KOLHAPUR.

*Head,*

*Department of Physics,*

*Shivaji University,*

*Kolhapur.*

# Dedicated To.....

॥ मातृ देवो भव: ॥ ॥ पितृ देवो भव: ॥ ॥ आचार्य देवो भव: ॥

Beloved Sir

&

My Dear Aai-Pappa.

## Acknowledgement

*According to saying, "Silent Things Are More Sound"; this part furnishes me the way of expressing heart feeling appreciations. How I can introduce and thank with deep sense to the unique & genius personality, my beloved research guide, respectable Prof. C. D. Lokhande (SIR). It was truly an immensive experience to work with and to learn many more things from our SIR. I salute him for his unbroken confidence, moral faith of true guidance and deep quest for scientific knowledge. I express huge gratitude to him not only for the research guidance granted during my Ph.D. course but also for shaping and enlightening the path of my life with deep care, strictness, love, affection, partial anger along with huge humanity by his stunning advises. I am indisputably very much fortunate to have him as my Ph.D. guide. With his kind support in educational, economical and social stages, I could overcome my personal and scientific troubles. I truly appreciated him for still offering an excellent, energetic youthful concert in research. This work could not have been completed without his inspiring guidance and continuous encouragement during the course of research tenure.*

*I would like to express my sincere thanks to Dr. C. H. Bhosale, Professor and Head, Department of Physics, Shivaji University, Kolhapur for his encouragement for making me available the laboratory facility.*

*I am thankful to Prof. N. J. Pawar (Vice-Chancellor SUK) and Prof. M. M. Salunkhe (Ex. Vice-Chancellor SUK), teaching and non- teaching staff of the Physics Department and all the members of C.F.C. and U.S.I.C., Shivaji University, Kolhapur for their help during the research work.*

*Exceptional thanks goes to Dr. (Mrs) S.S. Joshi for many brainstorming sessions & familiar support. Also, I wish to thank Dr. V. J. Fulari, Dr. P. S. Patil, Dr. K. Y. Rajpure and Dr. S. D. Lotake for their many insightful suggestions and support throughout my research. I would like to express sincere thanks to, Dr. T.P. Gujar and Dr. (Mrs.) V.R. Shinde, for insightful guidelines and precious help for the current work so that I have achieved this goal.*

*Good scientific research could not flourish in an alienated desert; it is a result of fruitful discussions and supportive exercises of many logical minds. I thank Dr. J.L. Gunjakar, Dr. A.M. More, Dr. R.R. Salunkhe along with Dr. U. M. Patil especially, who helped me to analyze the results with all their empathy and supportive mind. I am thankful for the fabulous support provided by Dr. S. D. Sartale, Dr. B. R. Sankapal, Dr. H. M. Pathan, Dr. R. B. Kale, Dr. V. D. Patake, Dr. S. G. Kandalkar Dr. K. V. Gurav, Dr. D. S. Dhawale and Dr. D. P. Dubal during my research work.*

*I am appreciative to my colleagues, Ajju, Prashant, Nanaso, Sandip, Vinayak, Miss. Swati, Mr. B. B. Rajeshaikh and all research scholars of the Physics Department for their constant encouragement during my research work. I would like to extend my thanks to seniors Nilesh, Sharad, Sachin (Kd) and Manik sir for timely and precious help. It gives me immense pleasure to convey admiration to my dearest friends Aniket, Somnath (Barakya), Sopanrao (SP), Rama, Anand, Shivaji, Suraj, Appa, Pravin (Pr.), Vikas (CEO), Makarand (Mak), Yogesh, Prakash (Golu), Shitalu, Mahendra (Mahi), Vinayak (Prl), Sachin, Nama and Sitaram (Maharaj) for their unforgettable and spectacular patronage along with all my juniors who helped me with all possible ways during my work.*

*Special thank are retained for Dr. B. R. Karche H.O.D physics, Akluj college for his constant, appropriate and enthusiastic moral support which made my path easier to tread.*

*I hereby articulate my innermost honest appreciation and regards to my dearly loving "Aai-Pappa". My cordial acknowledgment goes to my simple-straightforward father, caring mother, dear SandipDa-Dipali vahini with little Yashraj (Pilu) for unutterable things. Also, I thankful to all my family members, who continuously supported and encouraged me to complete my research.*

*Last and most momentous; I dedicate this work to my beloved "SIR" and my dear "Aai-Pappa".*

*$@chin*

# Summary of Research Work

## List of Publications

### A) Patents

1 Synthesis of Supercapacitive Polyaniline Thin Film Electrodes Deposited on Large Scale Area by Bottom-Up Approached Lucrative SILAR Method ***Indian patent.***

### B) Reasearch papers published/accepted/submitted to the cited national/international Journals

1 "Synthesis and characterization of b-Ni(OH)2 up grown nanoflakes by SILAR method."
**S.B. Kulkarni**, V.S. Jamadade, D.S. Dhawale, C.D. Lokhande*
**Applied Surface Science 255 (2009) 8390–8394.**

2 "Facile and efficient route for preparation of nanostructured polyaniline thin films: Schematic model for simplest oxidative chemical polymerization."
**S.B. Kulkarni**, S.S. Joshi, C.D. Lokhande*
**Chemical Engineering Journal 166 (2011) 1179–1185**.

3 "Temperature impact on morphological evolution of ZnO and its consequent effect on physico-chemical properties."
**S.B. Kulkarni**, U.M. Patil, R.R. Salunkhe, S.S. Joshi, C.D. Lokhande*
**Journal of Alloys and Compounds 509 (2011) 3486–3492**.

4 "Chemically synthesized hydrous RuO2 thin films for supercapacitor application."
U.M. Patil, **S.B. Kulkarni**, V.S. Jamadade, C.D. Lokhande*,
**Journal of Alloys and Compounds 509 (2011) 1677-1682.**

5 "Photosensitive nanostructured TiO2 grown at room temperature by novel "bottom-up" approached CBD method."

U.M. Patil, **S.B. Kulkarni**, P.R. Deshmukh, R.R. Salunkhe, C.D. Lokhande*

**Journal of Alloys and Compounds 509 ( 2011) 6196-6199.**

6 "Potentiodynamically deposited $Co_{1-x}Ni_x$ LDHs as redox electrode for supercapacitors."

**S.B. Kulkarni**, A. D. Jagadale, S.S. Joshi, C.D. Lokhande*

**Electroanalytical chemistry (submitted)**

7 "Synthesis and characterization of $Co_{1-x}Ni_x$ LDHs thin films by potentiostatic mode : Supercapacitors."

**S.B. Kulkarni**, A. D. Jagadale, S.S. Joshi, C.D. Lokhande*

**Electrochimica Acta (submitted)**

8 "Galvanostatically deposited Co-Ni layered double hydroxides as redox supercapacitor electrodes."

**S.B. Kulkarni**, A. D. Jagadale, S.S. Joshi, C.D. Lokhande*

**Electrochemistry communication (submitted)**

9 "Room Temperature Synthesis of Inorganic Metal Oxide-Organic Conducting Polymer (ZnO/PANI) Nanocomposites via Simple Solution Route."

**S.B. Kulkarni**, U. M. Patil, S. S. Joshi, C.D. Lokhande1*

**Journal of Alloys and Compounds(submitted)**

## C) Paper presented /accepted at national/International Conferences/Meetings/Seminar/Sympoysia

1 "Direct growth of β-Ni(OH)2 nanoflakes on the substrate surface by SILAR method."

**S.B. Kulkarni**, P.R. Deshmukh, V.S. Jamdade, D.S. Dhawale, U.M. Patil, C.D. Lokhande*

Poster presentation NCANDT-2009, 11-12$^{th}$ July, 2009.

2 “Chemically prepared nickel iron oxyhydroxide thin films on flexible foil for supercapacitor application.”

V.S. Jamadade, **S.B. Kulkarni**, U.M. Patil, J.L Gunjakar, C.D. Lokhande*

Poster presentation NCANDT-2009, 11-12th July, 2009.

3 “Synthesis and characterization of nickel hydroxide by chemical method.”

**S.B. Kulkarni**, P.R. Deshmukh, V.S. Jamdade, D.S. Dhawale, U.M. Patil, C.D. Lokhande*

Poster presentation RAINMAA-2009 held at G. B. Patel Science and STSKVS Commerce college, Shahada, Dist-Nandurbar.

4 “LPG sensing properties of ZnO nanorods synthesized by chemical method: effect of film thickness.”

K.V. Gurav, P.R .Deshmukh, **S.B. Kulkarni**, S.N. Pusawale, U.M.Patil, C.D. Lokhande*

Poster presentation NCMS-2010, Amaravati.

5 “Synthesis of ZnO nanorods by chemical bath deposition: annealing effect.”

K.V. Gurav, P.R .Deshmukh, **S.B. Kulkarni**, S.N. Pusawale, U.M.Patil, C.D. Lokhande*

Poster presentation, Jodhapur.

6 “Potentiodynamic deposition of Co-Ni hydroxides onto cost effective flexible substrate: supercapacitors.”

**S.B. Kulkarni**, P.R .Deshmukh, U.M.Patil, C.D. Lokhande*

Poster presentation Jodhpur.

7 "Synthesis of PANI/ZnO Nanocomposite Thin Films by Chemical Bath Deposition at Low Temperature"

**S.B. Kulkarni**, P.R. Deshmukh, C.D. Lokhande, S.S. Joshi**.**

2nd NATCON NAMTECH-2009 to be held in the Department of Physics, University of Lucknow, from December 21 to 23, 2009.

8 "Room Temperature Synthesis of Polyaniline (PANI) by Novel Facile SILAR Method"

**S.B. Kulkarni**, C.D. Lokhande, S.S. Joshi.

Second International Conference on Polymer Processing and Characterization (ICPPC–2010) January 15, 16 and 17, 2010, Kottayam, Kerala, India

9 "Potentiostically deposition of Co(OH)2 Ni(OH)2 thin film electrodes for supercapacitors."

**S.B. Kulkarni**, U.M Patil, K.V. Gurav, S.S. Joshi, C.D. Lokhande,.

Second International Conference on Polymer Processing and Characterization (ICPPC–2010) January 15, 16 and 17, 2010, Kottayam, Kerala, India

10 Bath temperature effect: Morphology evolution of nanocrystalline ZnO thin films via chemical route"

**S. B. Kulkarni**, B.B. Rajeshaikh, S.S. Joshi, C.D. Lokhande*.

Advances in synthetic mrthodologies and new materials. (ASMAM-January 21-22, 2011)

11 "Study of Temperature Impact on Morphological Evolution and Physico-Chemical Properties of ZnO."

**S.B. Kulkarni**, B.B. Rajeshaikh, U.M. Patil, S.S. Joshi, C.D.Lokhande*

22nd Annual Green Meeting (AGM) of Materials Reasearch Society of India (MRSI) Feb.14-16, 2011 at Bhopal.

12 "Synthesis and Characterization of Polyaniline/$TiO_2$ Nanocomposite Films by Simple Chemical route"

B.B. Rajeshaikh, S.S. Joshi, **S.B. Kulkarni**, C.D. Lokhande*.

National seminar on Physics of materials and materials based device fabrication (NSPM-MDF-February 17-18, 2011)

# INDEX

# CHAPTER I

## General Introduction and Literature Survey

## CHAPTER I

## 1.1 General: Need of Supercapacitor, Nanomaterials for Supercapacitors

### 1.1.1 Necessity of supercapacitor:

In response to the changing global landscape, energy has become a primary focus of the major world powers and scientific community. Environment pollution, global warming and hasty resource depletion due to consumption of fossil fuels resulted into energy crisis. As the problem of a vast consumption unable to fulfill the current energy demand of the world and seems not to be solvable with the ‘‘conventional energy sources within a foreseeable period of time. Based on moderate economic and population growth, the global energy consumption is anticipated to triple by the year 2100 [1]. Also recent increase in worldwide gasoline prices, as well as ongoing public and governmental stress for a more environmentally friendly and fuel efficient means of transportation, automotive manufacturers are developing product lines that incorporate true alternatives to the gas-powered transports. Development of alternative, sustainable, clean and green energy technologies is needed to address these inevitable challenges. Among the various alternative energy technologies, the electrochemical energy technologies are the most viable option for automobiles. Henceforth, the technology stimulated modern society in the development and refinement of more efficient energy storage devices mainly with variety of electrochemical power sources, which deals “clean and green energy”. It is pointed out that for the foreseeable future, only electrochemical energy systems will be available for powering vehicles and portable electronic devices. An electrochemical energy system comprises several power types as batteries, fuel cells and supercapacitors [1]. Electrochemical energy systems afford many benefits as compared to fuel combustion systems. Major one is, energy provided by electrochemical system is clean, economical and eco-friendly which is crucial regarding environmental point of view. Secondly, they are

potentially more proficient and dynamic enough than fuel combustion systems with higher conversion efficiency.

An immense variety of electric appliances of daily life, on large scale optionally or exclusively operated on electric energy from wide area of fields ranging from industrial to domestic applications e.g. cell phones, pagers, solar cells, computers, satellites, standby power supply systems, hybrid electric vehicles, etc [2]. So, electrical energy is an important part in our daily life. It can universally be applied and easily be converted into light, heat or mechanical energy. As electrical energy is currently available and easily accessible source but not obtainable at all time and can hardly be stored. As a result, there is necessity of development of superior methods for storing electrical energy when it is available and can be retrieved when needed. Basically electrical energy storage can be made in two ways; (1) Batteries (Indirect storage): In batteries the energy of chemical compounds acts as storage medium needs faradic oxidation and reduction to release charges during discharge which can perform electrical work when they flow between two electrodes of different electrode potentials. A chemical process occurs that generates energy which can be drawn from the battery in the form of an electric current at a certain voltage. For battery systems this process can be reversed and the battery recharged, i.e. the intake of electric energy can restore the chemical composition that contains higher energy and can closely reestablish the original structures within the battery. While storing electrochemical energy in the battery, due to the chemical kinetics involving irreversible inter-conversion of electrode material changes its phase can limit cycle life of storage batteries which varies accordingly with battery type [3]. Also, batteries cannot handle high power levels for long time periods in addition rapid discharge cycles may shorten the battery life leading to early replacement. Furthermore, there are some environmental concerns related to the use of batteries due the hazardous materials contained on

them, and the toxic gases generated during the charge discharge cycles. The disposal of the hazardous materials contained in the batteries implies additional costs due to strengthen environmental regulations. (2) Capacitors (Direct storage): In conventional capacitors (condensers), the charge accumulation is achieved electrostatically by positive and negative charges residing on two interfaces separated by a vacuum or a molecular dielectric medium. Capacitors allow direct storage of charges via non faradaic reaction, henceforth no chemical interconversion and phase change of plate electrodes aroused. Theoretically, offers unlimited recyclability and long life, typically $\sim 10^6$ times [2-4].

For energy extraction, we can obtain 100 % of stored energy by discharging a battery totally for long time period at low discharge rates. Although, power appliances frequently require a short and high power burst within very short time. At such condition, battery can deliver only a few percent of total stored capacity. It is superior to get current from battery for one minute than for few seconds. Even though, often use of battery for such work, needs electric capacity; which make weight, volume and cost much higher than the required electrical output. Hence, battery is ineffective in such short term power burst situations, which greatly reduces its operating life [5]. On the other hand, capacitors store power in the form of static electricity than that of reversible, faradic chemical reactions in the batteries and release all of stored energy instantly within few milliseconds. But the amount is very small, compared to the demand of most applications. Storing capacity of ordinary capacitor is of the order of microfarad (μF) or millifarad (mF), while supercapacitors offer thousands time greater charge storage capability in farad (F) or kilofarad (kF) than capacitors.

The current 'electronic age' demands high quality power. One such device, the supercapacitor, has matured significantly over the last decade and emerged with the potential to facilitate major advances in energy

storage. Supercapacitors, also known as ultracapacitors or electrochemical capacitors, utilize high surface area electrode materials and thin electrolytic dielectrics to achieve capacitances several orders of magnitude larger than conventional capacitors [1-5]. In doing so, supercapacitors are able to exploit both the advantages of battery (high energy density) and conventional capacitors (high power density). Additionally, they are superior than electrochemical batteries and fuel cells, including higher power density for appliances requiring high power bursts in the seconds range such as an ignition having shorter charging times and longer cycle life.

The performance for a supercapacitor is shown in figure 1.1; a graph termed a "Ragone plot". This type of graph presents the energy densities ($Wh.kg^{-1}$) i.e. how much energy is available of various energy storage devices, measured along the vertical axis, versus their power densities ($W.kg^{-1}$) i.e. how quickly that energy can be delivered, measured along the horizontal axis on logarithmic scale. It is seen that, supercapacitors occupy a region between conventional capacitors and batteries [2]. Despite greater capacitances than conventional capacitors, supercapacitors have yet to match the energy densities of mid to high-end batteries and fuel cells. The basic difference in working mechanism among ordinary capacitors, supercapacitors and batteries can be easily explained with the help of water tank analogy to understand actual theme represented by "Ragone plot" as shown in figure 1.2.

Hybrid Electric Vehicle (HEV) technology is most promising alternative to fuel cell driven vehicles. In the case of supercapacitor-enhanced HEVs, the traditional combustion engine functions as the primary power source. It handles continuous load requirements such as cruising and basic electric needs. Supercapacitors function as the secondary power source and they are sized for short duration load leveling.

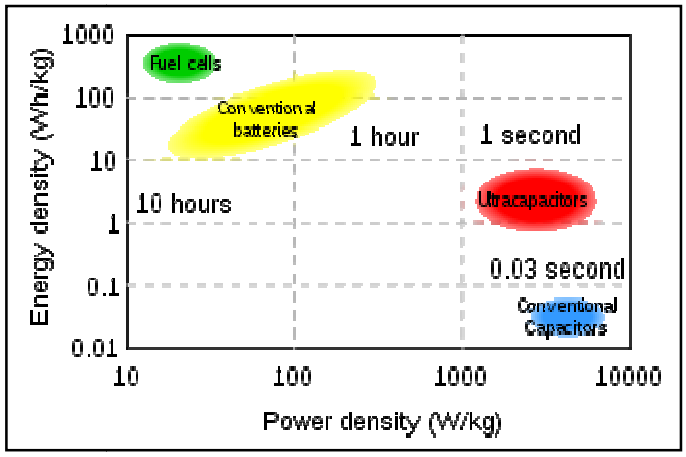


**Fig.1.1** Ragone chart showing performance comparison of various energy storage devices as logarithmic plot of energy density vs. power density [6].

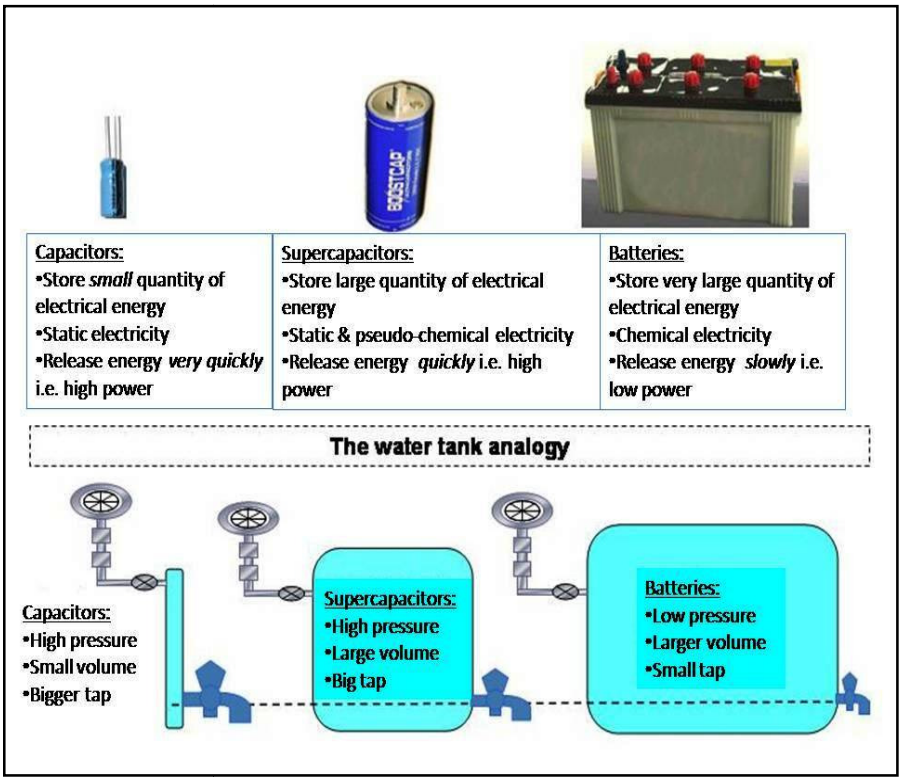


**Fig.1.2** The water tank analogy for illustration of working mechanism of ordinary capacitors, supercapacitors and batteries [7].

As these short duration events are experienced many thousands of times throughout the life of a vehicle, they are very well suited for the long life cycle of the supercapacitor, which can cycle millions of times without

any constraint on depth of discharge. Supercapacitors can also improve HEV mechanical design. Where additional batteries that are used to handle peak loads facilitate an overall increase in system size, weight and ultimately cost, the use of more powerful, smaller, and lighter supercapacitors causes an overall reduction in system size. Moreover, unlike batteries - which often fail to function in temperatures below 273 K - supercapacitors can operate successfully in wide temperature ranges, including those as low as 233 K. At the moment, numerous industries are empowering in the supercapacitors development with expected applications to boost components supporting batteries or replacing batteries, primarily in electric vehicles [7].

Major advantages of supercapacitor over the battery and conventional capacitor [8].

1) Virtually unlimited cycle life - can be cycled millions of time.
2) High power density.
3) Specific capacitance value ranges from Farads to several thousands Farads ($10^5$-$10^6$ times ordinary capacitors).
4) Quick charging – discharging, supercapacitors charge in seconds.
5) Trouble-free charging process. No special charging or voltage detection circuits needed like batteries.
6) Offer low impedance when put in paralleled with a battery and improve load handling.

Also, supercapacitors show great promise for industrial applications because of the following attributes:

- Technical maturity
- Chemical inertness
- Very limited environmental impact (no use of heavy metals)
- Expected performance vs. reasonable cost

The development of an energy storage device that has an energy density approaching that of a battery and the power density of a capacitor is an ultimate goal for power quality and energy storage of supercapacitors. They store energy using either ion adsorption (electrochemical double layer capacitors) or fast surface redox reactions (pseudo-capacitors). They can complement or replace batteries in electrical energy storage and harvesting applications, when high power delivery or uptake is needed. A notable improvement in performance has been achieved through recent advances in understanding charge storage mechanisms and the development of advanced nanostructured materials.

### 1.1.2 Demand of nanostructured electrode materials for supercapacitors:

The scaling down of functional structures has been a dominating trend in many fields of science and technology. The size reduction of structures from the micrometer to the nanometer scale leads not only to a miniaturization of functional units but also to the development of new materials and systems with unconventional physical and chemical properties. Design and development of new materials that can lower the cost, increase the efficiency and improve the durability can have a significant impact in making energy technologies commercially viable. In this regard, nanostructured materials and nanotechnology offer great promise because of the unusual properties endowed by confining their dimensions and the combination of bulk and surface properties to the overall behavior. The fundamental physical and chemical properties of materials are surprisingly altered as their constituent grains are decreased to a nanometer scale. Nanostructured materials play an important role in advancing the electrochemical energy storage and conversion technologies offering great promise to address the rapidly growing environmental concerns and the increasing global demand for energy by offering high

performance, affordable materials for electrochemical energy storage and conversion. The interest in these materials has been stimulated by the fact that, owing to the small size of the building blocks (particle, grain, or phase) leads to a variety of exciting phenomena due to enhanced surface-to-volume ratio and reduced transport length for the mobile charges [9, 10]. These materials are appealing in improving performance parameters such as high rate (power) capability and long cycle life, particularly to increase the energy density and rate capability [11, 12].

The nanostructures involved often combine fascinating shapes with remarkable properties. With the introduction of new techniques and novel concepts for preparation of layered double hydroxide (LDH) structures, together with the requirements of practical applications, various studies focus on the properties and applications of nanostructured LDHs. There is currently an increasing interest in LDHs, due to their properties as catalysts and catalyst supports [13], antacids [14], trapping agents for anionic contaminants [15], flame retardants [16], polymer stabilizers [17], molecular sieves, ion exchangers and adsorbents [18]. New areas have been investigated for applications in the field of medicine, thin films, conducting materials, electrical and optical functional materials and nanoadditives [19] along with electrodes [20] and corrosion protection [21]. LDHs have also been recently related to the origin of life [22].

LDHs are promising materials for a large number of practical applications in catalysis, adsorption, pharmaceutics, photochemistry, electrochemistry and other areas [23]. This is due to their high versatility, easily tailored properties and low cost, which make it possible to produce materials designed to fulfil specific requirements. LDH materials have relatively weak interlayer bonding and as a consequence exhibit excellent expanding properties. Therefore, over the past few years, increasing interest has been devoted to the use of these layered inorganic solids as host materials in order to create inorganic-organic host-guest hybrid

structures with desirable physical and chemical properties, in which the brucite-like layers may impose a restricted geometry on the interlayer guests leading to enhanced control of stereochemistry, rates of reaction and product distributions. The possibility of the formation of three-dimensional pillared layered structures by appropriate intercalation processes opens up new perspectives for functional materials with novel properties [24, 25].

LDHs are promising contender for electrode materials and are attractive as replacements since they have much better stability, tolerance to high temperatures and oxidizing conditions, chemical inertness along with very high theoretical specific capacitance. Also, due to the capability of clays to exchange intercalated ions, clay modified electrodes gained prime importance.

Nanotechnology offers scope in modification and tuning of the electrode structure at the nano dimensions. The control over optimized pore structure is responsible for high energy storage and uniformity in nanosized pores is the major demand in this application [26].

#### 1.1.2.1 Material in the thin film form:

Any solid system (material) having periodicity extended mostly along two dimensional orders while third dimension is restricted is called as a "thin film". The third dimension, being the thickness is very small compared to other two dimensions. Emerging properties of thin film are considerably different from that of bulk material due to surface and interface effects and may dominate the overall performance of the films [27]. Therefore, thin films are potentially used in several applications in various fields such as, anti-reflecting coating, wave guide coating, photo-thermal solar coatings, hard coatings, interference filters, polarizer, narrow band filters, solar cells, photo-detectors, magnetic films, superconductivity, high temperature wear resistance films, battery

electrodes, electrochemical capacitor electrodes, etc [28]. The current advancement made in surface physics and surface characterization is significant and having great importance in the study of materials in a configuration with a large surface to volume ratio (i.e. thin film). The potentiality of material in the thin film form explores enhancement in the performance than the bulk form. According to suitability of material in various applications, these thin film deposition techniques are supportive to achieve fully utilization of material for upgrading the performance [29].

## 1.2 Literature survey on LDHs materials:

### 1.2.1 Introduction to Layered double hydroxide (LDH) materials:

The terms layered double hydroxides (LDHs) or hydrotalcite-like compounds (HTLc) are used to designate synthetic or natural lamellar hydroxides with two or more kinds of metallic cations in the main layers and hydrated interlayer domains containing anionic species. This large family of compounds is also commonly referred to as hydrotalcites or anionic clays (i.e. anion exchanging), the latter term indicating a complementarity with the more usual cationic clays whose interlamellar domains contain cationic species. The LDHs are so called hydrotalcite-like compounds due to their structural similarities to hydrotalcite, a mineral with the formula $Mg_6Al_2(OH)_{16}CO_3{\cdot}4H_2O$. The hydrotalcite structure results from the stacking of brucite-like layers [$Mg(OH)_2$] containing a positive residual charge arising from the partial isomorphous substitution of $Mg^{2+}$ cations by $Al^{3+}$ cations. This positive excess charge is balanced by the carbonate anions, which reside in the interlamellar spaces [30].

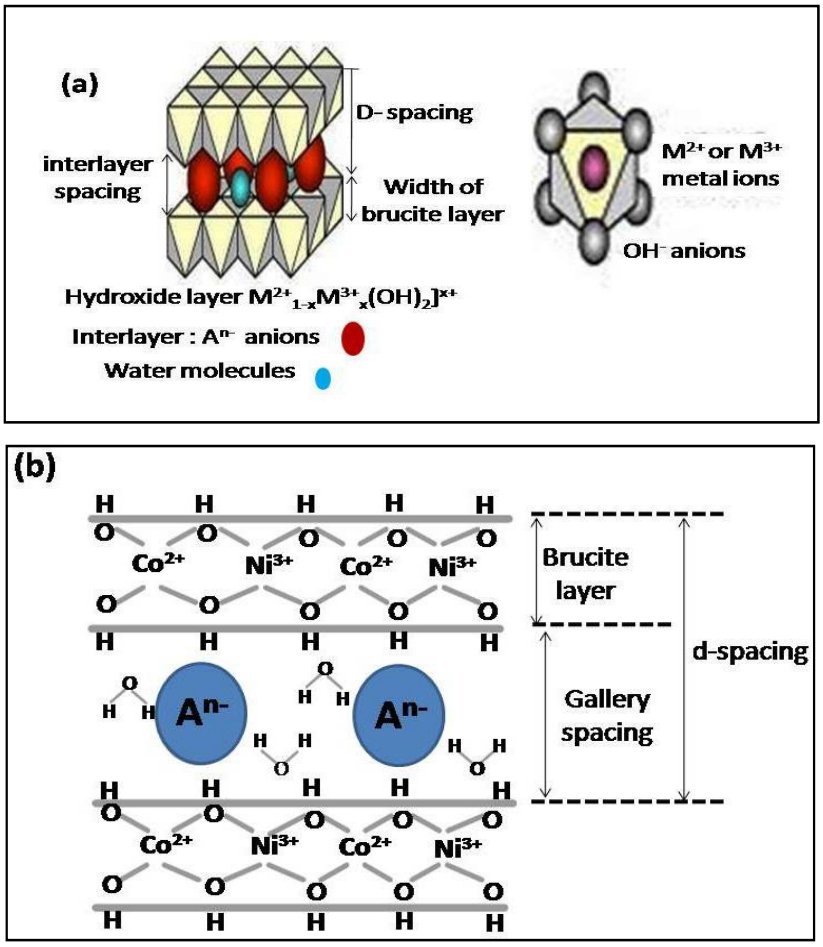


**Fig 1.6** (a) Schematic representation of layered crystal structure of hydrotalcite-like compounds (b) Idealized structure of a Co-Ni layered double hydroxide with interlayer anions

The LDHs may be described by the general formula

$$[M^{2+}_{1-x}M^{3+}_{x}(OH)_2]^{x+}\ (A^{n-}_{x/n})\cdot mH_2O$$

Where, $M^{2+}$ (such as $Co^{2+}$, $Ni^{2+}$, $Mg^{2+}$, $Zn^{2+}$, $Mn^{2+}$, $Ca^{2+}$ or $Fe^{2+}$ ) and $M^{3+}$ (such as $Co^{3+}$, $Ni^{3+}$, $Al^{3+}$, $Cr^{3+}$, $Mn^{3+}$, $Fe^{3+}$ or $Ga^{3+}$) can be any di and tri valent metal ions (whose ionic radius is not too different from that of $Mg^{2+}$), and *x* is the metal ratio $M^{3+}/(M^{2+}+M^{3+})$. LDHs consist of layers of $M^{2+}$ and $M^{3+}$ cations which are octahedrally co-ordinated by six oxygen anions, as hydroxides and two-dimensional infinite layers are formed by edge-sharing of the octahedral [31]. These layers exist with a similar layered

structure to that exhibited by natural $Mg(OH)_2$, i.e. brucite. Partial isomorphous substitution of trivalent cations for divalent ones results in a positive charge on the layers. Organic or inorganic anions are intercalated between the layers in order to maintain charge balance, and water of crystallization is also generally found in the interlayer galleries [32]. The species $A^{n-}$ in the interlamellar region can be any charge compensating anion (organic or inorganic such as $CO_3^{2-}$, $NO_3^{2-}$, $SO_4^{2-}$ or $Cl^-$) and *m* is the amount of water present in the same region [33]. The electrostatic interactions and hydrogen bonds between the layers and the contents of the gallery hold the layers together, forming the three-dimensional structure. A special case occurs when $A^{n-}$ is the hydroxide ion, $OH^-$. This class of compounds are called Meixnerite-like compounds (MLCs) because of their similarities to $Mg^{2+}{}_6Al^{3+}{}_2(OH)_{16}(OH)_2{\cdot}4H_2O$, a compound named after Meixner [34]. The schematic representation of layered crystal structure of hydrotalcite-like compounds and idealized Co-Ni layered structural illustration are shown in figure 1.6 (a) and (b), respectively.

### 1.2.2 Literature survey on synthesis of LDH materials and their applications:

Considering generally as promising materials in view of their high chemical versatility associated with a tunable anionic exchange capacity along with highly active surface atoms, LDHs is of great interest and importance to generate alternative predefined structures and morphologies. Important advances in LDH morphology have been made in the past years, ranging from LDH powders, spheres, nanosized LDH belt, fibrous structure to LDH films on substrates [35-39]. LDH compounds have been synthesized by direct methods, which include co-precipitation [33, 40], sol-gel synthesis [41], chimie douce [42], salt-oxide reaction [43], hydrothermal growth [44], electrochemical synthesis [45] and spray drying [46].

Indirect methods include all synthesis that uses an LDH as a precursor. Examples of these are all anion exchange based methods such as direct anion exchange [47], anion exchange by acid attack with elimination of the guest species in the interlayer region and anion exchange by surfactant salt formation [48]. The non-anion exchange methods include the delamination-restacking method and LDH reconstruction method [49, 50]. Gursky et al. [51] obtained nanosized colloidal Mg-Al LDH particles through coprecipitation from metal salts dissolved in methanol in the presence of NaOH. Xu et al. [35] also prepared colloidal Mg-Al LDH by a fast co-precipitation followed by controlled hydrothermal treatment having LDH platelets dimensional sizes ranging from 50 to 300 nm. Zhang et al. synthesized Mg-Al LDHs with a high aspect ratio via calcination and rehydrolysis under hydrothermal conditions [52]. Zhao et al. prepared Mg-Al LDH nanowires and nanorods via hydrothermal treatment at a high temperature and Zn-Co-Fe LDH nanowires with controllable morphology in a water-in-oil microemulsion [53, 54]. The major advantage of fabrication of well-oriented or self-supporting LDH films is to avoid spontaneous aggregation of LDH powders. LDH films usually consist of face-on oriented building blocks of platelet-like LDHs. The face-on orientation of the building blocks of LDH platelets are achieved through various methods, such as solvent evaporation [55], electrochemical deposition [56], spin-coating technique [57], Langmuir-Blodgett (LB) technique [58], Layer-by-layer (LbL) technique [59] and in-situ growth [59].

Mainly, layered nickel hydroxide often used as an electrode for alkaline secondary cells. To improve its properties, modification has been carried out by incorporation of other metal elements to form Ni-M LDHs, including Co [60], Zn [61], Al [62], Cr or Mn [63] and Fe [64]. For example, Chen et al. reported the electrochemical performance of Al-substituted layered $\alpha$-$Ni(OH)_2$ with appropriate additives in Ni-metal hydride

batteries [62]. They found that, the addition of $Mg^{2+}$ increases the unit cell parameters and the charge and discharge potentials and decreases the electrochemical polarization. A higher charge efficiency and cycle life is obtained by the addition of $Co^{2+}$. The authors suggested that, the addition of both $Mg^{2+}$ and $Co^{2+}$ could improve the stability in alkaline solution at high temperature.

Chen et al. studied the effects of zinc on the structure and electrochemical performance of Ni-Al LDHs prepared by a coprecipitation method. The addition of zinc in Ni-Al LDHs improved the electrochemical performance of the samples such as discharge potential, cycle stability and reversibility [61]. Scavetta et al. have been electrosynthesized thin films with controlled thickness of Co-Al LDH with different Co and Al percentages by the cathodic reduction of a 0.03M Co and Al nitrate solution. The electrochemical behavior of the films deposited on Pt or ITO electrodes has been deeply studied in 0.1M NaOH solution [65]. LDHs of cobalt with aluminium and chromium, isostructural with α-cobalt(II) hydroxide, are electrosynthesized by Dixit et al. [66]. The effect of the interlayer anions on the electrochemical performance and a comparison of two well-crystallised LDHs, $[Ni_4Al(OH)_{10}]OH$ and $[Ni_4Al(OH)_{10}]NO_3$, were presented by Lei et al. [67]. Ni-Al LDH nanosheet film grown directly on Ti substrate by Li et al.[68]. Béléké et al. studied electrochemical properties of nickel–aluminum layered double hydroxide/carbon composites (Ni–Al LDH/C) fabricated by liquid phase deposition [69]. Jayashree et al. studied nickel-based LDHs with Cr and Mn as candidate electrode materials for alkaline secondary cells [63]. Su et al. proposed CNTs/Co-Al LDHs as potential supercapacitor electrode material and their electrochemical performance was studied by cyclic voltammetry, galvanostatic charge/discharge measurements and impedance spectroscopy [70]. Electrochemical study of nanostructured multiphase nickel hydroxide was carried out by Wang et al. They reported that, electrochemical behavior of

the high density spherical multiphase α-$Ni(OH)_2$ have much better redox reversibility, a much lower oxidation potential of Ni(II) than the corresponding oxidation state in the case of β-$Ni(OH)_2$ and a much higher reduction potential [71]. In situ raman studies on cathodically deposited nickel hydroxide films and electroless Ni-P electrodes in 1M KOH solution was carried out by Lo et al. [72]. $Co_{0.56}Ni_{0.44}$ oxide nanoflakes with a maximum specific capacitance of 1227 $Fg^{-1}$ was synthesized by Lang et al. and observed specific capacitor 97 $Fg^{-1}$ and specific energy of 34.5 W h/kg for asymmetric $Co_{0.56}Ni_{0.44}$ oxide nanoflake materials and activated carbon electrodes in 2M KOH [73]. Vidotti et al. reported sonochemically synthesized $Ni(OH)_2$ and $Co(OH)_2$ nanoparticles and their application in electrochromic electrodes [74]. The maximum specific capacitance of 684 $F.g^{-1}$ was observed in 6M KOH for Co–Al LDHs prepared via chemical method by Wang et al. [75]. However, Su et al. reported capacitance value of 145 $F.g^{-1}$ for chemically synthesized Co–Al LDHs in 1M NaOH [76]. Also, Wang et al. hydrothermally prepared Co-Al LDHs and reported 163 $F.g^{-1}$ of specific capacitance in 0.5M NaOH [77]. Liu et al. synthesized ternary Ni-Co-Al-LDHs by chemical coprecipitation method and obtained capacitance of 960 $F.g^{-1}$ in 6M KOH [78]. Wang et al. chemically synthesized Ni-Al LDH and obtained specific capacitance value 701 $F.g^{-1}$ in 6M KOH [79]. Synthesis of $Co_xNi_{1-x}$ LDHs by Gupta et al. via potentiostatic deposition route showed a maximum specific capacitance of 2104 $F.g^{-1}$ in 1M KOH [80]. Recently, Hu et al. reported nanostructured mesoporous $Co_xNi_{1-x}$ LDHs synthesized by a chemical co-precipitation route has a specific capacitance of 1809 $F.g^{-1}$ at a current density of 1 $Ag^{-1}$ in 6M KOH [81].

The promising characteristics of LDH materials are the better substitution and/or options to fulfill the current demands regarding energy consumption. Table 1.1 shows the specific capacitance values exhibited by Co, Ni hydroxides/LDHs with preparation methods and the

electrolyte used. Over all, LDHs have provided their superior capability as an electrode in supercapacitor application.

**Table 1.1: Co, Ni hydroxide/LDH materials for supercapacitor with specific capacitance, specific energy and specific power.**

| Sr. No. | Material | Method of preparation | Electrolyte | Specific capacitance ($F.g^{-1}$) | Reference |
|---|---|---|---|---|---|
| 1 | $Ni(OH)_2$ | Electrodeposition | 3M KOH | 578 | 82 |
| 2 | Co–Al LDH | Chemical method | 6M KOH | 684 | 75 |
| 3 | $Ni(OH)_2$/Activated Carbon | Chemical method | 6M KOH | 530 | 83 |
| | $Co(OH)_2$/Y Zeolite | Chemical method | 6M KOH | 1492 | 84 |
| 5 | $Co(OH)_2$–$Ni(OH)_2$/Y Zeolite | Chemical method | 6M KOH | 479 | 85 |
| 6 | Ni–Co–Al LDHs | Chemical method | 6M KOH | 960 | 78 |
| 7 | Zeolites | Chemical method | 6M KOH | 470 | 85 |
| 8 | Co–Al LDH | Chemical method | 1M NaOH | 145 | 76 |
| 9 | Co-Al–$CO_3$ LDH | Chemical method | 0.5M NaOH | 163 | 77 |
| 10 | $Co_xNi_{1-x}$ LDHs | Electrodeposition | 1M KOH | 2104 | 80 |
| 11 | Co–Al LDH | Chemical method | 1M LiOH | 187 | 86 |
| 12 | Ni-Al LDH | Chemical method | 6M KOH | 701 | 79 |
| 13 | α-$Co(OH)_2$ chloride anion intercalated | Chemical method | 6M KOH | 697 | 87 |
| 14 | α-$Co(OH)_2$ nitrate anion intercalated | Chemical method | 6M KOH | 638 | 87 |

| | | | | | |
|---|---|---|---|---|---|
| 15 | α-$Co(OH)_2$ acetate anion intercalated | Chemical method | 6M KOH | 526 | 87 |
| 16 | α-$Co(OH)_2$ sulfate anion intercalated | Chemical method | 6M KOH | 420 | 87 |
| 17 | $Ni(OH)_2$/Ultra Stable Y Zeolite | Chemical method | 2M KOH | 583 | 88 |
| 18 | $Ni(OH)_2$ | Chemical method | 2M KOH | 2055 | 89 |
| 19 | $Ni(OH)_2$/ Activated Carbon | Chemical method | 6M KOH | 314.5 | 90 |
| 20 | Pure Activated Carbon | - | 6M KOH | 255.1 | 90 |
| 21 | Graphene | - | 6M KOH | 137.6 | 91 |
| 22 | $Co(OH)_2$ | Chemical method | 6M KOH | 726.1 | 91 |
| 23 | Graphene/$Co(OH)_2$ | Chemical method | 6M KOH | 972.5 | 91 |
| 24 | $Co(OH)_2$/ Activated Carbon | Chemical method | 2M KOH | 72.4 | 92 |
| 25 | Nickel oxide/hydroxide | Electrodeposition | 1M KOH | 202 | 93 |
| 26 | $Co(OH)_2$/Carbin Nano Tubes | Electrodeposition | 1M KOH | 322 | 94 |
| 27 | Co–Ni $(OH)_2$ | Chemical method | 2M KOH | 324 | 95 |
| 28 | $Co_xNi_{1-x}$ LDH | Chemical method | 6M KOH | 1809 | 81 |
| 29 | $Co(OH)_2$ | Electrodeposition | 6M KOH | 280 | 96 |
| 30 | β-$Ni(OH)_2$ | Chemical method | 2M KOH | 398 | 97 |
| 31 | β-$Ni(OH)_2$ | Chemical method | 2M KOH | 398 | 98 |
| 32 | $Co(OH)_2/TiO_2$ | Chemical method | 6M KOH | 229 | 99 |
| 33 | α-$Co(OH)_2$ | Electrodeposition | 1M KOH | 860 | 100 |

## 1.3 Orientation and purpose of dissertation:

The electrode is the key part of the electrochemical devices, so the electrode materials are the most important factors to determine the properties of supercapacitors. Primly, the performance of this device usually resulted from the high specific surface area as well as the highly reversible redox reactions of the electrode materials. Literature survey exemplify that, supercapacitors make use of porous activated carbon (AC), hydrous transition metal oxides, metal hydroxides, electronically conducting polymers, mixed metal oxides/hydroxides or their composites are the main components as an electrode materials. Among these electrode materials, AC, as the representative electrode material of the EDLCs, has rapid current–voltage (I–V) response and rectangle cyclic voltammetry shape, whereas its specific capacitance is relatively low. Electroactive materials with several oxidation states or structures, such as transition metal oxides and conducting polymers, can provide a large reversible capacity, good cycling performance and high recharging rates for pseudocapacitors. Conducting-polymer capacitors have been reported to display high power densities, but their specific capacitances are much lower than those of metal oxide capacitors [73]. However, metal hydroxide (e.g. $Co(OH)_2$, $Ni(OH)_2$, etc ) materials are attractive on account of their layered structure with large interlayer spacing and their well defined electrochemical redox activity. Being an important electrochemical active material, a great deal of interest has been centered on the utilizations of LDH material in alkaline batteries, fuel cells and supercapacitors. Previous reports have shown that the film of LDH material has a higher specific capacitance than that of $RuO_2$ [80].

The key factors determining the performance of supercapaciotrs are the specific surface area (SSA) of electrode materials and the properties of electrolytes. Also, understanding and modifying the surface properties are crucial in achieving the high power and energy density values for

supercapacitors. Hence, it would be of great interest to develop metal hydroxide (LDHs) electrode materials with the large capacity and high rate capability for supercapacitors. This opens up further possibilities for achieving nanomaterial composites with high specific capacitances.

Currently, nanostructured materials play an important role in advancing the electrochemical energy storage and conversion technologies, offering great promise to address the rapidly growing environmental concerns and the increasing global demand for energy. Wherein, the physical properties are changing accordingly size. There are two approaches to produce nanocrystalline (or amorphous) dimensionally stable anodes (DSA) for supercapacitor application, "bottom-up" (chemical methods) approach and "Top-down" (physical methods). The electrochemical behavior of material results directly from their morphology, which on the other hand, depends on the preparation procedure and conditions. In order to improve the electrochemical properties of the material, the size and distribution of the particles have to be adjusted.

This work is concerned with the development of supercapacitor electrodes of $Co_{1-x}Ni_x$ layered double hydroxide (LDH) films prepared by electrodeposition method, which can offer the fulfillment of the requirements of the supercapacitor. The metal hydroxides prepared by the precipitation process have a disadvantage due to the agglomeration of particles during preparation. The resultant particle size is large and need a binder for electrode preparation. However, such disadvantages can be avoided by using electrodeposition method to obtained very high specific capacitances. Among various other deposition methods, preparation of thin films using electrodeposition technique has several attractive features such as (i) it is an isothermal process in which, the thickness and morphology of the films can be easily controlled by electrochemical parameters such as electrode potential and current (charge), (ii) relatively

uniform films can be obtained on substrates of complex shape, (iii) the deposition rate is higher than other physical and chemical methods, (iv) the equipments needed are not expensive and does not require sophisticated instrumentation and vacuum, (v) electrodeposition usually has low operating temperature. Apart from the obvious advantages in terms of energy saving the low deposition temperature avoids high temperature effects such as interdiffusion, contamination and dopant redistribution. Even with above advantageous points, electrodeposition has interesting feature that, direct cathodic electrodeposition from aqueous and non-aqueous baths is possible and it can be employed as one of the steps in the preparation of semiconductors or oxides.

There are well known three electrodeposition modes by which we can apply the electric field, proffering by changing electric field (potentiodynamic), constant voltage (potentiostatic) and constant current (galvanostatic). The application of electric field with the different modes can be useful to deposit various nanostructures and appreciably influence the physico-chemical properties and hence can amend the supercapacitive performance of the deposited materials. Various modes of electrodeposition, it is possible to deposit nanocrystalline/amorphous, $Co_{1-x}Ni_x$ LDH thin films of different compositions by varing molar ratios of cobalt and nickel precursors. For understanding of physico-chemical properties of any material, phase analysis, compositional characterization, structural elucidation, micro-structural analysis and surface characterization, etc are important. The X-ray diffraction (XRD) technique will be used for the structural and phase identification. Surface morphology of the films will be studied using scanning electron microscopy (SEM). The compositional study will be carried out by energy-dispersive spectroscopy (EDS) technique. The chemical bonding in the present material will be studied by Fourier Transform Infrared (FT-IR)

analysis. Wettability properties of the film surface will be studied by measuring the water contact angle.

The supercapacitor properties of the $Co_{1-x}Ni_x$ LDH films will be studied by cyclic voltametry (CV) using Potentiostat, forming a electrochemical cell comprising platinum as a counter electrode, saturated calomel electrode (SCE) as a reference electrode in a suitable electrolyte. The effect of electrolyte, thickness of electrode, scan rate and number of cycles on the performance of supercapacitor electrode will be studied. The electrochemical impedance spectroscopic (EIS) study will be carried out to measure ESR of the formed electrode.

So keeping in mind the valuability of material, present study is performed to reduce the cost and to increase the specific capacitance. Therefore, the purpose of research work is to develop the $Co_{1-x}Ni_x$ LDH electrodes by electrodeposition method and check their supercapacitive behaviour for commercial application.

**References:**


1 A.K. Shukla, S. Sampath, K. Vijaymohanan, Current Sci., 79 (2000) 1656.

2 A. Burke, J. Power Sources, 91 (2000) 37.

3 A. Chu, P. Braatz, J. Power Sources, 112 (2002) 236.

4 B.E. Conway, J. Electrochem. Soc., 138 (1991) 1539.

5 B.E. Conway, V. Briss, J. Wojtowicz, J. Power Sources, 66 (1997) 1.

6 http://www.Wikipedia.com/supercapacitor/Regon plot.

7 http://www.cap-xx.com/resources/docs.

8 M. Anderman, J. Power Sources, 127 (2004) 2.

9 R.W. Seigel, Mater Sci. Eng. B 19, (1993) 37.

10 H. Gleiter, Nanostruct. Mater., 6, (1995) 3.

11 P.G. Bruce, B. Scrosati, J.M. Tarascon, Angew. Chem. Int. Edit., 47 (2008) 2930.

12 A.T. Appapillai, A.N. Mansour, J. Cho, Y.S. Horn, Chem. Mater., 19 (2007) 5748.

13 V. Rives, M.A. Ulibarri, Coord. Chem. Rev., 181 (1999) 61.

14 N. Bejoy, J. Reson. Sci. Ed., 6 (2001) 57.

15 M. Lehmann, A.I. Zouboulis, K.A. Matis, Chemosphere, 39 (1999) 881.

16 G. Camino, A. Maffezzoli, M. Braglia, M.D. Lazzaro, M. Zammarano, Polym. Degrad. Stab., 74 (2001) 457.

17 L. van der Ven, M.L.M. van Gemert, L.F. Batenburg, J.J. Keern, L.H. Gielgens, T.P.M. Koster, H.R. Fischer, Appl. Clay Sci., 17 (2000) 25.

18 L.M. Parker, N.B. Milestone, R.H. Newman, Ind. Eng. Chem. Res., 34 (1995) 1196.

19 E. Gardner, K.M. Huntoon, T.J. Pinnavaia, Adv. Mater., 13 (2001) 1263.

20 M. Morigi, E. Scavetta, M. Berrettoni, M. Giorgetti, D. Tonelli, Anal. Chim. Acta, 439 (2001) 265.

21 R.G. Buchheit, S.B. Mamidipally, P. Schmutz, H. Guan, Corrosion Houston, TX, U.S. 58 (2002) 3.

22 S. Pitsch, R. Krishnamurthy, G. Arrhnius, Helv. Chim. Acta, 83 (2000) 2398.

23 S. Carlino, Chem. Brit., 33 (1997) 59.

24 J.L. Atwood, J.E.D. Davies, D.D. MacNicol, F. Vögtle (eds) Comprehensive Supramolecular Chemistry, (1996), vol 7. Pergamon, Oxford p 251.

25 A.M. Johnson, J. Newman, J. Electrochem. Soc., 118 (1971) 510.

26 W.G. Pell, B.E. Conway, J. Electroanal. Chem., 500 (2001) 121.

27 K.L. Chopra, I.J. Kaur, "Thin Films Device Applications" Plenum Press N. Y. (1983).

28 J. George, "Preparation of Thin Films" Marcel Dekker, Inc. N. Y. (1992).

29 C.D. Lokhande, Mater. Chem. Phys., 27 (1991) 1.

30 R. Allman, N.J. Mineral., Monatsh., 12 (1969) 544.

31 R. Allman, Chimia., 24 (1970) 99.

32 R. Allmann, Acta Crystallogr., B24 (1968) 9725.

33 F. Cavani, F. Trifiro, A. Vaccari, Catal. Today, 11 (1991) 173.

34 S. Koritnig, P. Süsse, Tschermaks, Min. Petr. Mitt., 22 (1975) 79.

35 Z.P. Xu, G.S. Stevenson, C.Q. Lu, G.Q. Lu, P.F. Bartlett, P.P. Gray, J. Am. Chem. Soc., 128 (2006) 36.

36 Y. Du, G. Hu, D. O'Hare, J. Mater. Chem., 19 (2009) 1160.

37 G. Hu, D. O'Hare, J. Am. Chem. Soc., 127 (2005) 1780.

38 M.M. Ortiz, E. Lima, V. Lara, J.M. Vivar, Langmuir, 24 (2008) 8904.

39 X. Guo, F. Zhang, S. Xu, D.G. Evans, X. Duan, Chem. Commun., 44 (2009) 6836.

40 W. Feitknecht, Helv. Chim. Acta., 25 (1942) 131.

41 T. Lopez, P. Bosch, E. Ramos, R. Gomez, O. Novaro, D. Acosta, F. Figueras, Langmuir, 12 (1996) 189.

42 C. Delmas, Y. Borthomieu, J. Solid State Chem., 104 (1993) 345.

43 A. Roy, C. Forano, K. Malki, J.P. Besse, In Synthesis of Micrporous Materials; Van Nostrand Reinhold: New York, 1992, vol. II, p. 108.

44 G. Mascolo, Appl. Clay Sci., 10 (1995) 21.

45 L. Indira, M. Dixit, P.V. Kamath, J. Power Sources, 52 (1994) 93.

46 Y. Wang, F. Zhang, S. Xu, X. Wang, D.G. Evans, X. Duan, Ind. Eng. Chem. Res., 47 (2008) 5746.

47 S. Miyata, Clays Clay Miner., 31 (1983) 305.

48 E.L. Crepaldi, P.C. Pavan, J.B. Valim, J. Mater. Chem., 10 (2000) 1337.

49 F. Leroux, M.A. Pagano, M. Intissar, S. Chauvière, C. Forano, J.P. Besse, J. Mater. Chem., 11 (2001) 105.

50 F. Prinetto, D. Tichit, R. Teissier, B. Coq, Catal. Today, 55 (2000) 103.

51 J.A. Gursky, S.D. Blough, C. Luna, C. Gomez, A.N. Luevano, E.A. Gardner, J. Am. Chem. Soc., 128 (2006) 8376.

52 Q. Tao, Y. Zhang, X. Zhang, P. Yuan, H.P. He, J. Solid State Chem., 179 (2006) 708.

53 Y. Zhao, Q.Z. Jiao, X.J. Ding, L.Q. Zhang, Y.Y. Liu, Chem. Res. Chin., 23 (2007) 622.

54 H. Wu, Q. Jiao, Y. Zhao, S. Huang, X. Li, H. Liu, M. Zhou, Mater. Character, 61 (2010) 227.

55 J.H. Lee, S.W. Rhee, H.J. Nam, D.Y. Jung, Adv. Mater., 21 (2009) 546.

56 A. Khenifi, Z. Derriche, C. Forano, V. Prevot, C. Mousty, E. Scavetta, B. Ballarin, L. Guadagnini, D. Tonelli, Analy. Chim. Acta, 654 (2009) 97.

57 F. Zhang, M. Sun, S.L. Xu, L. Zhao, B. Zhang, Chem. Eng. J. 141 (2008) 362.

58 J.X. He, S. Yamashita, W. Jones, A. Yamagishi, Langmuir, 18 (2002) 1580.

59 D.P. Yan, J. Lu, M. Wei, J.B. Han, J. Ma, F. Li, D.G. Evans, X. Duan, Angew. Chem. Int. Ed., 48 (2009) 3073.

60 R.S. Jayashree, P.V. Kamath, J. Electrochem. Soc., 149 (2002) 761.

61 H. Chen, J.M. Wang, T. Pan, H.M. Xiao, J.Q. Zhang, C.N. Cao, Int. J. Hydrogen Energ., 27 (2002) 489.

62 H. Chen, J.M. Wang, T. Pan, Y.L. Zhao, J.Q. Zhang, C.N. Cao, J. Electrochem. Soc., 150 (2003) 1399.

63 R.S. Jayashree, P.V. Kamath, J. Power Sources, 107 (2002) 120.

64 H. Sakaebe, H. Uchino, M. Azuma, M. Shikano, S. Higuchi, Solid State Ionics, 15 (1998) 35.

65 E. Scavetta, B. Ballarin, M. Gazzano, D. Tonelli, Electrochim. Acta, 54 (2009) 1027.

66 M. Dixit, P.V. Kamath, J. Power Sources, 56 (1995) 97.

67 L. Lei, M. Hu, X. Gao, Y. Sun, Electrochim. Acta, 54 (2008) 671.

68 X. Li, J. Liu, X. Ji, J. Jiang, R. Ding, Y. Hu, A. Hu, X. Huang, Sens. Actu. B 147 (2010) 241.

69 A.B. Béléké, M. Mizuhata, J. Power Sources, 195 (2010) 7669.

70 L.H. Su, X.G. Zhang, Y. Liu, J. Solid. State. Electrochem. 12 (2008) 1129

71 X. Wang, P.J. Sebastian, A. Millan, P.V. Parkhutik, S.A. Gamboa, J. New. Mat. Electrochem. Syst., 8 (2005) 101.

72 Y.L. Lo, B.J. Hwang, Langmuir, 14 (1998) 944.

73 J. Lang, L. Kong, M. Liu, Y. Luo, L. Kang, J. Electrochem. Soc., 157 (2010) A1341.

74 M. Vidotti, C. Greco, E.A. Ponzio, S.I. Torresi, Electrochem. Commun., 8 (2006) 554.

75 Y. Wang, W. Yang, S. Zhang, D.G. Evans, X. Duan, J. Electrochem. Soc., 152 (2005) A2130.

76 L. Su, X. Zhang, J. Power Sources, 172 (2007) 999.

77 J. Wang, J. You, Z. Li, P. Yang, X. Jing, M. Zhang, J. Electroanal. Chem., 624 (2008) 241.

78 X.M. Liu, Y.H. Zhang, X.G. Zhang, S.H. Fu, Electrochim. Acta, 49 (2004) 3137.

79 J. Wang, Y. Song, Z. Li, Q. Liu, J. Zhou, X. Jing, M. Zhang, Z. Jiang, Energy Fuels, 24 (2010) 6463.

80 V. Gupta, S. Gupta, N. Miura, J. Power Sources, 175 (2008) 680.

81 Z. Hu, Y. Xie, Y. Wang, H. Wu, Y. Yang, Z. Zhang, Electrochim. Acta, 54 (2009) 2737.

82 D.D. Zhao, S.S. Bao, W.J. Zhou, H.L. Li, Electrochem. Commun., 9 (2007) 869.

83 J.H. Park, O.O. Park, K.H. Shin, C.S. Jin, J.H. Kim, Electrochem. Solid State Lett. 5 (2002) H7.

84 L. Cao, F. Xu, Y.Y. Liang, H.L. Li, Adv. Mater., 16 (2004) 1853.

85 Y.Y. Liang, S.J. Bao, H.L. Li, J. Solid State Electrochem., 11 (2007) 571.

86 L. Su, X. Zhang, C. Mi, Y. Liu, J. Power Sources, 179 (2008) 388.

87 Z. Hu, Y. Xie, Y. Wang, L. Xie, G. Fu, X. Jin, Z. Zhang, Y. Yang, H. Wu, J. Phys. Chem. C, 113 (2009) 12502.

88 L. Cao, L. Kong, Y. Liang, H. Li, Chem. Commun., (2004) 1646.

89 J.W. Lang, L. Kong, W. Wu, M. Liu, Y. Luo, L. Kang, J. Solid State Electrochem.,14 (2009) 1333.

90 Q. Huang, X. Wang, J. Li, C. Dai, S. Gamboa, P.J. Sebastian, J. Power Sources, 164 (2007) 425.

91 S. Chen, J. Zhu, X. Wang, J. Phys. Chem. C, 114 (2010) 11829.

92 L. Kong, M. Liu, J. Lang, Y. Luo, L. Kang, J. Electrochem. Soc., 156 (2009) A1000.

93 M. Wu, Y. Huang, C. Yang, J. Electrochem. Soc., 155 (2008) A798.

94 X. Wang, D. Ruan, Z. You, Chin. J. Chem. Phys., 19 (2006) 499.

95 S.G. Kandalkar, H. Lee, S. Seo, K. Lee, C. Kim, J. Mater. Sci, 10 (2010) 5174.

96 Z. Wang, X. You, Z. Ruan, D. Bo, J. Chin. Chem., 24 (2006) 1126

97 U.M. Patil, K.V. Gurav, V.J. Fulari, C.D. Lokhande, O.S. Joo, J. Power Sources, 188 (2009) 338.

98 S.B. Kulkarni, V.S. Jamadade, D.S. Dhawale, C.D. Lokhande, Appl. Surf.

Sci. 255(2009) 8390

99 F. Tao, Y. Shen, Y. Liang, H. Li, J. Solid State Electrochem., 11 (2007) 853.

100 V. Gupta, T. Kusahara, H. Toyama, S. Gupta, N. Miura, Electrochem. Commun. 9 (2007) 2315.

# CHAPTER II

## Theoretical Background of Electrodeposition Method, Thin Film Characterization Techniques and Supercapacitor

## CHAPTER II

## 2. Introduction: Thin Film Deposition Methods

One of the great challenges for today's information-rich, mobile society is providing high-efficient, low-cost and environmental friendly electrochemical energy conversion and storage devices for powering an increasingly diverse range of applications, ranging from portable electronics to electric vehicles (EVs) or hybrid electric vehicles (HEVs) [1]. As the performance of these devices depends intimately on the properties of their materials, considerable attention has been paid to the research and development of key materials [2]. Micrometer-sized bulk materials are reaching their inherent limits in performance and cannot fully satisfy the increasing needs of consumer devices. Therefore, rapid development of new materials with high performance is essential. As the identification of conventional bulk materials are carried out via arrangement of their constitute atoms or molecules in three-dimensional periodic order and this is responsible for the final structure or nature of the material, on which the physico-chemical properties of the materials are mainly dependent. But for thin films, the solid system possesses periodicity at most in two-dimensions, causing the enormous variation in its resulting physico-chemical properties than that of the bulk material.

A variety of nanometer size effects have been found in the materials used in electrochemical energy conversion and storage devices, which can be divided into two types: i) 'trivial size effects', which rely solely on the increased surface-to-volume ratio and ii) 'true size effects', which also involve changes of local materials properties [1]. Thin film technology has wide spread applications in various fields such as, optics, magnetism, electricals, electronics, sensors, energy storage systems (electrochemical devices), coatings etc. However, nanocrystalline form of materials offers enlargement in active surface area, enhancement in diffusivity, electrical

resistivity and hardness with reduction in density, thermal conductivity, etc in comparison with conventional coarse-grained materials.

A new technology boasting potentials to facilitate foremost advances in energy storage has emerged as supercapacitors. One of the most important and large scale applications of supercapacitors is in a load leveling function, hybridized either with fuel cells or with rechargeable batteries, for electrical vehicle systems [3-5]. Though, pseudocapacitors have higher capacity than batteries, conventional plate capacitors and double layer capacitors, it suffers through disadvantage of high raw material cost and process difficulty. Conversely, supercapacitve electrode in the thin film form might overcome the above disadvantages [6]. Nanostructured materials offer superior electrochemical performance because of the ability to access both bulk and surface properties. The advantages of using nanostructured materials for electrochemical energy storage have largely focused benefits associated with short path lengths offering a unique prospect to tailor power density and energy density, enabling an intermediate state between batteries and supercapacitors to be realized [4-6]. Currently, interest in micro-scale power sources, such as thin-film batteries (TFBs) and thin-film supercapacitors (TFSCs), has risen because of their use as power sources in microelectronic mechanical systems (MEMs) and nanoelectronic mechanical systems (NEMs). TFBs are suitable for use in most of these devices as a result of their high energy density, rechargeability and safety in operation. But their poor ability to deliver high power over limited time intervals restricts application in the startup of some MEMs or NEMs, which require a large burst of power to be delivered in a very short time. To meet this particular demand, the fabrication of high-quality TFSCs with high power density and long cycle life has received considerable attention in recent years [7].

The properties of thin films are depending on the method of deposition. The essential properties and flexibility can be achieved by choosing appropriate deposition method for thin films. Mainly, thin film deposition methods can be classified into physical (Top-Down) and chemical (Bottom-Up) approach. In physical methods, vacuum evaporation and sputtering are enclosed [8]. The chemical methods include the gas phase chemical processes such as conventional chemical vapor deposition (CVD), laser CVD, photo CVD, metal organo-chemical vapor deposition (MOCVD) and plasma enhanced CVD. Liquid phase chemical methods include electrodeposition (ED), chemical bath deposition (CBD), modified chemical bath deposition (M-CBD), successive ionic layer adsorption and reaction (SILAR), anodization, spray pyrolysis, liquid phase epitaxy, sol-gel method, etc. The chemical method incorporated with growth from chemical solution [9]. The physical methods have major drawbacks such as high working temperature, small area of deposition, requirement of sophisticated instruments, high cost system, wastage of depositing material, cleaning after each deposition, etc. Chemical methods are simple, economic and convenient for the deposition of metal chalcogenide, hydroxides and materials with complex chemical compositions in the thin film form [8-10]. The preparative parameters such as concentration, pH, nature of the complexing agent, temperature, etc are easily controllable. The low temperature deposition avoids oxidation and corrosion of metallic substrates. Chemical method results into pinhole free and uniform deposition. Therefore, these soft solution chemical processes are useful for the preparation of the nanocrystalline particles. Such processes include sol-gel, atomic layer deposition, spray pyrolysis, dip coating, spin coating, solution hydrolysis, chemical bath deposition (CBD), electrodeposition, etc. The broad classification of thin film deposition techniques is summarized in chart 2.1.

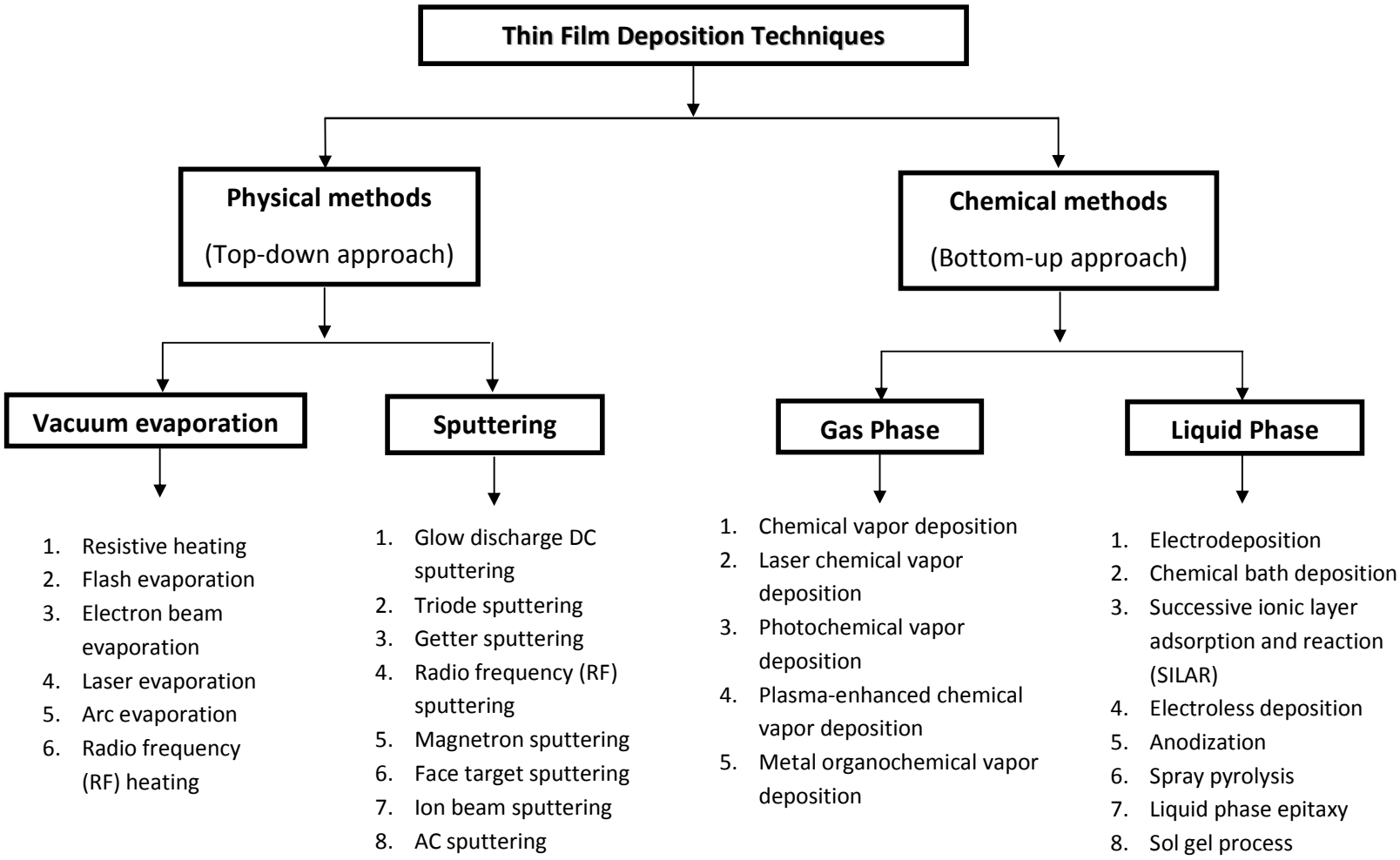


**Chart 2.1** Classification of thin film deposition methods.

## SECTION (I)

## THEORETICAL BACKGROUND OF ELECRODEPOSITION METHOD

### 2. A. 1 Introduction:

Electrodeposition is outstandingly multipurpose technique having precious applications and being explores new inventions due to occurrence of process at an atomic level. This method is renowned because of its economical and easy processability for metallic coatings. The shiny coating of one metal on to other can be fascinatingly achieved via electrodeposition, just by oxidation-reduction reaction (i.e exchange of electrons with ions) in the solution. The difficulties encountered during the synthesis of inorganic solids, on account of the limitations of diffusion in the solid state have been traditionally overcome (i) by reducing the particle size of the reactants or (ii) by eliminating the need for diffusion altogether by the use of solid solution or compound. These two strategies have led to the development of a plethora of low temperature routes to the synthesis of inorganic solids. A third strategy, which is applicable in the event of (i) the diffusing species being charged and (ii) the diffusion medium (more commonly called the host lattice) being porous, layered or defective is to induce diffusion by the application of an electric potential. This strategy can lead to the desired product even at room temperature. This technique, traditionally referred to as "electrosynthesis" has been included among the synthetic techniques available to the solid-state chemist.

Wide range of nanostructured materials can be synthesized via electrodeposition. Primly, electrodeposition is widely exploited as hard and soft coatings for protective and decorative purposes, which have been found exigently new applications in the electronics industry, includes the development of thin film magnetic recording heads for hard disks, thin

conducting coatings for printed circuit boards (PCB), etc [11]. Electrodeposition is one of the smart and convenient techniques and has become captivating due to its several advantages over the other physical and chemical methods. The semiconductor properties like n-type or p-type conductivity; band gap variation, control over stoichiometry, doping, etc can be easily controlled with accuracy. Up till now, many materials such as, metals, semiconductors, ceramics, superconductors, conducting polymers, oxides, hydroxides, etc thin films have been deposited by electrodeposition.

Remarkable distinction of electrodeposition from the chemical reaction is the controlled way in which chemical substances produce. Following are the fascinating features; mostly crucial for deposition of thin films via electrodeposition.

1. Deposition of various structures and compositionally tailored alloys and compounds can be carried out, which is difficult by other deposition techniques.
2. It is an isothermal process in which, the thickness and morphology of the films can be easily controlled by electrochemical parameters such as electrode potential and current (charge).
3. Relatively uniform films can be obtained on substrates of complex shape.
4. It usually has low operating temperature oftenly, room temperature deposition can be carried out which facilitates to form the semiconductor junctions without interdiffusion.
5. Unlike gas phase methods, toxic gases need not to be used.
6. The deposition rate is optimum for good quality of films as compared to other physical and chemical methods.

7. The equipments needed are not expensive and does not require sophisticated instrumentation for controlling high temperature, vacuum etc.
8. Reactions involved in the deposition course occur closer to the equilibrium compared to many gas phase methods and processes can be controlled more accurately and easily.
9. Apart from the obvious advantages in terms of energy saving the low deposition temperature avoids high temperature effects such as interdiffusion, contamination and dopant redistribution.
10. Also, direct cathodic electrodeposition from aqueous and non-aqueous baths is possible and it can be employed as one of the steps in the preparation of semiconductors or oxides.

Mainly, electrodeposition comprises three modes for deposition

1. Galvanostatic:- under constant current,
2. Potentiostatic:- under constant voltage and
3. Potentiodynamic:- under voltage and current variation with time.

### 2. A. 1.1 Fundamentals of electrodeposition:

Usually electrochemical processes involve an exchange of electrons or ions between the electrode and the electrolyte. The driving force is the difference in the electrochemical potential of the transferring species and therefore depends on the electrode potential. Generally, deposition of metal atoms onto any conducting substrate by passing direct current through solution containing metal salt to be deposited is carried out by electrodeposition. The typical electrodeposition set up basically includes three major components as,

1. Cathode and anode (electrodes)
2. Electrolyte (salt solution)

3. Source of electricity (D.C. Power supply)

The schematic diagram of electrodeposition set-up is shown in figure. 2.1.

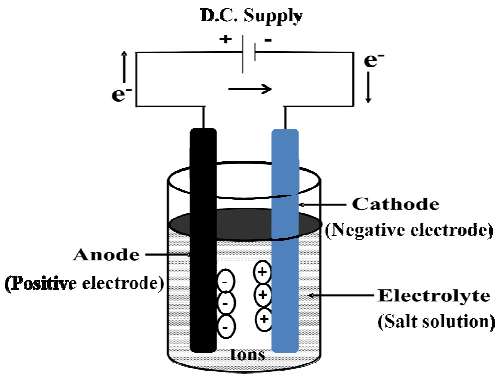


**Fig 2.1** Schematic diagram of electrodeposition.

In a liquid, all surface sites of metal electrode are equivalent and the deposition of a metal ion from the solution is conceptually simple. The ion loses a part of its solvation sheath, transferred to the metal surface and discharged simultaneously; after a slight rearrangement of the surface atoms it is incorporated into the electrode. Means, by passage of direct current through dipped cathode-anode in electrolyte solution containing the metal ions, the metal ions get attracted towards the negatively charged cathode, get neutralized electrically by acquiring electrons and deposited on cathode. The deposition process is managed by controlling the amount and rate of charge passing through electrolyte. Hence, electrical energy is used for chemical change. The metal cations from the electrolyte get deposited onto cathode as explained by following reaction.

$$X^{n+} + ne^- \rightarrow X \qquad [2.1]$$

For the electrolyte containing more than one ionic species, simultaneously deposition of ions occurs at cathode. For two types of ionic species, process can be explained by reaction

$$X^+ + e^- \rightarrow X \qquad [2.2]$$

$$Y^+ + e^- \rightarrow Y \qquad [2.3]$$

---

$$\text{Or} \quad X^+ + Y^+ + 2e^- \rightarrow XY \qquad [2.4]$$

Electrolysis in the electrolyte results into simultaneously deposition of metal cations onto cathode and dissolution of anode in the solution. According to Faraday's law, the amount of deposition and dissolution is determined by the quantity of electricity passed. Faraday established the relationship for amount of electricity passed through the electrolyte solution to occur chemical change in the form of deposition or liberation of solid material at the electrode. This can be mathematically written as,

$$W \propto Q \qquad [2.5]$$

where, W- is the amount of substance liberated in grams, Q- is the quantity of electricity, in coulombs. But Q = current (I)* time (t).

$$W \propto I\,t$$

$$W = z\,I\,t \qquad [2.6]$$

Where, z is 'electrochemical equivalent' (proportionality constant) and can be defined as, "*The amount of substance liberated (in gm) at the electrode by passing 1 coulomb of electricity or a current 1 Ampere for 1 second"*.

While, if same quantity of electricity is passed through different electrolytes, then the amount of substance liberated on the respective electrodes will be in the ratio of their equivalent weights. This is known as Faraday's second law.

## 2. A.1.2 Various steps associated with electrodeposition process:

Following are the consecutive stages involved in the electrodeposition of ionic species from the electrolyte as schematically shown in figure 2.2

1. Ionic transport,
2. Discharge,
3. Breaking of ion-ligand bond (in case of complexed bath solution), and
4. Incorporation of adatoms on to the substrate followed by nucleation and growth.

All above four stages occur within the region 1–1000Å from the substrate; though each has its own region of operation. These various processes can be classified regarding distance from the electrolyte as [12]:

I. In the electrolyte,
II. Near the electrode, and
III. At the electrode

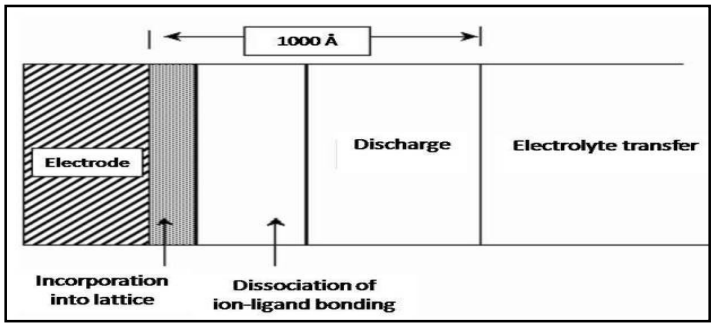


**Fig 2.2** Estimated regions through which various stages of ion transportation take place for electrodeposition.

### I. Processes occurred in the electrolyte

The movement of ions in the electrolyte towards the electrode takes place under the influence of

a. Potential gradient results in to drifting of ion, dϕ/dx.
b. Concentration gradient leading to diffusion of ions, dc/dx.
c. A density convective current, dρ/dx due to consumption of ions at the electrode.

All these processes can be written mathematically by Nernst-Planck equation,

$$j = zF\left(\frac{D_C}{RT}\frac{d\varphi}{dx} + D\frac{dc}{dx} + \quad cv\right) \qquad [2.7]$$

Where, F- is the Faraday's constant, ν- is the viscosity of the electrolyte, R- is the gas constant and D- is the diffusion coefficient. The three terms in the parenthesis respectively illustrates the contributions of migration, diffusion and convection processes to the mass transport towards the electrode.

**II. Processes occur near the electrode but within electrolyte**

Generally, ionic species are surrounded by a hydration sheath or by other complex forming ions or ligand present in the electrolyte. They move together as a single entity and arrive near the electrode surface where the ion-ligand system either accepts electrons from the cathode (or donates electrons to the anode). This ionic discharge occurs between 10 to 1000 Å distance from the electrode.

**III. Processes occur on the surface of electrode**

The electrically neutral (discharged) ions arrive near the electrode, where they lead to the form a new solid phase or the growth of an electrodeposit step by step. The deposited atoms have a tendency to form either an ordered crystalline phase or a disordered amorphous phase. The steps of transport, discharge, nucleation and growth are interlinked in the electrodeposit formation.

Ions are much heavier than electrons. While electrons can easily tunnel through layers of solution 5–10 Å thick and protons can tunnel over short distances, up to a few tenths of an angstrom, ions do not tunnel at all at room temperature. The transfer of an ion from the solution to a metal surface can be viewed as the breaking up of the solvation cage and subsequent deposition, the reverse process as the jumping of an ion from the surface into a preformed favorable solvent configuration. Schematic diagram for transfer of an ion from the solution onto the electrode surface is shown in figure 2.3.

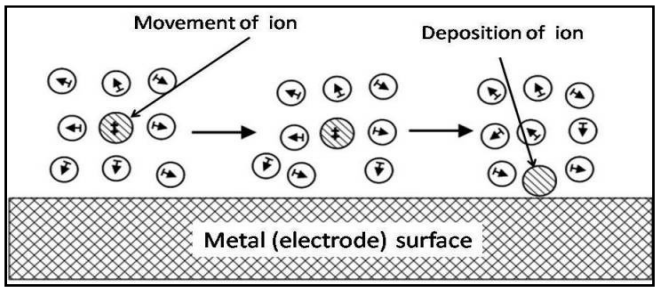


**Fig. 2.3** Schematic of ion transfer from solution onto the electrode surface.

### 2. A.1.3 Pathways for the growth of an electrodeposit

The surface of a solid metal offers various sites for metal deposition.

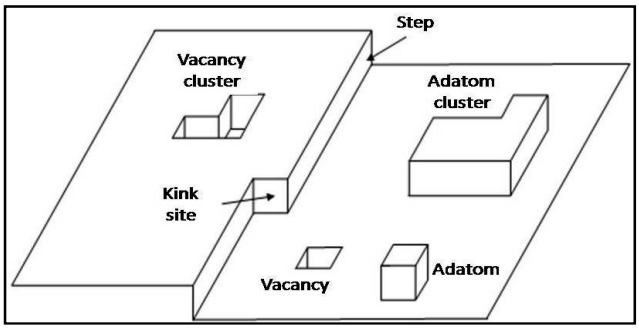


**Fig. 2.4** Schematic diagram for a metal surface with few characteristic features.

Figure 2.4 shows a schematic diagram for a crystal surface with a quadratic lattice structure. A single atom sitting on a flat surface plane is denoted as an adatom; several such atoms can form an adatom cluster. A vacancy is formed by a single missing atom; several vacancies can be grouped to vacancy clusters. Steps are particularly important for crystal growth, with kink atoms, or atoms in the half-crystal position, playing a special role. When a metal is deposited onto such a surface, the vacancies are soon filled. However, the addition of an atom in the kink position creates a new kink site; so at least on an infinite plane the number of kink sites does not change and the current is maintained by incorporation into these sites. Similarly, the removal of a kink atom creates a new kink site. In the limit of an infinitely large crystal, the contribution of other sites can be neglected.

There are two different pathways for metal deposition: (1) direct deposition from the solution onto a growth site and (2) the formation of an adatom with subsequent surface diffusion to an edge. Both mechanisms seem to occur in practice. If direct deposition is the dominant mechanism, the concentration of the supporting electrolyte is sufficiently high to eliminate double-layer effects and it appears that metal deposition and growth can be viewed as a propagation of steps. On a perfect but finite metal plane any propagating step must at some time reach the edge and the growth sites disappear. The entire pathway for the growth can be divided into following steps.

1. Transport of ions in the electrolyte bulk towards the interface.
2. Discharge of ions reaching the electrode surface, giving rise to generation of adatoms.
3. Nucleation and growth, where again alternative routes are possible
    i. Growth governed due to surface diffusion.

ii. Growth governed due to clusters formation and critical nuclei.

iii. Monolayer formation and final growth of electrodeposit.

**2. A.1.4 Initial stages of deposition:**

Consider a flat metal substrate, on which metal atoms are deposited; there are several principle mechanisms.

**1. Stronger interaction between metal atoms:**

In this case, three-dimensional clusters are formed from the beginning. Obviously, this cannot take place at underpotentials. On the contrary, nucleation usually requires overpotential for deposition to occur. This mechanism is known as Volmer–Weber or three-dimensional island growth as shown in figure 2.5 (a).

**2. Stronger interaction between metal atom and substrate:**

If the interaction of the deposited atoms with the substrate is stronger than with its own kind, a monolayer of metal atoms on substrate can be deposited at underpotential. There are two subcases

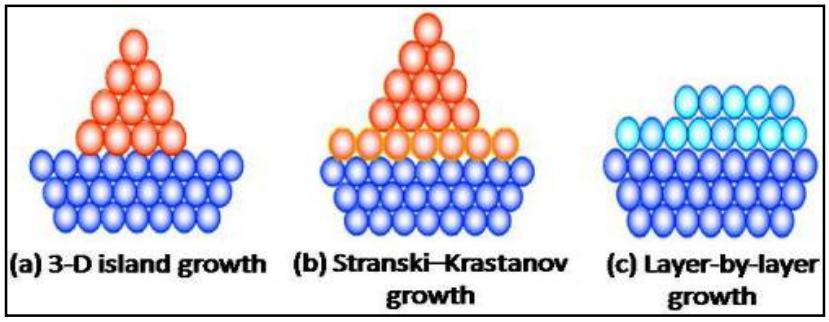


**Fig 2.5** Schematic of three growth modes (a) 3-D island growth (Volmer–Weber), (b) Stranski–Krastanov growth, (c) layer-by-layer or Frank-van-der-Merwe growth.

A) If there is a considerable mismatch in the lattice structures of metal atoms and substrates atoms, the first layer has a different, often incommensurate structure. Subsequently, three-dimensional clusters are formed. This is denoted as Stranski–Krastanov growth mode as shown in figure 2.5 (b).

B) If there is no large mismatch between the crystallographic structures of the two metals atoms and substrate, a commensurate monolayer is formed. Subsequent layers are also epitaxic and deposited layer-by-layer; this is also known as the Frank-van-der-Merwe growth mode. After two or three layers have been deposited, the influence of the substrate is negligible and the deposition proceeds in the same way as on the bulk metal atom as shown in figure 2.5 (c).

Various possibilities exist for the combination of reaction steps during electrodeposit course. Oftenly, charge transfer can occur only with adsorbed species, then adsorption/desorption steps are included. Furthermore, chemical reactions may precede or follow the electron transfer step. The mass transport concerns various steps within the reaction chain that forms the cell reaction. Transport of the reacting species is achieved by two mechanisms: diffusion that is caused by the concentration gradient of the concerned species and migration of ions caused by the current.

### 2. A.2 Various modes of electrodeposition method:

### 1) Galvanostatic mode:

The word “galvanostatic” itself revealed the meaning as “at constant current.” In this mode dc current between working and counter electrodes kept constant during deposition course. It is essential to have constant current density for uniform deposition. Generally, cathodic deposition (i.e.

working electrode at -ve potential) is preferred. The deposition rate is proportional to the corresponding limiting current densities. As the codeposition depends upon optimum value of current density to be chosen correctly, so the galvanostatic electrodeposition of compound semiconductor is difficult. Following are the important features of galvanostatic mode.

i) Easy controls of the current between counter electrode and working electrode within selected current range.
ii) Counter electrode is driven to the required potential to generate the desired cell current.
iii) Reference electrode is only used to measure potential at some point in electrochemical cell and not for controlling the current.
iv) As constant current density is supplied, output waveform gives the variation of cell potential with respect to time.

**2) Potentiostatic mode:**

The word "potentiostatic" itself revealed the meaning as "at constant dc voltage or potentail." In this mode, various charge transfer reactions continue under a steady-state condition at appropriate rates to the steady-state interfacial overpotential and exchange current density. The preference of overpotential depends on the parameters such as, bath composition, nature of substrate and the reversible potential of the species to be deposited. The standard electrode potentials are useful as an approximate guide in finding the possible potential of a particular species to be electrodeposited. However, the actual deposition potential depends on number of factors such as, interaction of substrate-depositant, hydrogen overvoltage, interaction between the components during compound electrodeposition and the polarization characteristics of the bath. Following are the important features of potentiostatic mode.

i) Primly, this mode controls the potential of working electrode accordingly reference electrode.
ii) The potential at counter electrode is driven to the required potential to establish the desired working electrode potential.
iii) As constant potential is appiled, output waveform gives the variation of cell current with respect to time.

**3) Potentiodynamic mode (Cyclic Voltammetry)**:

In cyclic voltammetry, the voltage is swept between two values at a fixed rate (i.e. within given potential window), however when the voltage reaches $V_2$ the scan is reversed and the voltage is swept back to $V_1$. This result schematically presented in figure 2.6 (a), (b). Furthermore, figure 2.6 (b) includes a typical cyclic voltammogram for a reversible single electrode transfer reaction, wherein $V_1$, $V_2$ are potential limits, $I_p^C$ , $I_p^a$ are the cathodic and anodic peak currents and $E_p^C$, $E_p^a$ are cathodic and anodic peak voltages of resulted voltammogram. This technique is often used to establish voltage limits but is also important because the measured current is directly relatable to the capacitance in the most straightforward interpretation of the theory as,

$$I(t)=C\,(dv/dt) \qquad [2.8]$$

Due to electrochemical process which occurred entirely in the solution phase, results a new solid phase formation on the substrate surface due to the redox state. The solid phase must be formed by oxidation process. Metal oxides can be deposited in single step by using this method. Film formation involves the reduction of metal ion at reduction potential on substrate successively followed by oxidation at oxidation potential of metal ions.

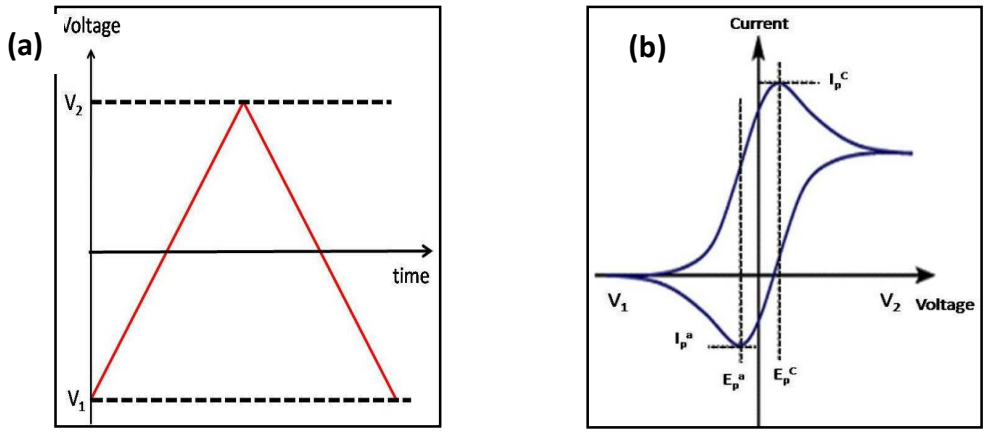


**Fig.2.6** (a) Schematic of cyclic voltammetry (b) a typical cyclic voltammogram for a reversible single electrode transfer reaction.

Several repeated cycles can furnish a desired thickness of the film following by layer by layer deposition.

Following are the important features of potentiodynamic mode.

i) It measures the current during triangular potential sweep and observes both the anodic and cathodic responses.
ii) The output waveform has both forward and reverse peaks that provide information concerning electroactivity of electrode or the solution.

## SECTION (II)
## THIN FILM CHARACTERIZATION TECHNIQUES

### 2. B Fundamentals of characterization techniques:

An effective implementation of synthesized materials in respective field applications is based on their numerous physico-chemical properties. The complete characterization of any material consists of structural, phase as well compositional and micro-structural analysis, surface studies, etc; which have great significance towards properties of materials for evaluation. One has to characterize the films to achieve optimum performance of the prepared films, before using them in application. Characterization techniques play crucial role in categorizing and marking the prepared materials properly, according to their suitability in the applications. Also characterization techniques help to explain reasons behind various phenomena occur and assist to establish scientific support to the proposed theories. Understanding of different properties of the films along with growth mechanism can be possible only by characterization of the films.

### 2. B.1 Thickness measurement

As the materials are deposited in the thin film form, the thickness of the film is most crucial factor that can affect the thin films properties significantly. The thickness of the deposited material (film) can be measured either in-situ by monitoring the rate of the material deposition or after the deposition of film by taking out form the deposition chamber. As mentioned the first type of technique usually referred as monitor methods; generally facilitate both monitoring and controlling of deposition rate of the film thickness. Any known physical quantity associated to film thickness can be used to measure the thickness. Though, the method

chosen should be suitable, consistent and easy. One of the most convenient and reliable method for determining film thickness is gravimetric method. This comprises area (A) and weight (M) of the film for measurement. The average thickness (t) is obtained by using the formula [13].

$$t = \Delta M/A\rho \qquad [2.9]$$

$$\Delta M = M_1 - M_2 \qquad [2.10]$$

where, 't'- thickness of the film, 'ΔM'-mass of the film material, 'A' - area of the film, '$M_1$' -mass of the substrate with film, '$M_2$' -mass of the substrate without film and 'ρ' -density of the deposited material. In order to acquire more accuracy in results, one should have to measure thickness using the films with maximum area. So that, weight difference is accurately measurable. Even though the actual density of the material in thin film form is lower, the 'ρ' value is usually taken for the bulk material. Hence, this method is quite destructive as, actual density of material is different than the material in the film form. Also, in case of porous thin films, the density of deposited material will not be well defined so, thickness of thin film can be calculated in terms of deposited mass per unit area of the material only. Therefore, the equation (2.10) modifies to

$$t = M/A \qquad [2.11]$$

## 2. B.2 X-ray diffraction (XRD) technique

The X-ray diffraction (XRD) is a powerful technique used to uniquely identify the crystalline phases present in materials and to measure the structural properties (strain, grain size, epitaxy, phase composition, preferred orientation and defect structure) of these phases. The XRD is noncontact and nondestructive, which makes it ideal for in situ studies. The intensities measured with XRD can provide quantitative, accurate information on the atomic arrangements at interfaces (e.g. in

multilayers). Materials composed of any element can be successfully studied with XRD [14]. As a consequence, the sensitivity of XRD depends on the material of interest. Superior detection methods for x-ray, the availability of commercial monochromators and intense microfocus x-ray sources have made x-ray diffraction method applicable to films as thin as 100 Å.

Figure 2.7 shows the basic features of an XRD experiment, where the diffraction angle 2θ is the angle between the incident and diffracted x-rays. Typically, the diffracted intensity is measured as a function of 2θ and the orientation of the specimen, which yields the diffraction pattern. The x-ray wavelength λ is typically 0.7-2 Å, which corresponds to x-ray energies.

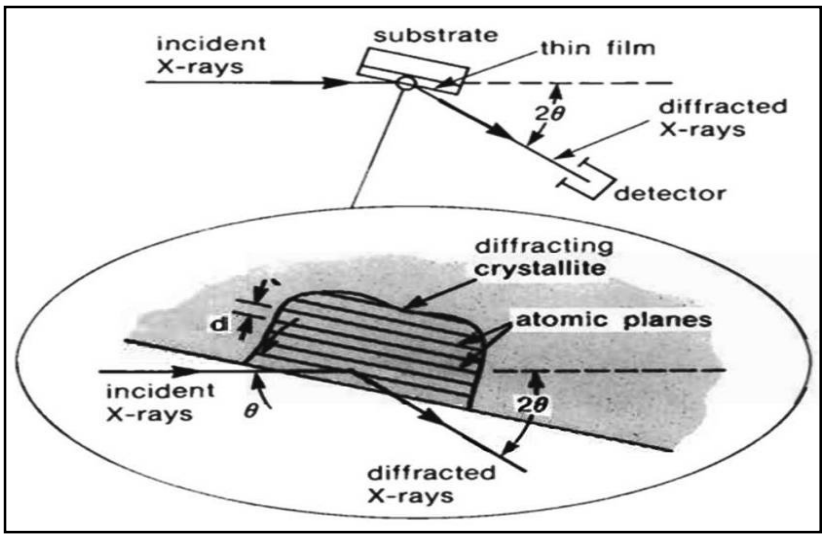


**Figure 2.7** Basic features of a typical XRD experiment.

This technique employs a chromator to provide a diffracted beam, which is further diffracted from the film surface oscillating about the mean diffraction position. The x-ray diffraction technique based on monochromatic radiation is more important because the spacing of the planes (d-spacing) can be deduced from the observed diffraction angles. The phenomenon of x-ray diffraction can be considered as reflection of x-

rays from the crystallographic planes of the material and is governed by the Bragg's equation.

$$2d \sin \theta = n \lambda \qquad [2.12]$$

Where, d– is the lattice spacing, λ– is the wavelength of the monochromatic x-ray, n– is the order of diffraction and θ– is the diffraction angle. The 'd' values are calculated using above relation for known values of θ, λ and n.

This method permits the size of crystals to be determined, but not the size of the particle itself. Crystalline size is usually smaller than particle size. For single crystalline nanoparticles, the crystalline size approximates the particle size. Fortunately, if a nanoparticle is crystalline, it usually appears as single crystal so that the crystalline size is the same as the particle size. The size of a nanocrystal can be predicted using XRD data by combining the Scherrer and Warren formulae. The broadening of the XRD peaks reflects either crystallinity or the size of nanocrystal. Assuming that the crystallinity of nanoparticles is not too different, the broadening of the XRD peaks reflects the size of nanocrystals only; smaller the nanocrystals, wider the reflection peak. The crystalline size in a sample from XRD patterns is predicted using the Scherrer formula.

$$d = 0.9\lambda / (\beta \cos\theta) \qquad [2.13]$$

where, d- is the crystalline diameter, λ- is the wavelength of x-ray, and θ- is the Bragg angle, β- is the line broadening, obeys the Warren formula

$$\beta^2 = (\beta_M)^2 - \beta_S)^2 \qquad [2.14]$$

Where, $\beta_M$ –the measured peak width at half the peak height of the sample and $\beta_s$- the corresponding width of a standard material having a large crystalline size mixed with the sample with diffraction peak near the relevant peak of the sample. Figure 2.8 illustrates these peaks. For large

crystalline materials, the XRD peaks are very narrow, while for nanocrystalline materials, the XRD peaks are broad. Thus, an approximation of $\beta_M >> \beta_S$ or $\beta \cong \beta_M$ is usually used [15].

Thin films contain many grains or crystallites (small crystalline regions) having a distribution of orientations. If this distribution is completely random, then diffraction occurs from any crystallite that happens to have the proper orientation to satisfy the diffraction conditions. The diffracted x-rays emerge as cones about the incident beam with an opening angle of $2\theta_{hkl}$, creating a "powder" diffraction pattern.

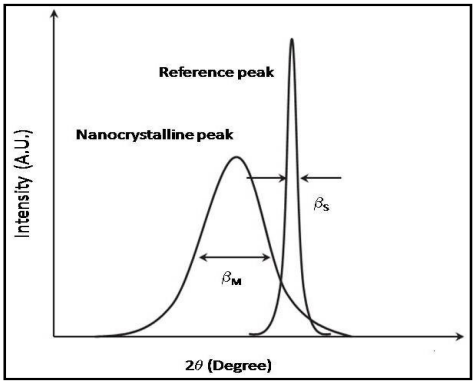


**Fig 2.8** Schematic diagram of XRD peaks for nanoparticles and a reference sample.

Thin films are frequently in a class of materials intermediate between single crystals and powders and have fiber texture. That is, all the crystallites in the film have the same atomic planes parallel to the substrate surface, but are otherwise randomly distributed. The XRD provides phase identification of the materials. This identification is done by comparing the measured 'd' spacings in the diffraction pattern and to a lesser extent, their integrated intensities with known standards in the JCPDS Powder Diffraction File (Joint Committee on Powder Diffraction Standards) or American Standard for Testing of Materials (ASTM).

However, thin films often have a preferred orientation and this can cause the measured intensities to disagree with the JCPDS file, which are for random orientations. For films containing several phases, the proportion of each phase can be determined from the integrated intensities in the diffraction pattern. The sample used may be in the powder, single crystal or thin film form.

### 2. B.3 FT-IR spectroscopy

The physical principles underlying infrared spectroscopy have been appreciated for more than a century. As one of the few techniques, FT-IR can provide information about the chemical bonding in a material particularly useful for the nondestructive analysis of solids and thin films. Chemical bonds vary widely in their sensitivity to probing by infrared techniques. For example, carbon-sulfur bonds often give no infrared signal and so cannot be detected at any concentration. But, silicon-oxygen bonds can produce signals intense enough to be detected when probing submonolayer quantities, or on the order of $10^{13}$ bond/cc. Thus, the potential utility of infrared spectrophotometry (IR) is a function of the chemical bond of interest, rather than being applicable as a generic probe. The goal of the basic infrared experiment is to determine changes in the intensity of a beam of infrared radiation as a function of wavelength or frequency (2.5- 50 μm or 4000-200 $cm^{-1}$, respectively) after it interacts with the sample. The centerpiece of most equipment configurations is the infrared spectrophotometer. Its function is to disperse the light from a broadband infrared source and to measure its intensity at each frequency. The ratio of the intensity before and after the light interacts with the sample is determined. The plot of this ratio versus frequency is the infrared spectrum.

FT-IR stands for Fourier Transform Infrared, the preferred method of infrared spectroscopy. An infrared spectrum represents a fingerprint of a sample with absorption peaks which correspond to the frequencies of vibrations between the bonds of the atoms making up the material. Because each different material is a unique combination of atoms, no two compounds produce the exact same infrared spectrum. Therefore, infrared spectroscopy can result in a positive identification (qualitative analysis) of every different kind of material. In addition, the size of the peaks in the spectrum is a direct indication of the amount of material present. With modern software algorithms, infrared is an excellent tool for quantitative analysis. In infrared spectroscopy, IR radiation is passed through a sample. Some of the infrared radiation is absorbed by the sample and some of it is passed through (transmitted). The resulting spectrum represents the molecular absorption and transmission, creating a molecular fingerprint of the sample. Like a fingerprint no two unique molecular structures produce the same infrared spectrum. This makes infrared spectroscopy useful for several types of analysis [16].

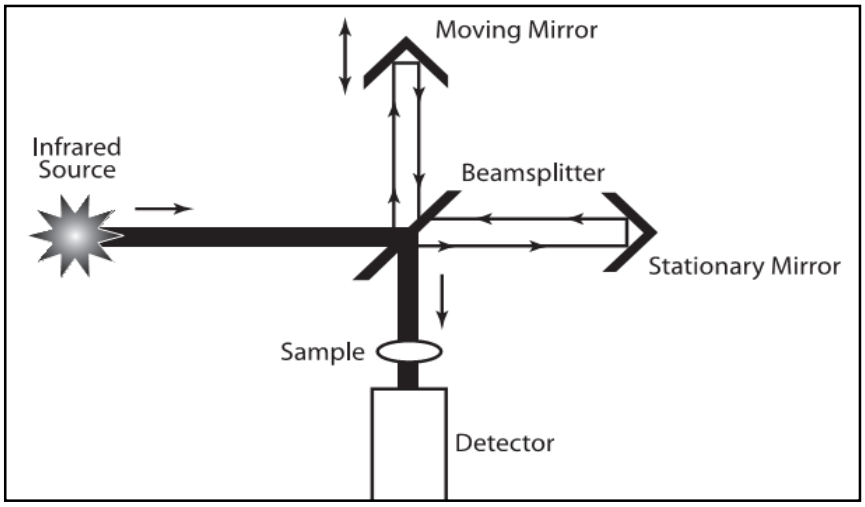


**Fig. 2.9** Schematic diagram of interferometer.

A Michelson interferometer as the dispersing element, gained increasing acceptance shown in figure 2.9. All frequencies emitted by the interferometer follow the same optical path, but differ in the time at which they are emitted. Thus these systems are referred to as being temporally dispersive. Since the intensity-time output of the interferometer must be subjected to a Fourier transform to convert it to the familiar infrared spectrum (intensity-frequency), these new units were termed Fourier Transform Infrared spectrophotometers, (FT-IR). It has grown to dominate the field of infrared spectroscopy. Experiments in microanalysis, surface chemistry and ultra-thin films are now much more routine. The same is true for interfaces, if the infrared characteristics of the exterior layers are suitable. While infrared methods still are rarely used to profile composition as a function of depth, microprobing techniques available with FT-IR technology permit the examination of micropartides and x-y profiling with a spatial resolution down to 20 μm.

Studies of the spontaneous orientation of dipole moment in semiconductors are carried out by infrared spectroscopy which can provide information regarding atomic arrangement and inter atomic forces in the crystal lattice itself. If the two energy levels $E_1$ and $E_2$ are placed in an electromagnetic field and the difference in the energy between the two states is equal to a constant 'h' multiplied by the frequency of the incident radiation ν, a transfer of energy between the molecules can occur as,

$$\Delta E = h\nu \qquad [2.15]$$

When the ΔE is positive the molecule absorbs energy; when ΔE is negative, radiation is emitted during the energy transfer and emission spectra are obtained. When the energies are such that the equation (2.15) is satisfied, a spectrum unique to the molecule under investigation is

obtained. The spectrum is usually represented as a plot of the intensity Vs the frequencies and peaks occur when the equation (2.15) is satisfied. Frequency ranges in this spectrum vary from those of 'γ' rays (wavelength of about $10^{-10}$ cm) to radio waves (wavelength of $10^{10}$ cm). Mostly, spectroscopic investigations are carried out close to visible light, which includes UV, visible and IR region (between wavelength of $10^{-6}$ and $10^{-3}$ cm). Both the atoms and molecules give rise to spectra but they differ from each other. The difference between the atomic and molecular spectra lies in the nature of energy levels involved in the transitions. In the atom, the absorption represents transition between the different allowed states for the orbital electrons. In case of molecules, however, the atoms within the molecules vibrate and the molecule as a whole rotates. So, total energy contributions are represented by the equation [17].

$$E_{tot} = E_{elect} + E_{vib} + E_{rot} + E_{trans} \qquad [2.16]$$

Where, $E_{elect}$ -the electronic energy, $E_{vib}$ -the vibrational energy, $E_{rot}$ -the rotational energy and $E_{trans}$ -the translation energy. The separate energy levels are quantized and only certain transitions of electronic, vibrational and rotational energy are possible. Usually translational energy is sufficiently small and can be ignored. The vibrational spectrum of a molecule is considered to be a unique physical property and is a characteristic of the molecule [18]. As such the infrared spectrum can be used as a finger print for identification, in support of x-ray diffraction technique for the purpose of characterization. Infrared spectra were usually published in the transmittance format, because the goal of the experiment was to obtain qualitative information.

## 2. B.4 Scanning electron microscopy (SEM):

For the purpose of a detailed materials characterization, Scanning Electron Microscope (SEM) as a potent instrument is widely preferred. The SEM provides the investigation with a highly magnified image of the surface of a material that is very similar to what one would expect if one could actually "see" the surface visually. This tends to simplify image interpretations considerably. High-resolution imaging of SEM provides more topographical information of the material surfaces. The resolution of the SEM can approach a few nm and it can operate at magnifications that are easily adjusted from about 10X to 300,000X and greater depth of field up to 100 times than that of optical microscopy [19].

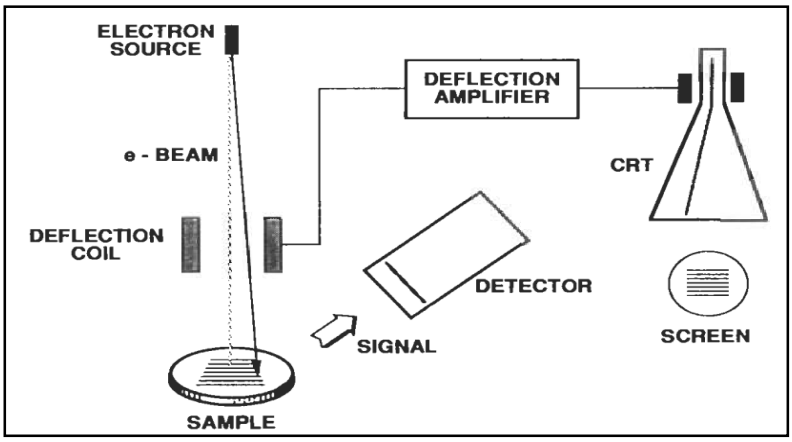


**Fig 2.10** Schematic for the operation of SEM.

In the SEM, a source of electrons is focused (in vacuum) into a fine probe that is rastered over the surface of the specimen as shown in Figure 2.10. As the electrons penetrate the surface, a number of interactions occur that can result in the emission of electrons or photons from (or through) the surface. A reasonable fraction of the electrons emitted can be

collected by appropriate detectors, and the output can be used to modulate the brightness of a cathode ray tube (CRT) whose x and y inputs are driven in synchronism with the x-y voltages rastering the electron beam. In this way an image is produced on the CRT; every point that the beam strikes on the sample is mapped directly onto a corresponding point on the screen [20].

The principle images produced in the SEM are of three types: secondary electron images, backscattered electron images and elemental x-ray maps. Secondary and backscattered electrons are conventionally separated according to their energies. They are produced by different mechanisms. When a high-energy primary electron interacts with an atom, it undergoes either inelastic scattering with atomic electrons or elastic scattering with the atomic nucleus. In an inelastic collision with an electron, some amount of energy is transferred to the other electron. If the energy transfer is very small, the emitted electron will probably not have enough energy to exit the surface. If the energy transferred exceeds the work function of the material, the emitted electron can exit the solid. When the energy of the emitted electron is less than about 50 eV, by convention it is referred to as a secondary electron (SE), or simply a secondary. Most of the emitted secondaries are produced within the first few nm of the surface. Secondary electrons produced much deeper in the material suffer additional inelastic collisions, which lower their energy and trap them in the interior of the solid. Higher energy electrons are primary electrons that have been scattered without loss of kinetic energy (i.e., elastically) by the nucleus of an atom, although these collisions may occur after the primary electron has already lost some of its energy to inelastic scattering. Backscattered electrons (BSEs) are considered to be the electrons that exit the specimen with an energy greater than 50 eV, including Auger electrons. However, most BSEs have energies comparable to the energy of

the primary beam. The higher the atomic number of a material, the more likely it is that backscattering will occur. In most currently available SEMs, the energy of the primary electron beam can ranges from a few hundred eV up to 30 keV [21]. The SEM generates a beam of electrons in an electron column above the sample chamber. The electrons are produced by a thermal emission source, such as a heated tungsten filament, or by a field emission cathode.

### 2. B.5 Energy-Dispersive X-Ray Spectroscopy (EDS):

An electron beam not only emphasizes imaging in the SEM, but is also concerned with analysis (compositional in particular) of materials which provide fine spatial resolution. Such analytical technique involves fine electron probes specially constructed for an analytical mode. The incoming electron beam interacts with the sample to produce a number of signals that are subsequently detectable and useful for analysis. Energy-dispersive x-ray spectroscopy (EDS or EDX) is an analytical technique used for the elemental analysis or chemical characterization of a sample. It is one of the variants of x-ray fluorescence spectroscopy which relies on the investigation of a sample through interactions between electromagnetic radiation and matter, analyzing x-rays emitted by the matter in response to being hit with charged particles. Its characterization capabilities are due in large part to the fundamental principle that each element has a unique atomic structure allowing x-rays that are characteristic of an element's atomic structure to be identified uniquely from one another. They are x-ray emission, which can be detected either by energy dispersive spectroscopy (EDS) or by wavelength dispersive spectroscopy (WDS).

EDS is an extremely powerful analytical technique of special value in conjunction with electron column instruments. Figure 2.11 shows

schematic of an EDS system on an electron column. The incident electron interacts with the specimen with the emission of x-rays. These x-rays pass through the window protecting the Si (Li) and are absorbed by the detector crystal. The x-ray energy is transferred to the Si (Li) and processed into a digital signal that is displayed as a histogram of number of photons versus energy [20]. When the sample is bombarded by the electron beam of the SEM, electrons are ejected from the atoms comprising the sample's surface. A resulting electron vacancy is filled by an electron from a higher shell, and an x-ray is emitted to balance the energy difference between the two electrons. The EDS x-ray detector measures the number of emitted x-rays versus their energy. The energy of the x-ray is characteristic of the element from which the x-ray was emitted. A spectrum of the energy versus relative counts of the detected x-rays is obtained and evaluated for qualitative and quantitative determinations of the elements present in the sampled volume.

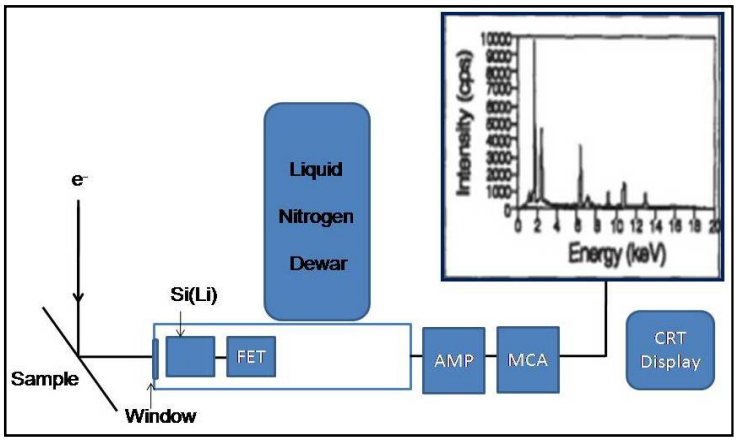


**Fig 2.11** Schematic of an EDS system on an electron column.

With modern detectors and electronics most EDS systems can detect x-rays from all the elements in the periodic table above beryllium, Z= 4, if present in sufficient quantity. The minimum detection limit (MDL)

for elements with atomic numbers greater than Z= 11 is as low as 0.02% wt., if the peaks are isolated and the spectrum has a total of at least $2.5 \times 10^5$ counts.

EDS has been used for quality control and test analysis in many industries including: computers, semiconductors, metals, cement, paper and polymers. EDS has been used in medicine in the analysis of blood, tissues, bones and organs; in pollution control, for asbestos identification; archeology and oceanography; for identification and forgery detection in the fine arts and for forensic analysis in law enforcement. With a radioactive source, an EDS system is easily portable and can be used in the field more easily than most other spectroscopy techniques. The main advantages of EDS are its speed of data collection; the detector's efficiency (both analytical and geometrical); the ease of use; its portability; and the relative ease of interfacing to existing equipment. A major advantage of the energy-dispersive spectrometer is that it can be positioned very close to the sample and can present a large solid angle for the collection of emitted x-rays.

## 2. B.6 Impedance spectroscopy:

Electrochemical impedance spectroscopy (EIS) has been known to the electrochemistry community for more than a century; Macdonald recently published an excellent account of its history [22]. Electrical equivalent circuits (EECs) are merely analogs, rather than models, which described an electrochemical reaction that takes place at the electrode/electrolyte interface, using an EEC as a model. The current flowing at an electrified interface due to an electrochemical reaction, $Ox + ne^- \leftrightarrow Red$, always contains non-faradaic components, no matter how well the measurement is made. In this equation, n is the number of electrons

transferred, O is the oxidant and R is its reduced product (reductant). The electron is transferred across the electrified interface, as illustrated in Figure 2.12.

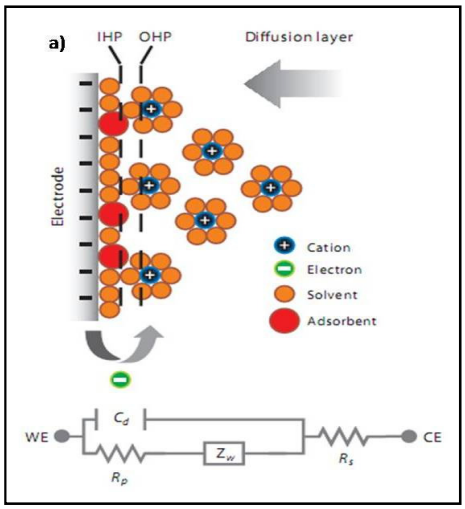


**Fig 2.12.** An EDLC at negative electrode of cell

Figure 2.12 shows at top, an electrified interface in which the electrode is negatively charged; counter cations are aligned along the electrified surface. At bottom are the electrical circuit elements corresponding to each interface component. The high-frequency components are shown on the left and the low-frequency components are shown on the right. where, $C_d$–is the double-layer capacitor, $C_E$– is the counter electrode, IHP- is inner Helmholtz plane, OHP- is outer Helmholtz plane, $R_p$- is polarization resistance, $R_s$- is solution resistance, WE-is working electrode, $Z_W$– is Warburg impedance.

The charge transfer leads to both faradaic and non-faradaic components. The faradaic component arises from the electron transfer via above mentioned reaction across the interface by overcoming an appropriate activation barrier, namely the polarization resistance ($R_p$), along with the uncompensated solution resistance ($R_s$). Then on faradaic

current results from charging the double-layer capacitor ($C_d$). When the charge transfer takes place at the interface, the mass transports of the reactant and product take on roles in determining the rate of electron transfer, which depends on the consumption of the oxidants and the production of the reductant near the electrode surface. The mass transport of the reactants and the products provides another class of impedance ($Z_W$), which can be exploited by electroanalytical chemists because it shows up in the form of a peak current in a voltammogram or a current plateau in a polarogram. The EEC in Figure2.12 shows that each circuit component corresponds to each interfacial component.

Impedance spectroscopy is a powerful method of evaluating a component's performance in the frequency domain. Special equipment is required to apply a small AC voltage and measure the changes in magnitude and phase over a range of frequencies. An ideal capacitor is represented by a vertical straight line shifted on the real axis by its ESR. At low frequencies a supercapacitor approaches a near vertical straight line shifted on the real axis by the ESR.

AC method is commonly used to make a measurement over a wide range of frequencies. The DC value of the conductivity can be extracted from the corresponding AC data. Many AC measurements are performed with blocking electrode such that no discharge or reaction occurs at the electrode-electrolyte interface. Because the current will flow back and forth, no ion pile up is found on the electrode surface, especially when a high AC frequency is used. Commonly used electrodes are platinum, stainless steel, gold and indium tin oxide (ITO) glass.

Impedance is simply the AC resistance of the cell. The value in general contains a real and an imaginary part. An electrochemical cell, in general, exhibits resistive, capacitive, as well as inductive properties. The

resistive property contributes to the real part of the impedance, while the capacitive and the inductive properties contribute to the imaginary part of the impedance. Therefore, an electrochemical cell can be considered to be a network comprised of a resistor, a capacitor, as well as an inductor. The arrangement for such a cell is usually determined after performing a measurement and analyzing the form of the impedance curve. The capacitor presents as an open circuit in a DC network and an inductor that appears as a straight conductor wire in a DC circuit, both appear as imaginary resistors in an AC circuit.

The complex impedance can be written in a general form as

$$Z(\omega) = Z'(\omega) - i\,Z''(\omega) \qquad [2.17]$$

Where, ω- is frequency, Z'(ω)- is real part of impedance, contributed by the resisitive part, Z"(ω)- is imaginary part of impedance, contributed by the capacitive part, $i=\sqrt{-1}$, the imaginary number.

**2. B.7 Contact angle:**

Recently, surface wettability study of solid surfaces receives a great importance in the various fields of research and industrial applications. However, now a day's behaviour of material surfaces switching from superhydrophilic to superhydrophobic is the leading issue of researchers, which is primly helpful according to demand of various applications.

The contact angle tool characterizes the behavior of a liquid on a solid. When a liquid is placed in contact with a solid surface, the bare surface of the solid absorbs the vapor of the liquid until the volatility of the absorbed material is equal to that of the liquid. When equilibrium is established, there is a liquid-solid interface between the two phases gives rise contact angle. The standard contact angle goniometer is a powerful

tool for measuring contact angle and surface energy. The figure 2.13 (a) shows photograph of contact angle goniometer. This instrument is used by researchers and scientists around the world. This tool includes drop image standard as well as fiber optic illuminator, 3-axis leveling stage (X, Y and Z) and high speed digital camera. Each system ships as a complete turn-key system with PC and LCD and microsyringe fixture for manual dispensing. Contact angle ranges from 0 to 180° with accuracy +/- 0.10°.

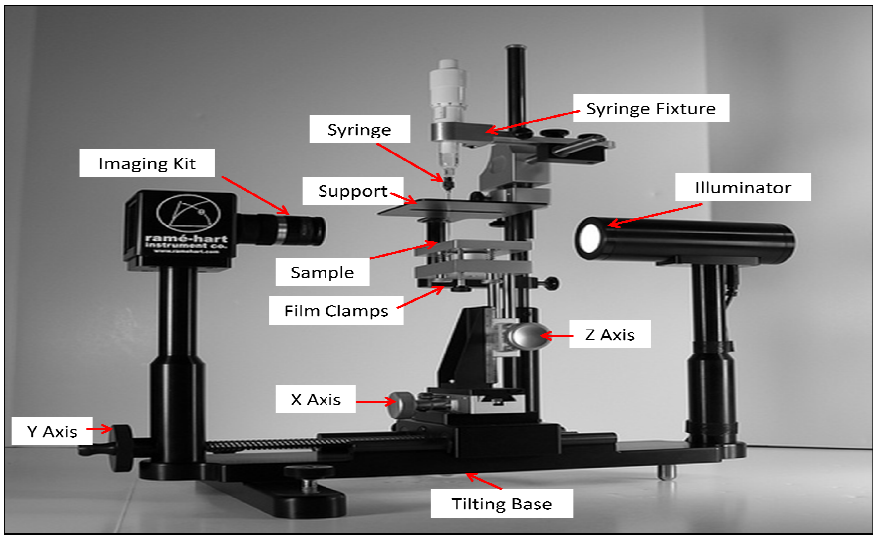


**Fig 2.13 (a)** Contact angle goniometer.

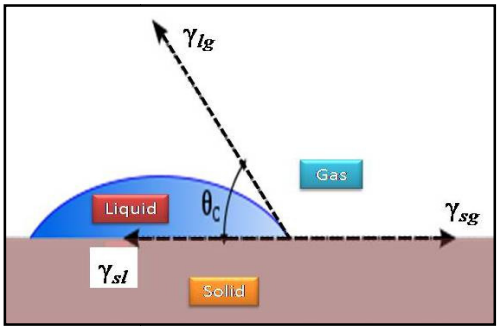


**Fig 2.13 (b)** Contact angle of a solid sample.

The contact angle plays the role of a boundary condition. Contact angle goniometer is used to measure the contact angle of the material. And it is not limited to a liquid/vapour interface; but is equally applicable to the interface of two liquids or two vapours in equilibrium with vapor phase and then the drop spreads on the solid surface till the three interfacial forces balance each other. Contact angle (θ) is the angle made by the tangent to the liquid-vapor (gas) interface drawn at the contact line makes an angle with the solid surface, which is the characteristic of the three-phase system (solid-liquid-vapor). The contact angle therefore is a thermodynamic property. The three forces acting on the contact line due to interfacial tension. At equilibrium condition, the net force on the contact line must be zero. This is governed by Young's equation [23].

$$\gamma_{sv} - \gamma_{sl} - \gamma_{lv} \cos\theta = 0 \qquad [2.18]$$

where, $\gamma_{sv}$ , $\gamma_{sl}$ , $\gamma_{lv}$ are solid-vapor (*sv*), solid-liquid (*sl*) and liquid-vapour (*lv*) interfacial energies, respectively and θ is the contact angle. Contact angle is specific for any given material. This concept can be illustrated with a small liquid droplet resting on a flat horizontal solid surface as shown in figure 2.13 (b).

Consider a liquid drop on a solid surface. If the liquid is very strongly attracted to the solid surface (for example water on a strongly hydrophilic solid) the droplet will completely spread out on the solid surface and the contact angle will be close to 0°. Less strongly hydrophilic solids will have a contact angle up to 90°. On many highly hydrophilic surfaces, water droplets will exhibit contact angles of 0° to 30°. If the solid surface is hydrophobic, the contact angle will be larger than 90°. On highly hydrophobic surfaces the surfaces have water contact angles as high as ~120° on low energy materials e.g. fluorinated surfaces. However some materials with highly rough surface may have water contact angle greater

than 150°. These are called superhydrophobic surfaces [24]. The surface wettability is important as electrode/electrolyte interaction plays significant role in supercapacitors, hence affects the supercapacitive performance of the material electrode.

## SECTION (III)

## SUPERCAPACITOR

### 2.C Theoretical background:

### 2.C.1 Introduction:

Supercapacitor, emerged as new technology with the great potential to enable major advances in energy storage and able to fulfil the increasing demand of world powers and scientific community. There has been great interest in developing and refining more efficient energy storage devices. Traditionally, due to the low cost the most commonly used storage devices are electrolytic capacitors and batteries, but they have some drawbacks such as size, performance and life. The supercapacitor has emerged to assists foremost progresses in the energy storage field [25-28]. Supercapacitors make use of high surface area electrode materials and thin electrolytic dielectrics to achieve capacitances several orders of magnitude larger than traditional capacitors [28-30]. In doing so, supercapacitors are able to attain greater energy densities while still maintaining the high power density characteristic of conventional capacitors.

### 2.C.2 Fundamentals of supercapacitor

There are three general classifications of capacitors: electrostatic, electrolytic and electrochemical. Electrostatic capacitors are typically made of two metal electrodes (parallel plates) separated by an insulator called the dielectric as shown in figure 2.14 (a). The dielectric conducts ionically, but not electrically (e.g. air, plastic, paper, Mylar, etc.) that is inserted between the parallel plates of the metal electrode material. The strength of the dielectric material measured in volts per meter ($Vm^{-1}$) determines the operating voltage of the capacitor. The dielectric strength equals the maximum electric field that can exist in a dielectric without

electrical breakdown. By the application of voltage, opposite charges get accumulated on the surfaces of each electrode of capacitor too. The charges are kept separate by the dielectric, resulting as an electric field that permits the capacitor to store energy. The dielectric increases the overall capacitance and the maximum operating voltage of the capacitor. The capacitance, measured in Farads (F), is defined as the ratio of total charge in coulombs (Q) in each electrode to the potential difference (V) between the plates:

$$C=Q/V \qquad [2.19]$$

The capacitance is also proportional to the surface area (A) of the plates and inversely proportional to the distance (d) between the plates:

$$C=(\varepsilon_0\varepsilon_r A)/d \qquad [2.20]$$

The product of $\varepsilon_0$ and $\varepsilon_r$ is a constant of proportionality where '$\varepsilon_0$' is the dielectric constant (i.e. "permittivity") of free space and '$\varepsilon_r$' is the dielectric constant of the insulating material between the electrodes. The two principal characteristics of a capacitor are its energy density and power density. For either measure, the density can be calculated as a quantity per unit mass or per unit volume. The stored energy of the capacitor in the form of electrostatic field is proportional to the capacitance (C) and voltage (V) square across the plates.

$$E= QV= 1/2\ (CV^2) \qquad [2.21]$$

Generally, power P is the energy spent per unit time. In case of capacitor, power determination can be done by considering an external "load" resistance R in series with capacitor, as shown in figure 2.14 (b). Along with this, also internal components (e.g. current collectors, electrodes and dielectric material) of the capacitor also contribute to the

resistance and collectively measured by a quantity called as "equivalent series resistance" (ESR). During discharging, voltage is determined by these resistances. When measured at matched impedance (i.e. at R = ESR), then maximum possible power that can be supplied by a capacitor [25-30] is given by equation:

$$P_{(max)} = V^2/(4.ESR) \qquad [2.22]$$

Above equation explains the major role of the ESR in limiting the maximum power of a capacitor. Traditional capacitors have relatively high power densities, but low energy densities comparatively with electrochemical batteries and to fuel cells. Explicitly, a battery can store up more energy than that of a capacitor, but unable to deliver it very quickly, i.e. low power density. Conversely, capacitors store relatively less energy per unit mass or volume, but can be discharged rapidly to produce a lot of power, so their power density is usually very high.

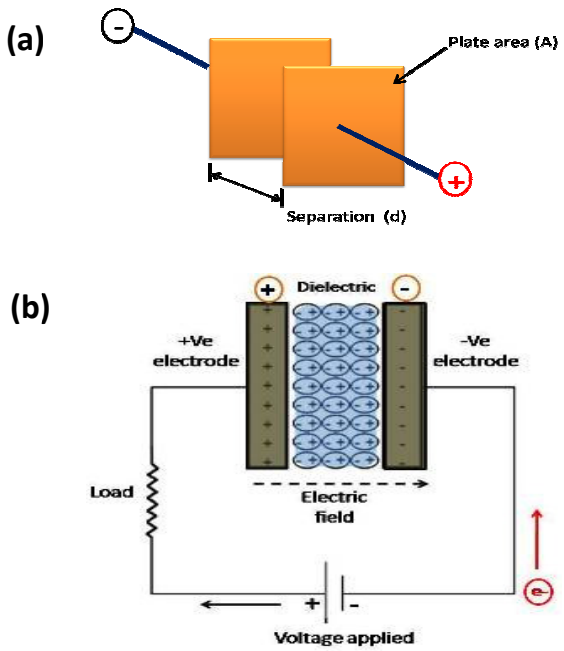


**Fig. 2.14** (a) Simplified parallel-plate capacitor (b) Schematic of a traditional capacitor.

An electrolytic capacitor is similar in construction to an electrostatic capacitor but has a conductive electrolyte salt in direct contact with the metal electrodes. For example, aluminum electrolytic capacitors are made up of two aluminum conducting foils (one coated with an insulating oxide layer) and a paper spacer soaked in electrolyte. The oxide layer serves as the dielectric and is very thin, which results in higher capacitance per unit volume than electrostatic capacitors. Electrolytic capacitors have plus (+) and minus (-) polarity due to the oxide layer, which is held in place by the electric field established during charge. If the polarity is reverse-biased, the oxide layer dissolves in the electrolyte and can become shorted and in extreme cases, the electrolyte can heat up and explode.

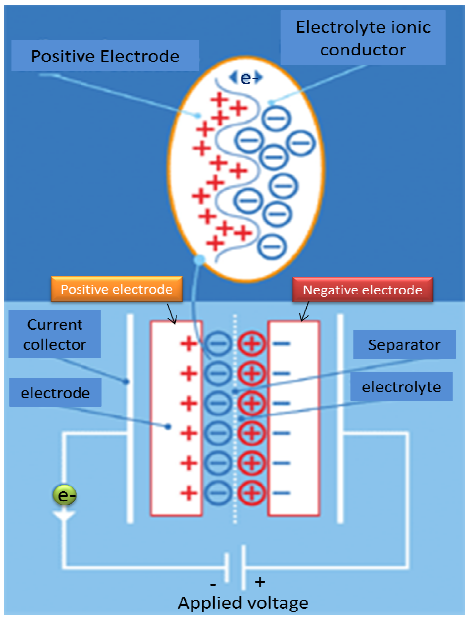


**Fig. 2.15** Schematic representation of an electrochemical double layer capacitor.

In general, electrochemical capacitors (ECs)/supercapacitors (SCs) also use electrolyte solutions but have even greater capacitance per unit volume due to their porous electrode structure compared to electrostatic and electrolytic capacitors. At the macroscopic level, the SC takes the

equation {$C = \varepsilon_0\varepsilon_r A/d$} to the extreme by having a very high electrode surface area (A) due to the porous electrodes and very small separation (d) between the electronic and ionic charge at the electrode surface.

Indeed, the surface area of the porous electrodes has been recorded to be as large as 1000 to 2000 $m^2cm^{-3}$. The high energy density of SCs is due to their greater capacitance per unit volume compared to traditional capacitors. Moreover, SCs are also able to achieve comparable power densities by maintaining the low ESR characteristic of conventional capacitors. Figure 2.15 provides a schematic representation of a supercapacitor, exemplifing some of the physical features described above.

**2. C.3 Classification of supercapacitors :**

Taxonomy of supercapacitors is mainly based on their unique mechanism of storing charge and can be divided into three general classes:

1) Electrochemical double-layer capacitors (non-Faradaic reaction),
2) Pseudo or redox capacitors (Faradaic reaction)
3) Hybrid capacitors (combination of above two)

Figure 2.16 shows taxonomy of supercapacitors. A non-Faradaic mechanism does not use chemical reactions. However, charges are distributed on surfaces by physical processes that do not involve the making or breaking of chemical bonds (i.e. charge stored electrostatically) [31]. In contrast Faradaic processes involve redox reactions such as, oxidation-reduction, for transfer of charge between electrode and electrolyte.

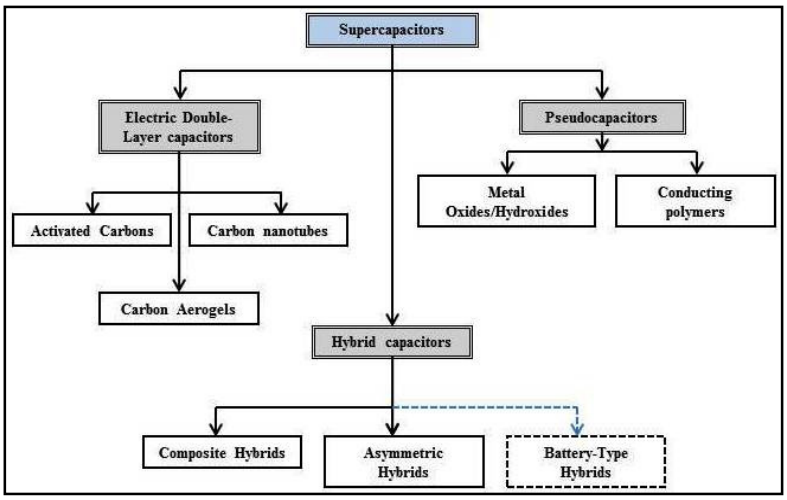


**Fig.2.16** Taxonomy of supercapacitors

## 2. C.3.1 Electrochemical double-layer capacitors

The electric double-layer concept was first described by Hermann von Helmholtz. By assuming that, there is no chemical reaction at the electrode and the interaction between the ions in solution and the electrode surface is purely electrostatic, he concluded that the ions hold electric charge at the electrode surface. When an electric potential is applied to the current collectors, electrons accumulate on the negative electrode thus attracting the positively charged cations to accumulate on the electrode surface to balance the charge locally. Similarly, on the positive electrodes, the electron vacancies attract the negatively charged anions to settle on the electrode surface to balance the charge. This separation of ionic and electronic charge gave rise to the name 'double-layer' capacitors. Double-layer capacitance forms on each electrode in the presence of electric potential. The double-layer capacitance at the positive and negative electrodes adds in series to the total capacitance of the device. The amount of ion accumulation depends on the electric potential. The higher the electric potential, concentration of ions at the surface is

also higher. A simplified cation accumulation on a negatively charged particle in the form of double layer is shown in figure 2.17.

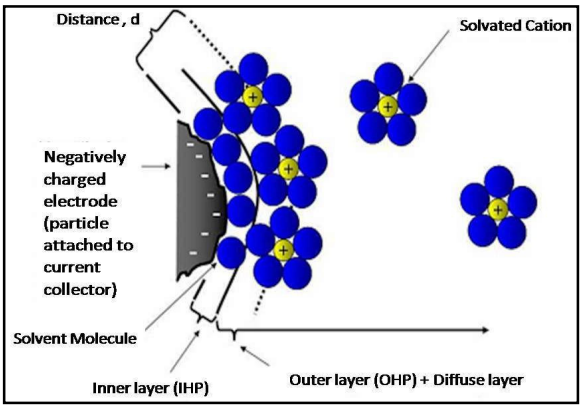


**Figure 2.17** A simplified cation accumulation on a negatively charged particle in the form of double layer.

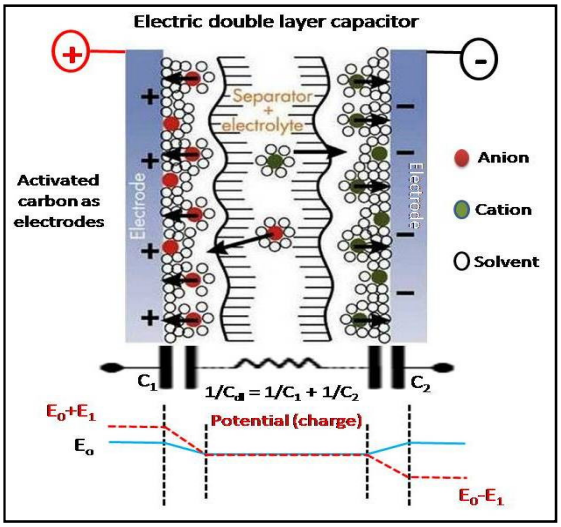


**Figure 2.18** Schematic of EDLC representing resultant capacitance to store charge electrostaticaly and illustration of the potential drop at interface of electrolyte and electrode.

Electrochemical double-layer capacitors (EDLCs) are constructed by using two carbon-based electrodes with high surface area, an electrolyte and a separator. Figure 2.18 represents schematic of electric double layer

capacitor with resultant double layer capacitance ($C_{dl}$) as a series combination of capacitances $C_1$ and $C_2$ originated at both positive and negative electrodes to store energy electrostaticaly. Similar to traditional capacitors, EDLCs store charge electrostaticaly or non-Faradaically, so there is no charge transfer between electrode and electrolyte. EDLCs exploit an electrochemical double-layer of charge for energy storing purpose. Collection of charge onto electrode surfaces is aroused by the application of voltage.

Unlike charges, ions in the electrolyte solution get attracted and diffused across the separator into the pores of the oppositely charge electrode. But the electrodes are modified to avoid the ions recombination. Hence, a double-layer of charge is produced at each electrode. These double-layers, together with an increase in surface area and a decrease in the distance between electrodes, allow EDLCs to achieve higher energy densities than traditional capacitors [32]. Charge storage in EDLCs is highly reversible because, firstly, there is no transfer of charge between electrolyte and electrode. Secondly, there is no any chemical or compositional conversion of electrode material; as process is non-Faradaic. This consent EDLCs capacitors to achieve very high cycling stabilities and provide longer operating life. Therefore, EDLCs work with stable performance characteristics with theoretically uncountable charge-discharge cycles, in practise up to $10^6$ cycles.

On the other hand, electrochemical batteries are generally limited to only up to few thousands cycles. The characteristics performance of an EDLC can be attuned by changing the nature of its electrolyte. An EDLC can make use of either an aqueous or organic (non-aqueous) electrolytes. Cell voltage is also a very important operating parameter that influences energy storage, which is apparent from equations (2.21) and (2.22), in

which both the energy and power of supercapacitors are proportional to the square of the operating voltage. The operating voltage of the cell is dependent on electrolyte stability. Aqueous electrolytes, such as sulfuric acid ($H_2SO_4$) and potassium hydroxide (KOH), offer the advantage of high ionic conductivity, lower ESR value and lower minimum pore size requirements as compared to organic electrolytes but suffer a low breakdown potential of about 1.2 V. However, organic electrolytes such as propylene carbonate and acetonitrile ($CH_3CN$) containing dissolved quaternary ammonium salts; permit operating voltages of near 3 V without breakdown, but their electrical resistance is at least an order of magnitude greater than that of aqueous electrolytes. Providing the applied voltage to the cell does not exceed the electrolyte breakdown potential; no significant chemical reactions will occur, at least in the absence of functional groups on the surface of the electrode material (that are susceptible to reactions at these voltages). Therefore, in choosing between an aqueous or organic electrolyte, one must consider the tradeoffs between capacitance, ESR and voltage. Because of these tradeoffs, the choice of electrolyte often depends on the proposed application of the supercapacitor. Factors that can contribute in varying degrees to the ESR of an electrochemical capacitor include

a. Ionic resistance of the electrolyte in the separator, which is controlled by the thickness and openness of the separator and electrolyte conductivity.

b. Electronic resistance of the electrode materials (very small by design).

c. Resistance of the interface between electrodes and current collectors (a factor now virtually negligible in commercial products, having been eliminated by modern design).

The nature of the electrolyte plays significant role in supercapacitor design; the subclasses of EDLCs are distinguished mainly by the form of carbon they use as an electrode material. Carbon electrode materials receives great interest because, they have generally larger surface area, lower cost and many well established production techniques than other materials, such as conducting polymers and metal oxides [33]. Activated carbons, carbon aerogels, carbon nanotubes, etc are the various forms of carbon materials used to store charge in EDLC electrodes.

Carbon is the most common and economical material for supercapactior electrodes and has been utilised as a high surface area electrode material ever since development of the electrochemical capacitor began. Today, it is still an attractive option because of its low cost, availability and long history of use. Carbon electrodes can take a number of manufactured forms such as foams, fibres and nanotubes.

**a) Activated carbons (ACs)**

Activated carbon (AC) is the most commonly used electrode material in EDLCs due to low cost and possesses a higher surface area than other carbon-based materials. ACs make use of a intricate porous structure composed of various sized micropores (<20 Å wide), mesopores (20-500 Å), and macropores (>500 Å) to achieve their high surface areas. Though capacitance is directly proportional to surface area, not all of the high surface area contributes to the capacitance of the device [36-38]. This contradiction is supposed to be caused by electrolyte ions that are too large to diffuse into smaller micropores, thus preventing some pores from contributing to store charge [35-37]. Also there exists an empirical correlation between distribution of pore sizes, the energy density and the power density of the device. Larger pore sizes correlate with higher power densities and smaller pore sizes correlate with higher energy densities. So,

pore size distribution of AC electrodes is a major area of research in EDLC design [33-37].

**b) Carbon Aerogels**

Carbon aerogels are formed from a continuous monolithic three-dimentional mesoporous network of conductive carbon nanoparticles with interspersed mesopores. Due to this continuous structure and their ability to bond chemically to the current collector, carbon aerogels do not require the application of an additional adhesive binding agent. As a binderless electrode, carbon aerogels have been shown to have a lower ESR than activated carbons [38]. This reduced ESR, yields higher power and is the primary area of interest in supercapacitor research involving carbon aerogels. Carbon aerogel and xerogels are considered as promising materials for supercapacitors, because they have high surface area, low density and good electrical conductivity. In order to improve the capacitance of carbon materials, functional groups are introduced into the carbon materials. Because the functional groups are related to the pseudocapacitance, which is a very effective method of increasing the capacitance.

**c) Carbon Nanotubes**

Nanostructured carbon films have highly accessible surface area needed for supercapacitors due to the structure based on the nanotube embryos and porosity with grain size of a few tens of nanometers. Carbon nanotubes are very attractive both for industrial and academic research due to their unique properties and offer a new possibility for carbon electrodes. Preliminary results suggest that higher capacitance is achieved by tangled networks with an open central canal. Unlike other carbon based electrodes, the mesopores in carbon nanotube electrodes are

interconnected, allowing a continuous charge distribution that uses almost all of the available surface area. Thus, the surface area is utilized more efficiently to achieve capacitances comparable to those in activated-carbon-based supercapacitors, even though carbon nanotube electrodes have a modest surface area compared to activated carbon electrodes [39].

### 2.C.3.2 Pseudocapacitance:

Besides the capacitance contribution from the separation of charge in the double layer, capacitance associated with reactions on the surface of the electrode is also important. During these reactions, electron transfer does take place across the double layer with consequence of change of oxidation state. Thus the capacitance from the faradaic process is referred to as pseudocapacitance.

Pseudocapacitance is faradaic in origin, accomplished through electrosorption, reduction-oxidation reactions and intercalation processes which is quite different from the classical electrostatic capacitance observed in the double layer [5]. In the case of the pseudocapacitance, charge will transfer across the double layer, similar to discharging and charging in a battery. The charge transfer that takes places in these reactions is voltage dependent, so a capacitive phenomenon occurs. Thus the capacitance can be calculated by using the extent of charge stored ($\Delta q$) and the change of the potential ($\Delta V$). The relationship between them can be described by equation,

$$C = \partial(\Delta q) / \partial(\Delta V) \qquad [2.23]$$

Generally in a double layer carbon capacitor, there is about 1-5% pseudocapacitance due to the functional groups on the surface, but there is also about 5-10% double layer capacitance in a battery. Pseudocapacitance can be caused by electrosorption of H or metal atoms

and redox reactions of electroactive species, which strongly rely on the chemical affinity of the surface to ions in the electrolyte. On the one hand, pseudocapacitance can remarkably enhance the capacitance of supercapacitors; while on the other hand, it also deteriorates other properties, such as life cycle. There are two types of reactions that can involve a charge transfer which is voltage dependent.

**A) Redox reactions**

Supercapacitors get their charge from the reduction and oxidation (redox) reaction; redox is the charge transfer of electrons that takes place at the electrode and electrolyte interface due to change in oxidation state. In a redox reaction involving an oxidant (ox) and reductant (red), of the form $ox + ze^- \leftrightarrow red$, the potential, E, is given by the Nernst equation as shown below,

$$E=E^0 + (RT/zF)*\ln (\Re/1-\Re) \qquad [2.24]$$

Where, $E^0$ – is the standard potential, R– is the gas constant, T– is the absolute temperature, F– is the Faraday constant, and $\Re$- is defined as [ox]/([ox]+[red]), (where square brackets denote species concentrations). The amount of charge q (given by the product zF), is therefore a function of the potential E. Differentiation of equation (2.24) thus produces a pseudocapacitive relation.

**B) Adsorption of ions**

The deposition of ions to form a monolayer on the electrode substrate is a reversible process that results in a Faradaic charge transfer and hence gives rise to pseudocapacitance in a similar manner to that demonstrated in redox reactions. Several types of materials with significant pseudocapacitance behavior have been investigated: (1)

electroactive oxide, hydrous oxide, hydroxide films of transition metals, such as Ru, Co, Ni, Mn, Ir, Mo, W, etc; (2) films of conductiving polymers, e.g. polypyrrole, polythiophene, polyaniline and their derivatives.

### a) Transition metal oxides/hydroxides

Metal-oxides/hydroxides present an attractive alternative as an electrode material because of high specific capacitance and low resistance, possibly making it easier to construct high-energy, high-power EDLCs. Extensive research into ruthenium oxides has been conducted, where cost is presumably an issue for commercial ventures. Transition metal oxides/hydroxides ($RuO_2$, $IrO_2$, $Ni(OH)_2$, $Co(OH)_2$, etc) have been explored as a possible electrode material for pseudocapacitors [40, 41]. The capacitance of $RuO_2$ is achieved through the insertion and removal or intercalation of protons into its amorphous structure. While it's hydrous form shows higher capacitance than that of carbon-based and conducting polymer materials [42, 43]. Moreover, hydrous ruthenium oxide has lower ESR than other electrode materials. Therefore, $RuO_2$ is possibly capable of attaining higher energy and power densities than EDLCs and conducting polymer pseudocapacitors. Metal-oxide/hydroxide electrodes can only be used with aqueous electrolytes, thereby limiting the achievable cell voltage. Gains in power density from lower resistance are therefore often offset by losses due to the lower operating voltage.

### b) Conducting polymers

Conducting polymers such as, polyaniline, polypyrrole, polythiophenes, and polyacetylene comprise a large degree of π-orbital conjugations that lead to electronic conductivity and can be oxidized or reduced electrochemically by withdrawal or injection of electrons, respectively. They have a relatively high capacitance and conductivity, in

conjunction with a relatively low ESR and cost than the carbon-based electrode materials. Especially, the n-type or p-type polymer configuration, with one negatively charged (n-doped) and other positively charged (p-doped) conducting polymer electrode, has the greatest potential energy and power densities; but, a lack of efficient, n-doped conducting polymer materials have prevented these pseudocapacitors from achieving their strength [44-48]. Moreover, mechanical stress on conducting polymers during reduction-oxidation reactions also limits their stability through many charge-discharge cycles.

### 2.C.3.3 Hybrid capacitors:

Hybrid electrode configurations show considerable potential, consisting of two different electrodes made of different materials. Composite electrodes consist of one type of material incorporated into another within the same electrode. Carbon nanotubes coated with conducting polymers have yielded particularly good results, with high specific capacitances of 180 $F.g^{-1}$ being reported [49]. The improved levels of energy storage are a result of the charging, taking place largely throughout the bulk of the material, along the surface of the nanotubes and along the backbone of the polymer. The pseudocapacitance arising from the redox processes in the polymer further enhances the capacitive gains. Hybrid capacitors combine the best features of EDLCs and pseudocapacitors together into a unified supercapacitor with better performance characteristics. Both Faradaic and non-Faradaic processes are used to store charge. Hybrid capacitors have achieved superior energy and power densities than EDLCs by sustaining in the cycling stability. Along with the increasing interest in developing high cycle life, high-energy supercapacitors, the tremendous flexibility in tuning the design and performance of hybrid capacitors is leading them to surpass EDLCs as

the most promising class of supercapacitors. Currently, researcher focused on three different types of hybrid capacitors, based on their electrode configuration as follow:

**a) Composite**

Incorporation of carbon-based materials with either metal oxide/hydroxide or conducting polymers results in the formation of a single composite electrode incorporates physical and chemical charge storage mechanisms combinely. The carbon-based materials support to EDLC for charge storage as well offer a high-surface-area backbone that enhances the interaction between electrolyte and deposited pseudocapacitive material. Further this could able to boost the capacitance of the composite electrode through Faradaic (redox) reactions [50-55]. Single wall carbon nanotube (SWNT) and multi-walled carbon nanotubes (MWNT) are the major invention regarding energy storage purpose. The modification of CNTs with conducting polymers is one way to increase the capacitance of the composite resulting from redox contribution of the conducting polymers. In the CNT/conducting polymer composite, CNTs are electron acceptors, while the conducting polymer serves as an electron donor. A charge-transfer complex is formed between CNTs in their ground state and aniline monomer.

**b) Asymmetric**

Asymmetric supercapacitors use two different materials for the positive and negative electrodes. However, they get their charge from the reduction and oxidation (redox) reaction. Redox is nothing but, the charge transfer of electrons occurred at the electrode-electrolyte interface due to change in oxidation state [56]. But, asymmetric hybrids combine non-Faradaic and Faradaic processes by coupling of EDLC electrode with a

pseudocapacitor electrode. Especially, coupling of a -ve AC electrode with a +ve conducting polymer electrode is a crucial topic and pays great attention. The deficiency of -vely charged conducting polymer material has limited in the success of pseudocapacitive conducting polymer. The implementation of a -vely charged, AC electrode attempts to avoid this difficulty. Generally conducting polymer electrodes show higher capacitances plus lower resistances than AC electrodes, but possess lower maximum voltages and less cycling stability. Asymmetric hybrid capacitors which combine these two electrodes possess higher cycling stability than analogous pseudocapacitors as well; improve the extent to attain higher energy and power densities than analogous EDLCs [57, 58].

**c) Battery type**

Similar to asymmetric hybrids, battery-type hybrids couple two different electrodes; however, battery-type hybrids are unique in coupling a supercapacitor electrode with a battery electrode. This specialized configuration reflects the demand for higher energy supercapacitors and higher power batteries, combining the energy characteristics of batteries with the power, cycle life and recharging times of supercapacitors. Research has focused primarily on using nickel hydroxide, lead dioxide and LTO ($Li_4Ti_5O_{12}$) as one electrode and AC as the other [59]. Although, there is less experimental data on battery type hybrids than on other types of supercapacitors, the data that is available suggests that these hybrids may be able to bridge the gap between supercapacitors and batteries. Despite the promising results, the general consensus is that more research will be necessary to determine the full potential of battery-type hybrids [60].

## 2.C.4 Performance characteristics of supercapacitors:

Electrochemical capacitors behave differently to conventional capacitors, which is to be expected based upon the different charge storage mechanisms involved. The performance characteristics of EDLCs will therefore be discussed in reference to the transmission line model of porous electrodes. This model is very useful in explaining the characteristics of EDLCs, while the other basic models are better suited to the simple experimental estimation of key parameters.

The typical impedance characteristic of an EDLC has several implications for cell performance. At low frequencies the reactance, which is mainly due to capacitance, is at a maximum and approaches the behaviour of an electrostatic capacitance. Under such conditions ions have time to penetrate into the depth of the pores and the maximum electrode surface-area is utilised to contribute to double-layer capacitance. Distributed resistance is also at a maximum. As the frequency increases, however, the capacitance begins to decrease and ion penetration begins to become poor with only the electrode surface being available for charging and discharging. The frequency dependence of a supercapacitor's specific capacity therefore affects the relationship between power density and energy density. Since energy density is directly related to specific capacitance and power density is related to the rate of charge delivery, it is apparent from an EDLC's impedance plot that energy density will be limited at higher rates of power delivery. This phenomenon is clearly understood by well known Ragone plots. It is also evident when charging curves at different power levels are considered. An EDLC's frequency response dictates that less charge can be stored at faster rates of charge. In other words, capacitance at higher scan rates decreases.

Cell voltage is largely dependent on the electrolyte breakdown voltage, while ESR depends on electrode and electrolyte conductivity. Choice of electrolyte is therefore influential. Organic electrolytes have a higher breakdown voltage, but have greater resistance. Advantages in having a higher cell voltage are therefore usually countered by the greater resistance. The capacitor using an organic electrolyte has the higher energy density because of its higher cell voltage, but the cell using an aqueous electrolyte has the greater power density as a result of its better conductance.

EDLC efficiency can be related to the phase angle $\phi$, the angle subtended at the origin of the Nyquist plot. Power lost by heat dissipation through the internal resistance is given by $\cos(\phi)$ and the phase angle decreases from 90° to 0° with increasing frequency [61]. It is therefore apparent that power losses increase at high frequencies.

## References:


1 J. Maier, Nat. Mater., 4 (2005) 805.

2 L.J. Fu, H. Liu, C. Li, Y.P. Wu, E. Rahm, R. Holze, H.Q. Wu, Solid State Sci., 8 (2006) 113.

3 B.E. Conway, J. Electrochem. Soc., 138 (1991) 1539.

4 B.E. Conway, V. Briss, J. Wojtowicz, J. Power Sources, 66 (1997) 1.

5 B.E. Conway, "Electrochemical Supercapacitors: Scientific Fundamentals and Technological Applications", Kluwer-Plenum, New York (1999).

6 A.K. Shukla, A.S. Arico, V. Antonucci., Ren. Sustain. Ene. Rev., 5 (2001)137.

7 Y. Wang, W. Yang, C. Chen, D.G. Evans, J. Power Sources, 184 (2008) 682.

8 T.P. Niesen, M.R. De Guire, Solid State Ionics, 151 (2002) 61.

9 C.D. Lokhande, Mater. Chem. Phys., 27 (1991) 1.

10 J. George, "Preparation of Thin Films", Marcel Dekker, Inc., New York. (1992).

11 P.C. Andricacos, Electrochem. Soc. Interface, 8 (1999) 32.

12 W. Schmickler, E. Santos, "Interfacial Electrochemistry", Oxford University Press, New York, Second Edition (2010).

13 K.L. Chopra, "Thin Film Phenomena" Mc Graw Hill Book Co., New York. (1969).

14 B.D. Cullity, "Elements of X-rays Diffraction", Addison-Wesley, London, Second Edition (1978).

15 Y. Ito, M. Abdullah, K. Okuyama, J. Mater. Res., 19 (2004) 1077.

16 M.L. Hair, "Infrared spectroscopy in surface chemistry" (Marcel Dekker, New York, (1967).

17 R.A. Nyquist, R.O. Kagel, "Infrared Spectra of Inorganic Compounds", Academic Press INC, New York. (1971).

18 J. Preudhomme, P. Tarte, Spectrochim. Acta, 27 (1971) 1817.

19 L.D. Hanke, "Handbook of Analytical Methods for Materials, Materials Evaluation and Engineering", Inc. Plymouth (2001).

20 C.R. Brundle, C.A. Evans, J.S. Wilson, "Encyclopedia of materials characterization: surfaces, interfaces, thin films." (1992).

21 O.C. Wells, "Scanning Electron Microscopy", McGraw Hill, Inc. USA (1974).

22 D.D. Macdonald, Electrochim. Acta, 51 (2006) 1376.

23 A.W. Anderson, "Physical Chemistry of Surfaces", John Wiley New York (1982).

24 S. Sarangapani, B.V. Tilak, C.P. Chen, J. Electrochem. Soc., 143 (1996) 3791.

25 C.D. Lokhande, A. Barkschat, H. Tributsch, Sol. Energ. Mat. Sol. C., 79 (2003) 293.

26 A.J. Bard, L.R. Faulkner. "Electrochemical Methods, Fundamentals and Applications" Second Edition. John Wiley & Sons, Inc (2001).

27 A. Burke, J. Power Sources, 91 (2000) 37.

28 R. Kotz, M. Carlen, Electrochim. Acta, 45 (2000) 2483.

29 A.S. Aricò, P. Bruce, Nature Mat., 4 (2005) 366.

30 A. Chu, P. Braatz, J. Power Sources, 112 (2002) 236.

31 M. Winter, R.J. Brodd, Chem. Rev., 104 (2004) 4245.

32 R.A. Dougal, L. Gao, S. Liu, J. Power Sources, 126 (2004) 250.

33 E. Frackowiak, F. Beguin, Carbon, 39 (2001) 937.

34 C. Arbizzani, M. Mastragostino, J. Power Sources, 100 (2001) 164.

35 D.Y. Qu, H. Shi, J. Power Sources, 74 (1998) 99.

36 J. Gamby, P.L. Taberna, J. Power Sources, 101 (2001) 109.

37 H. Shi, Electrochim. Acta, 41 (1996) 1633.

38 C. Lin, J.A. Ritter, Carbon, 35 (1997) 1271.

39 E. Frackowiak, K. Metenier, Appl. Phys. Lett., 77 (2000) 2421.

40 C.H. Hu, Y.H. Huang, J. Electrochem. Soc., 143 (1999) 2465.

41 K.H. Chang, C.C. Hu, J. Electrochem. Soc., 151 (2004) A958.

42 C.C. Hu, C.H. Chu, Mat. Chem. Phy., 65 (2000) 329.

43 J.P. Zheng, P.J. Cygan, J. Electrochem. Soc., 142 (1995) 2699.

44 A.A.F. Grupioni, E. Arashiro, T.A.F. Lassali, Electrochim. Acta, 48 (2002) 407.

45 T. Liu, W.G. Pell, B.E. Conway, Electrochim. Acta, 42(1997) 3541.

46 I.H. Kim, K.B. Kim, Electrochem. Sol. State Lett., 4 (2001) A62.

47 M. Mastragostino, C. Arbizzani, J. Power Sources, 97 (2001) 812.

48 K.S. Ryu, K.M. Kim, J. Power Sources, 103 (2002) 305.

49 W. Chen, T. Wen, H. Teng, Electrochim. Acta, 48 (2003) 641.

50 C.C. Hu, C.C. Wang, Electrochem. Commun., 4 (2002) 554.

51 C.C. Wang, C.C. Hu, Mat. Chem. Phy., 83 (2004) 289.

52 C.C. Hu, W.C. Chen, Electrochim. Acta., 49(2004) 3.

53 C.C. Hu, C.H. Chu, J. Electroanal. Chem., 503 (2001) 105.

54 M. Ramani, B.S. Haran, R.E. White, B.N. Popov, J. Electrochem. Soc., 148 (2001) A374.

55 C.C. Wang, C.C. Hu, Carbon, 43 (2005) 1926.

56 B.E. Conway, Proceedings of the Symposium on Electrochemical Capacitors, 95 (1996) 17.

57 A. Laforgue, P. Simon, J. Electrochem. Soc., 150 (2003) A645.

58 M. Mastragostino, C. Arbizzani, Solid State Ionics, 148 (2002) 493.

59 H.Q. Li, L. Cheng, Electrochem. Solid State lett., 8 (2005) A433.

60 W.G. Pell, B.E. Conway, J. Power Sources, 136 (2004) 334.

61 M. Kaufman, A.H. Seidman, "Handbook of Electronics Calculations for Engineers and Technicians" Second Edition. McGraw-Hill Book Company: (1988).

# CHAPTER III

## Preparation, Characterization and Supercapacitance Evaluation of $Co_{1-x}Ni_x$ LDHs Films Deposited By Potentiodynamic Mode

## CHAPTER III

## SECTION (I)

## PREPARATION AND CHARACTERIZATION OF $Co_{1-x}Ni_x$ LDHs FILMS DEPOSITED BY POTENTIODYNAMIC MODE

### 3.A.1 Introduction:

Supercapacitors have very high specific power and higher charge/discharge rate than the existing secondary batteries. They arouse wide concern by researchers, but their low specific energy restricts them to be used as power sources alone. Nanomaterials are rapidly developing and have been widely used in lots of fields because of their outstanding advantages in science and technology. For example, their properties become deteriorative and even irreversible, under high charge/discharge currents up to 1000 mA $g^{-1}$. Currently, many more materials are potential candidates as electrode materials for supercapacitor function. Such as activated carbon (AC), carbon aerogels, carbon nanotubes as EDLCs electrode; transition metal oxides/hydroxides, conducting polymers as pseudocapacitive (redox) electrodes, etc. Kang et al. recently reported exceed charge/discharge current of the ion-exchange based electrode material [1-4]. Therefore, further breakthroughs in materials are essential. In this regard, the nanostructured LDH materials open up a new important avenue in the advancement of the science and technology. Nanomaterials bring us the advantages of higher electrode/electrolyte contact area, short path lengths for cation transport, high power performance and new reactions, which are not possible with bulk materials [5, 6]. The existing nano-size electrode materials have higher specific mass capacity in the process of charge/discharge than the general micro size electrode material. It has been reported in recent years that some nanostructural electrode materials obtain good charge/discharge capacity [7, 8].

In this chapter, the studies performed on preparation, characterization and supercapacitance evaluation of $Co_{1-x}Ni_x$ LDHs films via potentiodynamic mode (cyclic voltametry) in aqueous media. Cyclic

voltametry provides information regarding electrochemical process which occurred in the solution phase, results new solid phase formation on substrate surface due to redox state. The metal oxides/hydroxides can be deposited easily by this mode wherein, film formation involves the reduction of metal ion on substrate successively followed by oxidation. Optimization of various preparative parameters, such as potential, bath composition and deposition cycles, etc, were carried out to deposit films for supercapacitor application. The redox reaction involving oxidation and reduction of species from electrolyte was studied by cyclic voltammetry (CV) curves. The effect of composition variation of Co and Ni on structural, morphological, wettability and supercapacitive properties of $Co_{1-x}Ni_x$ LDHs thin films has been examined. The effect of electrolyte concentration and scan rate on $Co_{1-x}Ni_x$ LDHs electrodes has been performed. Along with stability and charging–discharging characteristics of $Co_{1-x}Ni_x$ LDHs electrodes are studied.

### 3.A.2 Experimental Setup For $Co_{1-x}Ni_x$ LDHs Thin Film Deposition:

Figures 3.1 and 3.2 show schematic diagram and actual experimental setup for electrodeposition of $Co_{1-x}Ni_x$ LDHs thin films, respectively. Basically, this electrochemical cell is nothing but a conventional three-electrode system assembled in cylindrical glass cell. Purposely cylindrical cell is made up of glass, due to its chemical inertness and visibility inside the bath is possible during deposition. Herein, cell consists of cathode (working electrode-stainless steel), anode (counter electrode-graphite) and reference electrode (SCE). The well cleaned stainless steel substrate is used as working electrode (1 x 4 x 0.05 $cm^3$), polished graphite plate as counter electrode (1.5 x 4 x 0.5$cm^3$) and SCE with saturated KCl solution as a reference electrode are placed in individual slots of backelite holder on cylindrical cell containing

electrolyte. All the depositions were carried out using Potentiostat EG & G 263A model as shown in Fig 3.2.

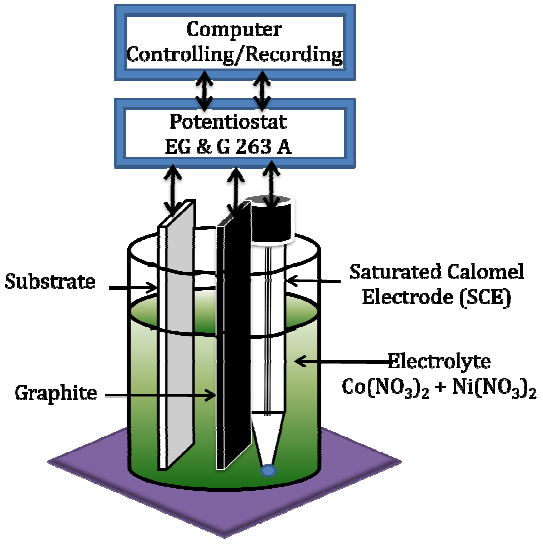


**Fig. 3.1:** Schematic diagram of experimental setup for electrodeposition of $Co_{1-x}Ni_x$ LDHs thin films.

**Fig. 3.2:** Actual experimental setup for deposition of $Co_{1-x}Ni_x$ LDHs thin films along with electrochemical cell.

### 3.A.3 Experimental Details:

Analytical grade chemicals $Co(NO_3)_2 \cdot 6H_2O$, $Ni(NO_3)_2 \cdot 6H_2O$ and research grade stainless steel (SS, grade 304) were used for the deposition of $Co_{1-x}Ni_x$ LDHs thin films. The stainless steel substrate was polished with emery paper to a rough finish, washed with double distilled water and make free of abrasive particles and then air dried.

For the $Co_{1-x}Ni_x$ LDHs thin films deposition, molar concentration of cobalt and nickel nitrate precursors were varied from 0.05 M to 0.2 M. Cyclic voltammetry was performed within the potential range from +500 to -1500 mV/SCE at different scan rate values 5 $mV.s^{-1}$ to 100 $mV.s^{-1}$.

**Table 3.1: Optimized preparative conditions for potentiodynamic deposition of $Co_{1-x}Ni_x$ LDHs thin films.**

| Film | $Co_{1-x}Ni_x$ LDHs | | | | | |
|---|---|---|---|---|---|---|
| Medium | Aqueous | | | | | |
| Bath composition | $Co(NO_3)_2.6H_2O$ :$Ni(NO_3)_2.6H_2O$ | | | | | |
| | 1.0:0.0 | 0.75:0.25 | 0.60:0.40 | 0.50:0.50 | 0.25:0.75 | 0.0:1.0 |
| Total quantity | 30 ml | | | | | |
| pH | ~6 | | | | | |
| Potential range | 0 to -1100 mV/SCE (at 50 $mV.s^{-1}$) | | | | | |
| Temperature | 300 K | | | | | |
| Substrate | Stainless steel | | | | | |

Also the bath temperature was varied from 300 K to 333 K. Out of which, the room temperature (300 K) deposition carried out in 0.1 M nitrate precursor's solution within potential window 0 to -1100 mV/SCE at scan rate 50 $mV.s^{-1}$ results smooth, uniform and good quality thin films with high adhesion. The baths were prepared by varying composition of $Co(NO_3)_2$:$Ni(NO_3)_2$ solution as 1.0:0.0, 0.75:0.25, 0.60:0.40, 0.50:0.50, 0.25:0.75 and 0.0:1.0; for the potentiodynamic deposition of $Co_{1-x}Ni_x$ LDHs onto cost effective stainless steel. The preparative optimized conditions for potentiodynamic deposition of $Co_{1-x}Ni_x$ LDHs thin films is given in table 3.1.

### 3.A.3.1 Cyclic Voltammetry (CV):

Cyclic Voltammetry (CV) is an electrochemical technique which measures the current that develops in an electrochemical cell under conditions where voltage is in excess of that predicted by the Nernst equation. CV is performed by cycling the potential of a working electrode and measuring the resulting current.

A potentiostat is an electronic device which uses a dc power source to produce a potential which can be maintained and accurately determined, while allowing small currents to be drawn into the system without changing the voltage. The current-to-voltage converter measures the resulting current and the data acquisition system produces the resulting voltammogram.

The CV experiment is also applied to study the interfacial behavior of electroactive species which confined to the immediate vicinity of the electrode surface and qualitative information about electrochemical processes under various conditions, such as the presence of intermediates in oxidation-reduction reactions, the reversibility of a reaction.

### 3.A.3.2 Characterization Techniques:

The structural characterization of the $Co_{1-x}$ $Ni_x$ LDHs films were carried out with the help of X-ray diffraction within the range 10°–90° by computer controlled Philips PW-3710 using $CuK_\alpha$ radiations (λ=1.54 Å). The surface morphologies and compositional studies of films were carried out by SEM (scanning electron microscopy, Model: JSM-6701F, JEOL, Japan) attached with an energy-dispersive X-ray spectroscopy (EDS) analyzer to measure the sample composition. The Fourier transform infrared (FT-IR) spectra of the samples were collected using a 'Perkin Elmer, FT-IR Spectrum one' unit. Surface wettabillity study was carried out by Rame-hart USA to understand electrolyte/electrode surface interaction. The 263A EG & G Princeton Applied Research Potentiostat is used for supercapacitor studies by forming electrochemical cell containing $Co_{1-x}$ $Ni_x$ LDH film as a working electrode, platinum (Pt) as a counter electrode and saturated calomel electrode (SCE) as a reference electrode in aqueous KOH electrolyte. Impedance study was carried out using a versastat II frequency response analyzer (FRA) under Z- plot program (Scribner Associates Inc.).

### 3.A.4 Results and Discussion:

### 3.A.4 Electrodeposition of $Co_{1-x}Ni_x$ LDHs Thin Films:

For the deposition of $Co_{1-x}$ $Ni_x$ LDHs films; aqueous bath of 0.1 M solutions of $Co(NO_3)_2$, $Ni(NO_3)_2$ at pH ~6 were used. The suitable composition of $Co_{1-x}$ $Ni_x$ LDHs was achieved from various $Co(NO_3)_2$:$Ni(NO_3)_2$ ratios. The deposition potential and film formation mechanism were studied from voltammograms. The structural, morphological, wettability properties of $Co_{1-x}$ $Ni_x$ LDHs thin films were studied.

### 3.A.4.1 Deposition Potential and $Co_{1-x}Ni_x$ LDHs Film Formation:

The formal deposition potential, redox reactions and film formation were studied from cyclic voltammogram. Figure (3.3) shows voltammograms recorded for 0.1 M solutions of $Ni(NO_3)_2$, $Co(NO_3)_2$ and $Co(NO_3)_2$ + $Ni(NO_3)_2$ at bath compositions 0.0:1.0, 1.0:0.0 and 0.5:0.5 on stainless steel substrate, respectively.

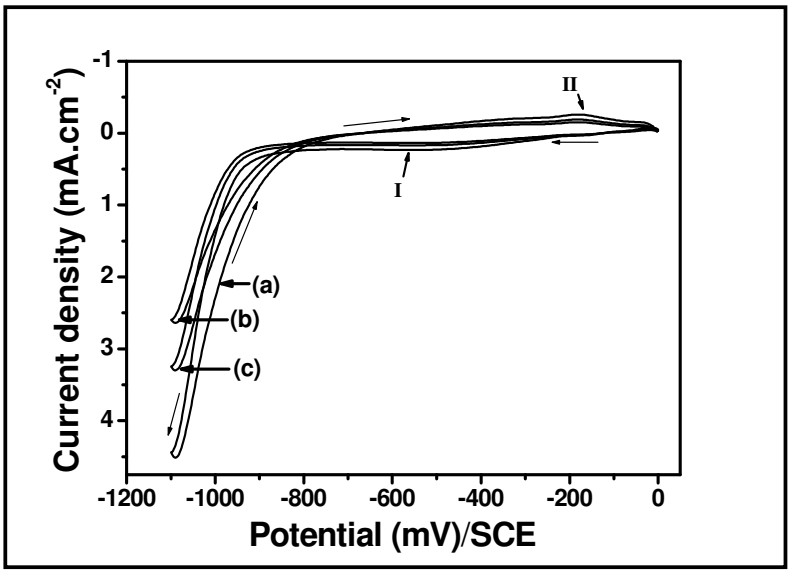


**Figure 3.3:** Cyclic voltamogramms for 0.1 M solution of (a) $Ni(NO_3)_2$, (b) $Co(NO_3)_2$ and (c) $Co(NO_3)_2$+$Ni(NO_3)_2$ with bath composition 0.0:1.0, 1.0:0.0 and 0.5:0.5 onto stainless steel substrate at 50 $mV.s^{-1}$ scan rate, respectively.

The potential was scanned from 0.0 to -1100 mV/SCE at a scan rate of 50 $mV.s^{-1}$. On the forward scan, almost no current was observed until the potential reached -300 mV/SCE. Thereafter, the cathodic current increased gradually with small reduction peak (I) near -500 mV/SCE and after -800 mV/SCE current increased rapidly; herein stages of the nucleation process occurred. The current density was quite higher on the reverse scan until the response reached to -800 mV/SCE. The voltammogram presents metal reduction reaction, particularly the "nucleation loop" towards the negative limit and the dissolution

(oxidation) peak (II) on reverse scan at the potential close to -200 mV/SCE. If lower limit was extended, the cathodic current continued rising at -1200 mV/SCE from which a peeling tendency was observed. From figure it is observed that, Ni solution has significantly higher limiting current and more positive deposition potential than that of Co and Co+Ni. Since, the standard deposition potentials of nickel ($E^0$= -505 mV/SCE) and cobalt ($E^0$= -525 mV/SCE) are very similar so deposition takes place from uncomplexed ions [9].

The possible redox reactions are given below. During electrodeposition from aqueous solution of $Co(NO_3)_2$:$Ni(NO_3)_2$ at negative potentials, nitrate ions can be reduced ($E^0$= -200 mV/SCE) on the cathodic surface to produce hydroxide ions. The generation of $OH^-$ at the cathode raises the local pH, as follow [10],

$$NO^-_3 + 6H_2O + 8e^- \Rightarrow NH_3 + 9OH^- \quad (3.1)$$

Or at higher negative potential value ($E^0$~ -1200 mV/SCE), there may be possibility of occasion of parallel reaction of water electrolysis as given below,

$$2H_2O + 2e^- \Rightarrow H_{2(g)} + 2OH^-_{(aq)} \quad (3.2)$$

But reaction (3.1) is more probable and prime. This reaction can be related to formation of cobalt-nickel hydroxides via reduction ($E^0$~ -500 mV/SCE) as follow.

$$M^{2+}_{(aq)} + 2OH^-_{(aq)} \Rightarrow M(OH)_{2\ (s)} \text{ where M= Co, Ni or (Co+Ni)} \quad (3.3)$$

Therefore, summarising reaction (3.1) and (3.3) are related to the formation of Co-$Ni(OH)_2$. From voltammograms, the metal (Co-Ni) reduction initiates at ~ -500 mV/SCE. In this potential region, it may be possible to get metal (Co, Ni) monolayers accordingly with the characteristics of the deposits obtained within the underpotential

condition [11]. At -1100 mV/SCE (overpotential zone), where "occurs" a tridimensional nucleation and growth of Co, Ni deposition. Under these potential conditions the Co, Ni deposits are massive and random on the electrode [12]. After reversing the potential at -1100 mV/SCE, the metal reduction proceeds up to -500 mV/SCE. The crossover between cathodic current branches is observed during the scan toward positive potential. The cathodic crossover -800 mV/SCE) corresponds to the nucleation overpotential from which the parameters of the nucleation-growth mechanism are taken [13]. At potentials more negative than -800 mV/SCE, the current for the scan toward positive potential is lower than that before the inversion of potential (-1100 mV/SCE), probably due to the corresponding change in the concentration of metal and hydroxyl ions at the electrode surface, due to the deposition process. On the other hand, in the range between -1000 mV/SCE and -800 mV/SCE, the current toward positive potential scan was higher than before the inversion of potential [13].

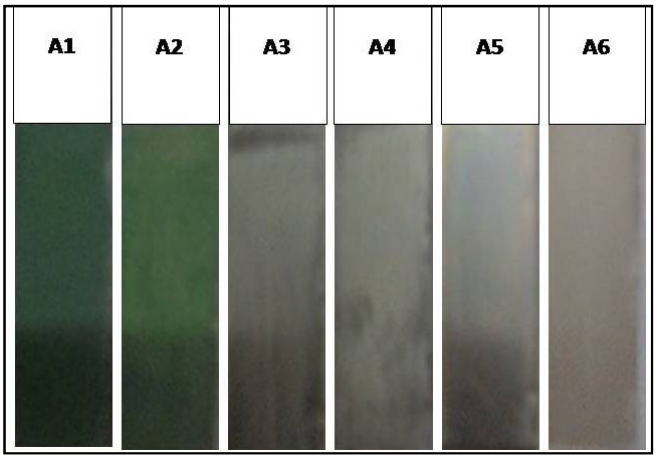


**Figure 3.4:** Photograph of $Co_{1-x}$ $Ni_x$ LDHs thin films with $Co(NO_3)_2$:$Ni(NO_3)_2$ bath compositions A1 (1.0:0.0), A2 (0.75:0.25), A3 (0.6:0.4), A4 (0.5:0.5), A5 (0.25:0.75), A6 (0.0:1.0).

At more anodic potentials the Co-Ni dissolution process initiates at -600 mV/SCE which is characterized by an anodic current peak and a mass decrease on the electrode. The current peak (II) was observed at -200

mV/SCE in Fig. (3.3). According to Soto et al., process at anodic peak could be related either to the dissolution of Co-Ni from electrode into the solution in form of different ionic species or to their dissolution in different phases that were previously formed during the cathodic sweep [13].

Well adherent greenish gray coloured uniform $Co_{1-x}$ $Ni_x$ LDHs thin films were obtained by potentiodynamic method. The photograph of various compositions of $Co_{1-x}$ $Ni_x$ LDHs thin films is shown in Fig. 3.4. The estimation of formal deposition potential -900 mV/SCE and deposition current density of 2 $mA.cm^{-2}$ was carried out with the help of cyclic voltammogram for synthesis of $Co_{1-x}$ $Ni_x$ LDHs films onto stainless steel electrode.

### 3.A.4.2 Thickness Measurement:

Figure 3.5 showed variation of deposited weight of $Co_{1-x}$ $Ni_x$ LDHs for different bath compositions of $Co(NO_3)_2$:$Ni(NO_3)_2$ solution.

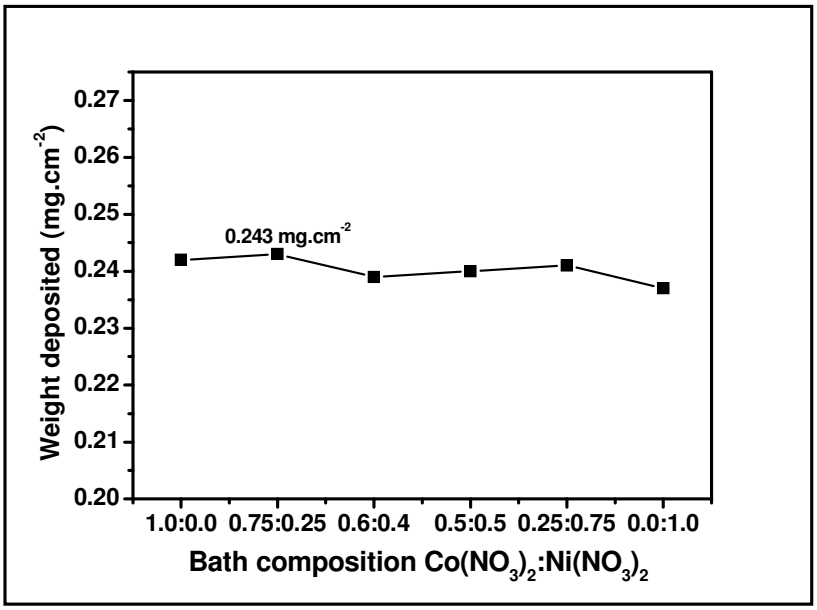


**Figure 3.5:** $Co_{1-x}$ $Ni_x$ LDHs thin film thickness for various bath compositions of $Co(NO_3)_2$:Ni $(NO_3)_2$.

The film thickness in terms of weight deposited of $Co_{1-x}Ni_x$ LDHs is carried out at optimized parameters with scan rate of 50 $mVs^{-1}$ for 50 cycles at room temperature.

The thickness varied accordingly bath composition of cobalt and nickel nitrate solutions (from 1.0:0.0 to 0.0:1.0) within range of 0.237 to 0.243 $mg.cm^{-2}$. The maximum thickness of $Co_{1-x}Ni_x$ LDHs film was obtained for 0.75:0.25 composition.

### 3.A.4.3 Structural Characterization:

Film crystallinity was analyzed using X-ray diffraction. The XRD patterns of $Co_{1-x}Ni_x$ LDHs films onto stainless steel substrate are shown in Fig 3.6. The diffraction peaks in the 2θ range 10°-90° correspond to the characteristic reflections of LDHs materials, with a series of (00l) peaks appearing as narrow symmetric lines at low angle, arising from the basal reflection. The patterns in Fig. 3.6 comprise six peaks, wherein, A1 and A6 are pure $Co(OH)_2$ and $Ni(OH)_2$, respectively. It is noticed that, the relatively higher and sharper diffraction peaks have occurred, which are directly linked to good crystallinity of the deposited films of $Co_{1-x}Ni_x$ LDHs. Out of them, the strong diffraction peaks at 2θ values 50.73° and 74.65° are associated with the stainless steel substrate and are indexed with the star. In particular, the peaks appearing at 2θ values of 12.21° (7.4 Å), 34° (2.65 Å), 43.59° (2.07Å), 60° (1.55 Å) are due to the reflections of the planes (001), (100), (101) and (110), respectively; which corresponds to both α-$Co(OH)_2$ and α-$Ni(OH)_2$ formation in accordance with JCPDS card no. 74-1057 and 38-0715, respectively [14]. It was difficult to differentiate between the two phases, since they have similar structures and their diffraction peaks are very close [6, 15].

The-β-$Co(OH)_2$ and β-$Ni(OH)_2$ has a d-spacing about 4.6 Å, consistent with a close packing of hydroxide layers, while the d-spacing of α-$Co(OH)_2$, α-$Ni(OH)_2$ and the LDHs samples is greater than 7 Å [16-18].

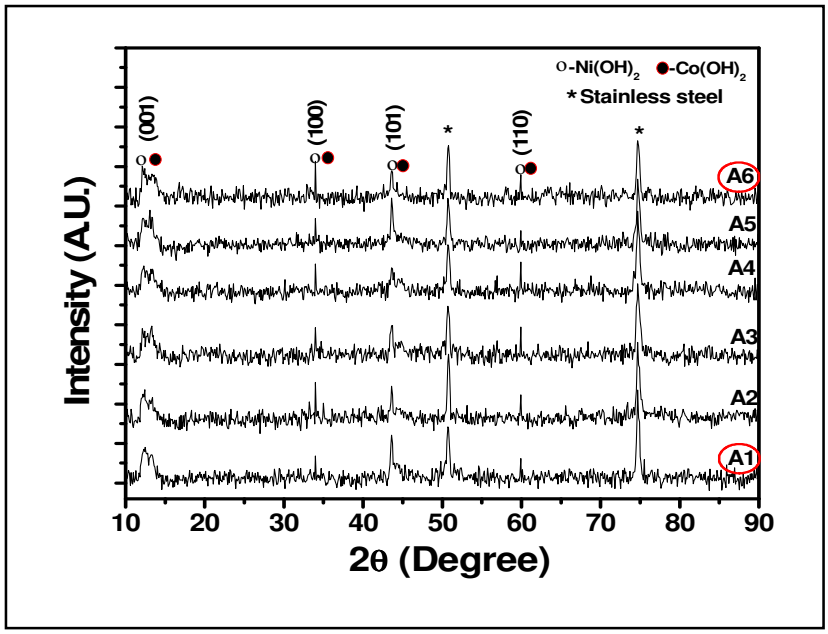


**Figure 3.6:** X-ray diffractograms of $Co_{1-x}$ $Ni_x$ LDHs thin films for various bath compositions of $Co(NO_3)_2$:$Ni(NO_3)_2$ on stainless steel substrate.

### 3.A.4.4 FT-IR study:

Figure 3.7 shows the FT-IR absorption spectra of $Co_{1-x}$ $Ni_x$ LDHs thin films in the range 4000–400 $cm^{-1}$ in further support to XRD study. In the spectra A1 (1.0:0.0), A4 (0.5:0.5) and A6 (0.0:1.0); peak around 3630 $cm^{-1}$ is a characteristic of non-hydrogen bond O-H stretching vibrations of deposited hydroxides. A broad OH band centered at around 3440 $cm^{-1}$ is indicative of O-H stretching vibration of interlayer water molecules within the film structure [19, 20]. The band at 1632 $cm^{-1}$ corresponds to angular deformation of molecular water. Peak around 1380 $cm^{-1}$ is due to the stretching vibrations and characteristics of interlayer $NO_3^-$ anions [21]. The band at 499 $cm^{-1}$ can be attributed to δ(OH) vibration [22, 23]. While the individual occurrence of bands at 467 and 436 $cm^{-1}$ correspond to stretching vibration of Ni-O and Co-O in A6 and A1, respectively are also observed in A4 sample spectrum [24, 25]. Therefore, obtained FT-IR spectra are also supportive to the formation of cobalt and nickel hydroxide phases in potentiodynamic deposit.

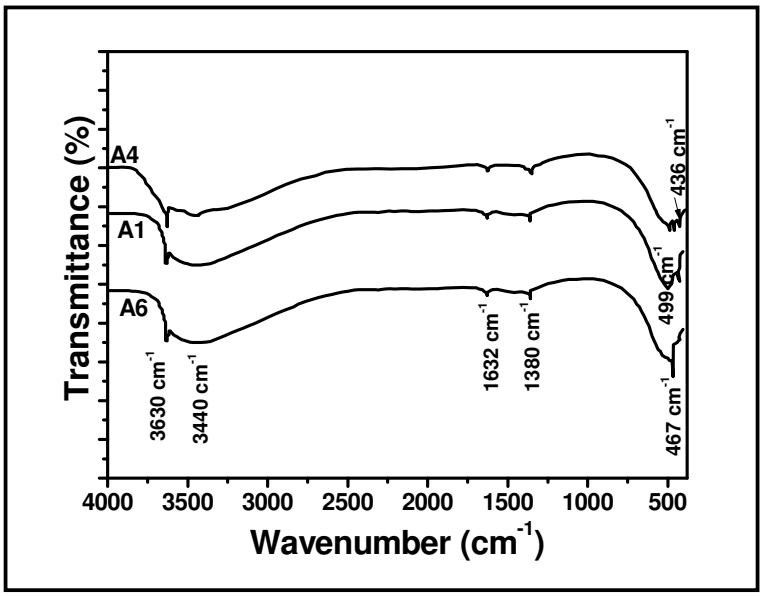


**Figure 3.7:** FT-IR spectra of $Co_{1-x}$ $Ni_x$ LDHs for A1 (1.0:0.0), A4 (0.5:0.5) and A6 (0.0:1.0) bath compositions of $Co(NO_3)_2$:$Ni(NO_3)_2$.

### 3.A.4.5 Surface Morphological (SEM) and Compositional Studies (EDS):

The surface morphologies of the $Co_{1-x}$ $Ni_x$ LDHs thin films were investigated by scanning electron microscopy (SEM) and the micrographs of various compositions at ×50,000 magnifications are shown in Fig. 3.8 (A1-A6). From the SEM images it is clearly seen that, the gradual increase of Ni proportion in the $Co_{1-x}Ni_x$ LDHs deposit has major influence in the emerging form of morphology. The $Co_{1-x}Ni_x$ LDHs thin films were covered with randomly oriented nano-flakes. The morphology of sample A1 (only cobalt hydroxide) is observed to be more porous having thin microstructure seized with thicker nano sheets of width about 23 nm emerges with larger flake size. As nickel contribution within $Co_{1-x}$ $Ni_x$ LDHs augmented, the morphology is observed as shown of sample A2.

The porosity of sample decreases fairly and become quite compact than A1 along with somewhat decrease in size and of sheet width flake

about 20 nm. The change observed in between sample A1 and A2 is relatively small.

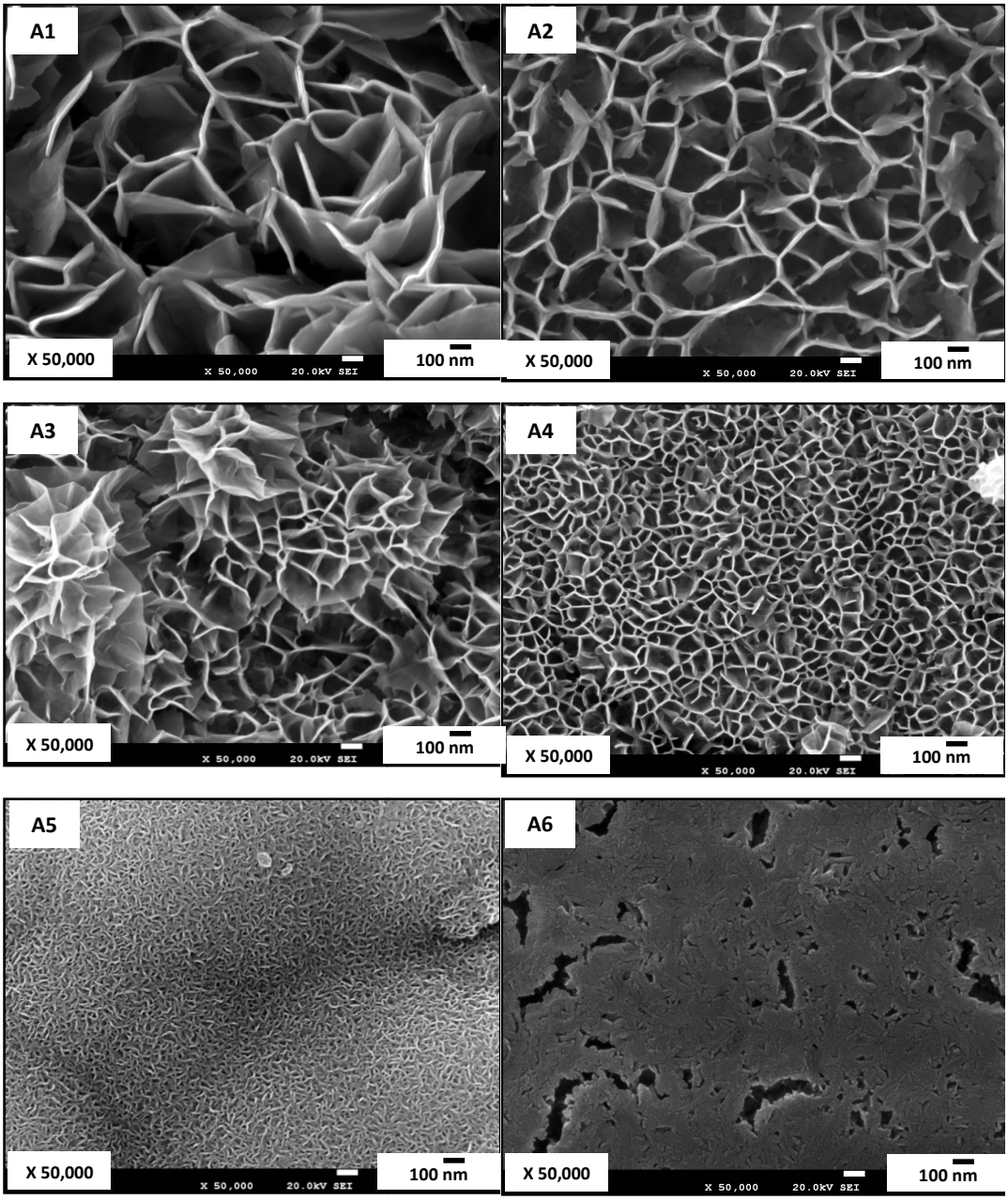


**Figure 3.8:** SEM micrographs of $Co_{1-x}$ $Ni_x$ LDHs thin film for samples A1 (1.0:0.0), A2 (0.75:0.25), A3 (0.6:0.4), A4 (0.5:0.5), A5 (0.25:0.75) and A6 (0.0:1.0) at X 50,000 magnification**.**

But as Ni content in $Co_{1-x}Ni_x$ LDHs goes on increased, the growing morphology became more compact owing less porous microstructure and emerging with bunch of flakes having dense nature.

The grown bunched nano-flakes have small flake size with very thinner flake width as shown in Fig. 3.8. (A3-A6). For sample A6 (only nickel hydroxide) dense microstructure of flakes bunched together was observed. The decrease in width of nano-flakes for samples A1 to A4 was observed from ~ 23 nm to ~14 nm. From the SEM studies we observed that, as Ni proportion in $Co_{1-x}$ $Ni_x$ LDH was increased, the growing morphology become more compact, less porous comprising decrease in flake size along with shrinking flake width. The raised Ni amount may forced to grow flakes collectively in bunches resulting in dense microstructure with decrease in the individual size of flakes and flake width. Thus the results signified that, the Ni content in $Co_{1-x}$ $Ni_x$ LDHs mutates the surface morphological properties of $Co_{1-x}$ $Ni_x$ LDH electrode [6].

All morphologies of $Co_{1-x}$ $Ni_x$ LDHs are important and useful due to the microstructure necessitated accordingly application purposes. Highly porous microstructure is a potential candidate for supercapacitor application provides large surface area; it possesses loosely packed structure and advantageous for the electrolyte ions to access the active materials, results in Faradaic reaction, which may contribute to enhancement of capacitive performance.

Table 3.2 shows the atomic percentages (at%) of the elements Co and Ni in $Co_{1-x}Ni_x$ LDHs, obtained by means of energy-dispersive X-ray spectroscopy (EDS). The elemental composition indicates that the $Co_{1-x}Ni_x$ LDHs are composed of $Co(OH)_2$ and $Ni(OH)_2$. From the EDS data, it is observed that the amount of oxygen (not shown in table) was slightly higher than the Co and Ni combined. The slightly higher content of oxygen may be due to water of hydration as well as absorbed water [6]. From EDS

analysis, the formula of $Co_{1-x}Ni_x$ LDHs would be $[Co(OH)_2]_{1-x}[Ni(OH)_2]_x$ with x= 0, 0.34, 0.46, 0.59, 0.76 and 1, obtained from the deposition carried out in $Co(NO_3)_2$:$Ni(NO_3)_2$ solutions with composition 1.0:0.0, 0.75:0.25, 0.60:0.40, 0.50:0.50, 0.25:0.75 and 0.0:1.0 for samples A1 to A6, respectively.

**Table 3.2: EDS analysis of Co, Ni in potentiodynamically deposited $Co_{1-x}Ni_x$ LDHs, for various compositions of $Co(NO_3)_2$ and $Ni(NO_3)_2$.**

| Sample | Co:Ni | Co (at%) | Ni (at%) | (x) in $[Co(OH)_2]_{1-x}[Ni(OH)_2]_x$ |
|---|---|---|---|---|
| A2 | 0.75:0.25 | 15.7 | 8.3 | 0.34 |
| A3 | 0.60:0.40 | 15.4 | 12.9 | 0.46 |
| A4 | 0.50:0.50 | 10.1 | 13.5 | 0.59 |
| A5 | 0.25:0.75 | 8.6 | 28.4 | 0.76 |

### 3.A.4.6 Surface Wettability Study:

Figure 3.9 shows the photographs of water contact with the $Co_{1-x}Ni_x$ LDHs thin films. From Fig. 3.9 (a) it is clearly seen that, water laid completely flat, get spread and somewhat absorbed by $Co_{1-x}Ni_x$ LDHs film surface for samples A1 (1.0:0.0) to A4 (0.50:0.50). This is in good agreement with the porous or open microstructure. The samples A1-A4 showed superhydrophilic nature with water contact angle <5° by complete wetting of $Co_{1-x}Ni_x$ LDHs surface [26]. Further for Ni rich samples A5 (0.25:0.75) and A6 (0.0:1.0) more flat but resting water drop was observed owing water contact angle of 10° and 13°, respectively as shown in Fig. 3.9 (b, c). This specific property is attributed to somewhat compact and nanocrystalline nature of the $Co_{1-x}Ni_x$ LDHs sample. Overall surface wettability study resulted into superhydrophilic nature of $Co_{1-x}Ni_x$ LDHs deposit, which is likely to acquire very high surface energy and increases with decrease in particle size. Superhydrophilic nature of the $Co_{1-x}Ni_x$ LDHs can be also attributed to the hydrous nature of the films. Hydrous bonding

on the substrate surface also causes the superhydrophilic nature. Therefore, we observed that increase in Ni content in $Co_{1-x}Ni_x$ LDHs can lead to slight increase in contact angle values. Superhydrophilic nature of the $Co_{1-x}Ni_x$ LDHs films is suitable for supercapacitive application wherein access of aqueous electrolyte ions to electrode surface is more and easy [27].

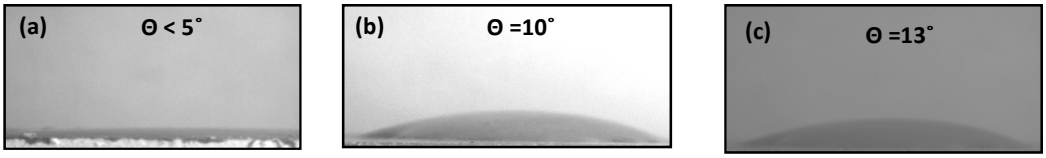


**Figure 3.9:** Measurement of water contact angle of $Co_{1-x}Ni_x$ LDHs samples (a) A1 (1.0:0.0), A2 (0.75:0.25), A3 (0.60:0.40), A4 (0.50:0.50), (b) A5 (0.25:0.75) and (c) A6 (0.0:1.0).

## SECTION (II)

## SUPERCAPACITIVE PERFORMANCE OF POTENTIODYNAMICALLY DEPOSITED $Co_{1-x}Ni_x$ LDHs THIN FILMS

### 3.B.1 Introduction:

The redox capacitors show higher capacitance than EDLCs due to redox reactions involving exchange of protons, with less emphasis on surface area results in higher utilization of electrode material. The conducting polymers and metal oxides/hydroxides come under this category [28, 29]. Therefore, metal oxides of Co, Ni, Fe, Mn, Sn, V, Mo, etc have long been considered as the most promising materials for supercapacitors [30]. Initially noble metal oxides, such as $RuO_2$ have exhibited prominent properties among various pseudocapacitive materials. Hu et al reported that the specific capacitance of $RuO_2$ was even as high as 1500 $F.g^{-1}$ in $RuO_2$/AC composite electrode [31]. However, the high cost of Ru has retarded its commercial acceptance as electrode material in electrochemical capacitors. This limitation has encouraged finding other cheaper materials with similar capacitive behaviour to $RuO_2$ [32]. Therefore, extensive attempts have been taken to make out substitute and economical electrode materials with suitable electrochemical properties. Late development of metal hydroxides with high specific capacitances has regenerated great interest in such materials [33, 34]. Metal hydroxides are often layered materials with large interlayer spacing. They can have very high theoretical specific capacitances. Especially, cobalt and nickel hydroxides have very high potential specific capacitances due to their redox reaction character and layered structures with large interlayer spacing [35]. A recent synthesis of $Co_xNi_{1-x}$ LDHs by the potentiostatic deposition route showed a maximum specific capacitance of 2104 $F.g^{-1}$ [6].

### 3.B.2 Experimental Details and Supercapacitance Evaluation:

In this current effort, $Co_{1-x}Ni_x$ LDHs thin films have been potentiodynamically deposited and used as supercapacitor electrodes. Effect of electrolyte concentration and scan rate on supercapacitance of $Co_{1-x}Ni_x$ LDHs electrodes have been examined along with stability, charging–discharging and impedance characteristics.

In order to study the supercapacitive performance of $Co_{1-x}Ni_x$ LDHs electrode the cyclic voltammetry (CV) experiments were carried out in aqueous KOH electrolyte. The performance of electrodes was studied with respect to various parameters such as, electrolyte concentration, scan rates, specific capacitance, stability, EIS and efficiency.

The preparation of electrode and electrolyte is important in the supercapacitor study. In order to construct the electrode for the supercapacitor study, the 1 $cm^2$ area of the film was used and the remaining part of the film coated with the insulating tape.

#### 3.B.2.1 Experimental Set Up for Supercapacitor Study:

Figure. 3.10 (a) shows the schematic of experimental set up and (b) shows the actual experimental set up for the supercapacitor study. The electrochemical measurements for supercapacitor were carried out in a three electrode electrochemical cell, in which the $Co_{1-x}Ni_x$ LDHs thin film electrode was used as the working electrode, platinum as the counter and saturated calomel electrode (SCE) as the reference electrode.

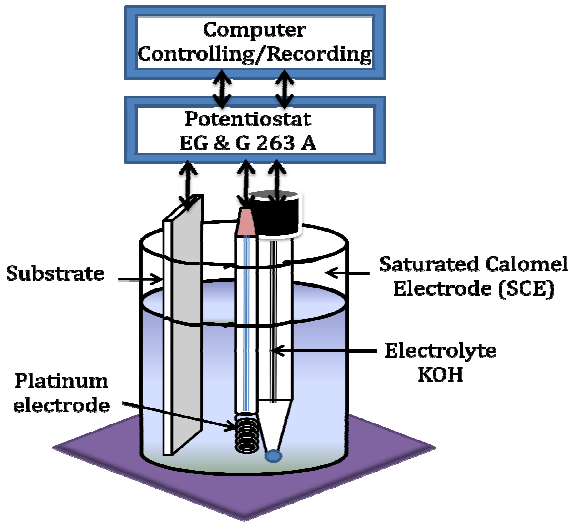


**Fig. 3.10 (a)** Schematic of experimental set up for the supercapacitor study.

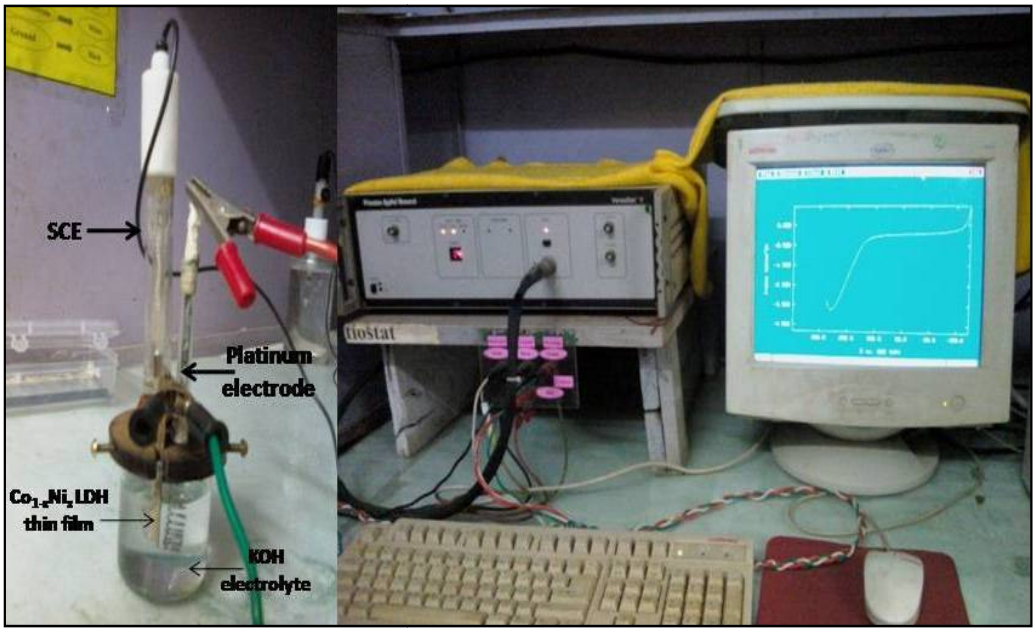


**Fig. 3.10 (b)** Experimental set up for the supercapacitive study.

The specific capacitance values of the $Co_{1-x}$ $Ni_x$ LDHs electrodes in KOH electrolyte were carried out using cyclic voltammetry (CV) experiments. The capacitance value 'C' of electrode was computed by using the relation

$$C = I/(dv/dt) \quad (3.4)$$

Where, 'I' is the average current in amperes and (dV/dt) is the sweep rate in $mV.s^{-1}$. Estimation of interfacial capacitance value ($C_i$) is attained by dividing dipped electrode area (A) in the electrolyte to respective capacitance 'C'.

$$C_i = C/A \quad (3.5)$$

Where, 'A' is the area of electrode dipped in the electrolyte (herein 1 $cm^2$). Determination of specific capacitance value ($C_s$) of the electrode is obtained by dividing the capacitance by the deposited weight of $Co_{1-x}Ni_x$ LDHs electrode dipped in the electrolyte to respective capacitance 'C'.

$$C_s = C/w \quad (3.6)$$

Where, 'w' is the deposited weight of the $Co_{1-x}Ni_x$ LDHs electrode dipped in the electrolyte. By analysis of charging-discharging curves various parameters such as average capacitance, coulomb efficiency, specific energy density and power density of the electrode are calculated.

The average capacitance of the electrode is calculated by relation [36],

$$C = I \times \left(\Delta t/\Delta V\right) \quad (3.7)$$

where, I (Amp) is the constant current, Δt (second) is discharge time period and ΔV (Volt) is the potential window. The capacitor energy efficiency known as coulomb efficiency was calculated by the ratio of the discharge and charge time given as

$$\text{Coulomb efficiency (\%)}\ (\eta) = \left(t_D/t_C\right) \times 100 \quad (3.8)$$

where, $t_C$ is charging and $t_D$ is discharging time periods.

Specific energy density and specific power density are the crucial parameters of energy devices were calculated by following equations [37].

$$\text{Specific energy } (SE) = Q \times \left(\Delta V / w\right) = (I \times t \times \Delta V) / w \qquad (3.9)$$

$$\text{Specific power } (SP) = SE / t = (I \times \Delta V) / w \qquad (3.10)$$

where, w is the mass (Kg) of electrode material.

### 3.B.3 Results and Discussion:

#### 3.B.3.1 Effect of different Electrolytes:

The characteristics performance of an electrochemical capacitor can be attuned by changing the nature of its electrolyte. The electrolytes used in the pseudocapacitors should have a wide range of potentials of electrochemical stability. The resistance of the supercapacitor cell is strongly dependent on the resistivity of the electrolyte used and size of the ions from the electrolyte that diffuse in to and out of the pores of the microporous electrode particles. Organic electrolytes have a higher resistance, but the subsequent power reduction is usually offset by the gain in higher cell voltage. Aqueous electrolytes, such as sulfuric acid ($H_2SO_4$) and potassium hydroxide (KOH), offer the advantage of high ionic conductivity, lower ESR value and lower minimum pore size requirements as compared to organic electrolytes with the resistivity of 1-2 Ω.cm. But, suffer a low breakdown potential of about 1.2 V thereby limiting the maximum achievable power [38]. Furthermore, the acidic electrolytes have the problem of corrosion of electrode due to the acidic nature.

For $Co_{1-x}Ni_x$ LDHs electrode, the aqueous electrolytes like NaOH, KOH, KCl, $Na_2SO_3$, $Na_2SO_4$, $H_2SO_4$, etc have been tested and KOH electrolytes was chosen to achieve maximum capacitance. Many

researchers tested and reported that, the KOH electrolyte is only more suitable for $Co_{1-x}Ni_x$ LDHs electrode [6].

### 3.B.3.2 Supercapacitance of $Co_{1-x}Ni_x$ LDHs films:

Typical cyclic voltammograms of potentiodyanamically deposited $Co_{1-x}Ni_x$ LDHs electrode for different x (Ni) values (x= 0.0 to 1.0) in aqueous 1M KOH electrolyte at sweep rate of 50 $mV.s^{-1}$ within optimized potential range of -200 to +500 mV/SCE is shown in Fig. 3.11. All the curves exhibit two prominent peaks characteristic which indicate capacitive behaviour. An ideal capacitor displays a rectangular shape with no resistance, but the prominent peaks that occur within voltage ranges are usually evidence of pseudocapacitive behaviour [39]. The $Co(OH)_2$, $Ni(OH)_2$ and $Co_{1-x}Ni_x$ LDH electrodes showed very strong redox peaks due to the following Faradaic reactions of $Co(OH)_2$ and $Ni(OH)_2$ as follows[34],

$$Co(OH)_2 + OH^- \Leftrightarrow CoOOH + H_2O + e^- \quad (3.11)$$

$$CoOOH + OH^- \Leftrightarrow CoO_2 + H_2O + e^- \quad (3.12)$$

$$Ni(OH)_2 + OH^- \Leftrightarrow NiOOH + H_2O + e^- \quad (3.13)$$

The CV curves showed shifts in the redox peaks as the composition of the $Co_{1-x}Ni_x$ LDHs were changed, as shown in Fig. 3.11. It is observed that, with increase in Ni content in $Co_{1-x}Ni_x$ LDHs, the oxidation and reduction peaks get shifted towards more positive voltage values within the applied potential window as shown in table 3.3.

It can be seen that, the oxidation and reduction peaks for the $Co_{0.66}Ni_{0.34}$ LDH are at +208 mV/SCE and +28 mV/SCE, respectively, whereas for the $Co_{0.24}Ni_{0.76}$ LDH, the peaks are at +411 mV/SCE and +203 mV/SCE for the oxidation and reduction processes, respectively. The quasi-reversible electron transfer process is observable in all CV curves, indicating that the measured capacitance is mainly based on redox

mechanism [40]. The integral area and redox current is maximal for the $Co_{0.66}Ni_{0.34}$ LDH. So the $Co_{0.66}Ni_{0.34}$ LDH has an optimal characteristic of specific capacitance.

**Table 3.3 Oxidation and reduction peaks in $Co_{1-x}Ni_x$ LDHs.**

| $Co_{1-x}Ni_x$ LDH | Oxidation peak (mV/SCE) | Reduction peak (mV/SCE) |
|---|---|---|
| $Co_{1.0}Ni_{0.0}$ LDH | +97 | -1 |
| $Co_{0.66}Ni_{0.34}$ LDH | +208 | +28 |
| $Co_{0.54}Ni_{0.46}$ LDH | +243 | +77 |
| $Co_{0.41}Ni_{0.59}$ LDH | +310 | +123 |
| $Co_{0.24}Ni_{0.76}$ LDH | +411 | +203 |
| $Co_{0.0}Ni_{1.0}$ LDH | +436 | +240 |

Cyclic voltammetry provides a measure of a supercapacitor's charge-response with regard to a changing voltage and is a measure of evaluating capacitance. The supercapacitance values calculated from the voltammograms are 574, 1102, 827, 514, 867 and 997 $F.g^{-1}$ of $Co_{1-x}$ $Ni_x$ LDHs electrode for the x values 0.0, 0.34, 0.46, 0.59, 0.76 and 1.0, respectively (Table 3.4). It is clear from Fig. 3.11 that, solitary $Ni(OH)_2$ alone shows higher capacitance than that of solitary $Co(OH)_2$. The performance of $Co_{1-x}$ $Ni_x$ LDHs for various x values along with specific and interfacial capacitance values is shown in Fig. 3.12. This could helpful for correct correlation in between capacitance and x values of $Co_{1-x}$ $Ni_x$ LDHs. From Fig.3.12 it was observed that, the combined supercapacitance of $Co_{1-x}$ $Ni_x$ LDHs is higher than that of individual $Ni(OH)_2$ and $Co(OH)_2$. The $Co_{0.66}Ni_{0.34}$ LDH is found to be an appropriate combination of $Co_{1-x}$ $Ni_x$ LDHs showed maximum supercapacitance of 1102 $F.g^{-1}$.

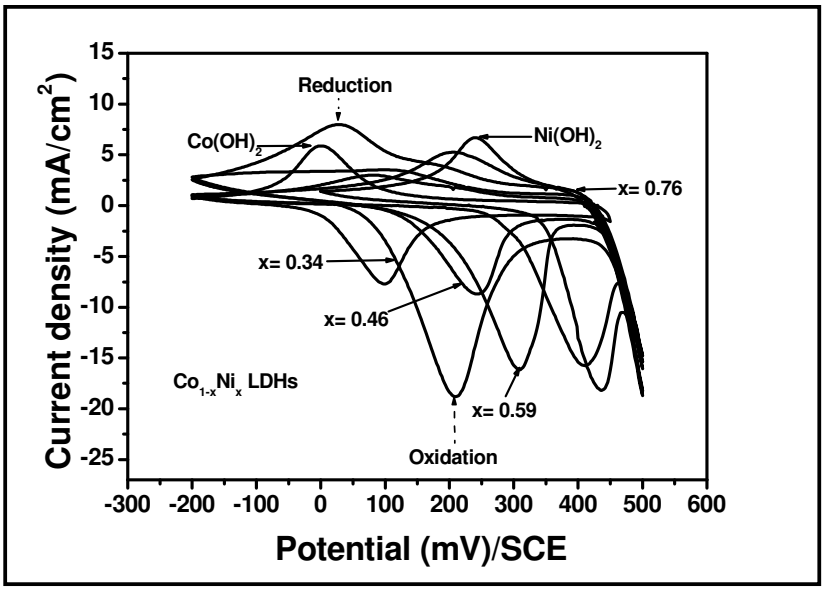


**Figure 3.11:** Cyclic voltammograms at different 'x' (Ni) values in $Co_{1-x}$ $Ni_x$ LDHs thin film electrodes in the 1M KOH electrolyte.

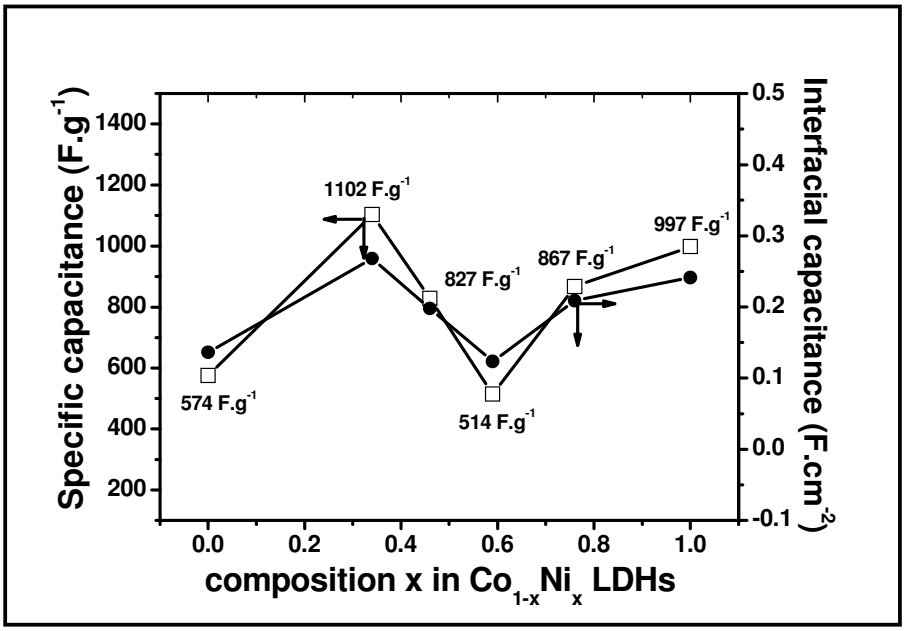


**Figure 3.12** Specific and interfacial supercapacitance at different 'x' (Ni) values in $Co_{1-x}$ $Ni_x$ LDHs film electrodes in 1M KOH at 50 $mV.s^{-1}$ scan rate.

From Fig. 3.12, it is clear that, with increased Ni proportion up to x = 0.34 in $Co_{1-x}Ni_x$ LDHs showed increasing capacitance. After that, further increased Ni content up to x = 0.59 showed drastic decrease in supercapacitance value up to 514 $F.g^{-1}$. Again further increased Ni from x= 0.59 to solitary $Ni(OH)_2$ showed rise in supercapacitance value up to 997 $F.g^{-1}$.

Fig. 3.12 showed graph of both interfacial and specific capacitance values versus x (Ni) values in $Co_{1-x}Ni_x$ LDHs, which indicated a valley like nature of graph.

**Table 3.4 Specific and interfacial capacitances at different 'x' (Ni) values in $Co_{1-x}Ni_x$ LDHs electrode.**

| **$Co_{1-x}Ni_x$ LDH** | **Interfacial capacitance ($F.cm^{-2}$)** | **Specific capacitance ($F.g^{-1}$)** |
|---|---|---|
| $Co_{1.0}Ni_{0.0}$ LDH | 0.136 | 574 |
| $Co_{0.66}Ni_{0.34}$ LDH | 0.268 | 1102 |
| $Co_{0.54}Ni_{0.46}$ LDH | 0.198 | 827 |
| $Co_{0.41}Ni_{0.59}$ LDH | 0.123 | 514 |
| $Co_{0.24}Ni_{0.76}$ LDH | 0.209 | 867 |
| $Co_{0.0}Ni_{1.0}$ LDH | 0.241 | 997 |

The data signified that the chemical composition factor also affects the electrochemical performance of combined material besides of morphology, valence state and other factors. According to this study, chemical composition is regarded to be the most significant aspect that

deals with the supercapacitance of $Co_{1-x}$ $Ni_x$ LDHs. Since now, only $Co_{0.66}Ni_{0.34}$ LDH film is used for further characterizations.

### 3.B.3.3 Effect of Electrolyte Concentration:

The effect of KOH electrolyte concentration on supercapacitance of $Co_{0.66}Ni_{0.34}$ LDH electrode was studied at 50 $mV.s^{-1}$ scan rate within the potential window of -200 to +500 mV/SCE. The CV curves of $Co_{0.66}Ni_{0.34}$ LDH electrode in KOH electrolyte for different concentrations (0.5 to 2M) is shown in Fig. 3.13. It is clearly observed that, current value under the curve rises with the KOH electrolyte concentration from 0.5 to 2M. The voltammogram of $Co_{0.66}Ni_{0.34}$ LDH showed saturation beyond 2M KOH concentration. The variation of interfacial and specific capacitance with electrolyte concentration at scan rate 50 $mV.s^{-1}$ for $Co_{0.66}Ni_{0.34}$ LDH electrode is shown in Fig. 3.14. The specific and interfacial capacitance values are increased from 996 to 1189 $F.g^{-1}$ and 0.23 to 0.289 $F.cm^{-2}$, respectively, as the electrolyte concentration increased from 0.5 to 2M (Table 3.5).

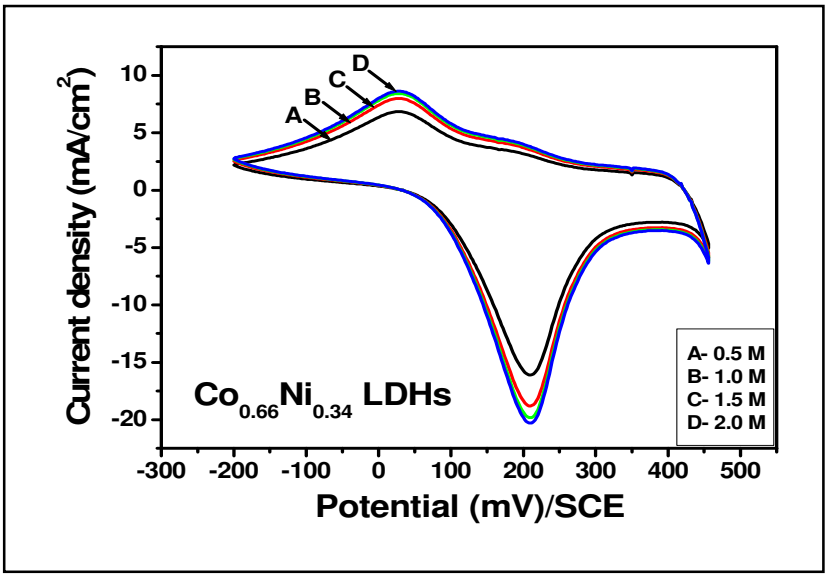


**Fig. 3.13** The CV curves of $Co_{0.66}Ni_{0.34}$ LDH electrode at different KOH electrolyte concentrations at 50 $mV.s^{-1}$.

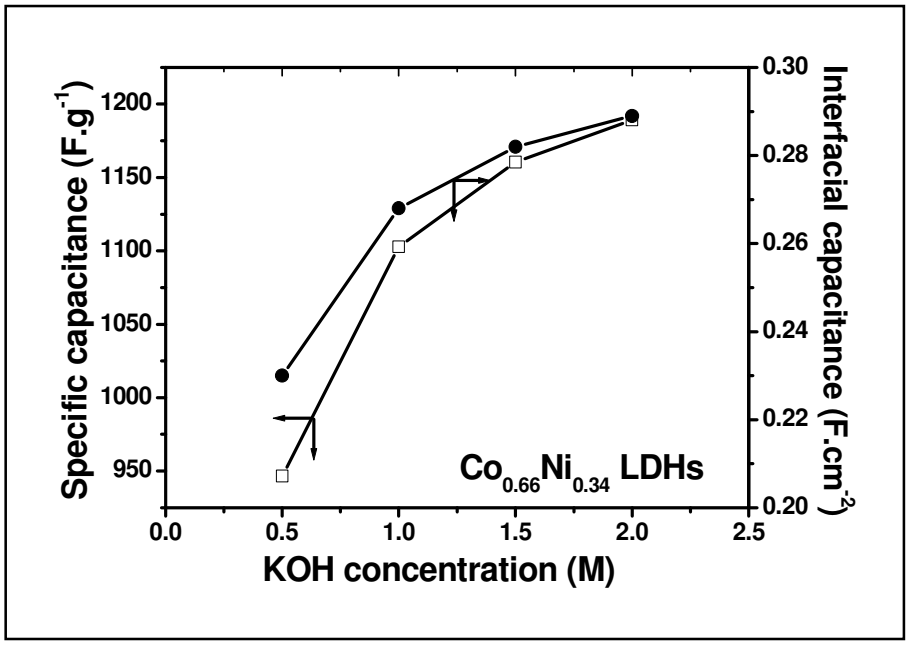


**Fig. 3.14** Variation of specific and interfacial capacitance with KOH concentration at scan rate 50 $mV.s^{-1}$ for $Co_{0.66}Ni_{0.34}$ LDH electrode.

**Table 3.5 Effect of electrolyte concentration on interfacial and specific capacitances of $Co_{0.66}Ni_{0.34}$ LDHs.**

| KOH Concentration (M) | $Co_{0.66}Ni_{0.34}$ LDHs | |
|---|---|---|
| | Interfacial capacitance ($F.cm^{-2}$) | Specific capacitance ($F.g^{-1}$) |
| 0.5 | 0.23 | 946 |
| 1.0 | 0.268 | 1102 |
| 1.5 | 0.282 | 1160 |
| 2.0 | 0.289 | 1189 |

As electrolyte concentration increased the current under curve is also increased resulted into increasing supercapacitance value of $Co_{0.66}Ni_{0.34}$ LDH electrode. This can be ascribed to the increase in number

of $K^+$ ions in the electrolyte. The applied potential difference across the electrodes in electrolyte solution results in redox reactions and development of charge on of the electrode surface. Electrostatic interactions causes ions in electrolyte solution transferred to electrode of opposite polarity to compensate the charge on the electrode.

Thus during charging-discharging, the ions move from one electrode to the other through the electrolyte causes simultaneous motion of electrons through the current source or through the external load. The specific and interfacial capacitances are increased with increasing the concentration of KOH electrolyte.

### 3.B.3.4 Effect of Scan Rate:

The voltammetric responses of $Co_{0.66}Ni_{0.34}$ LDH electrode at different scan rates are shown in Fig. 3.15.

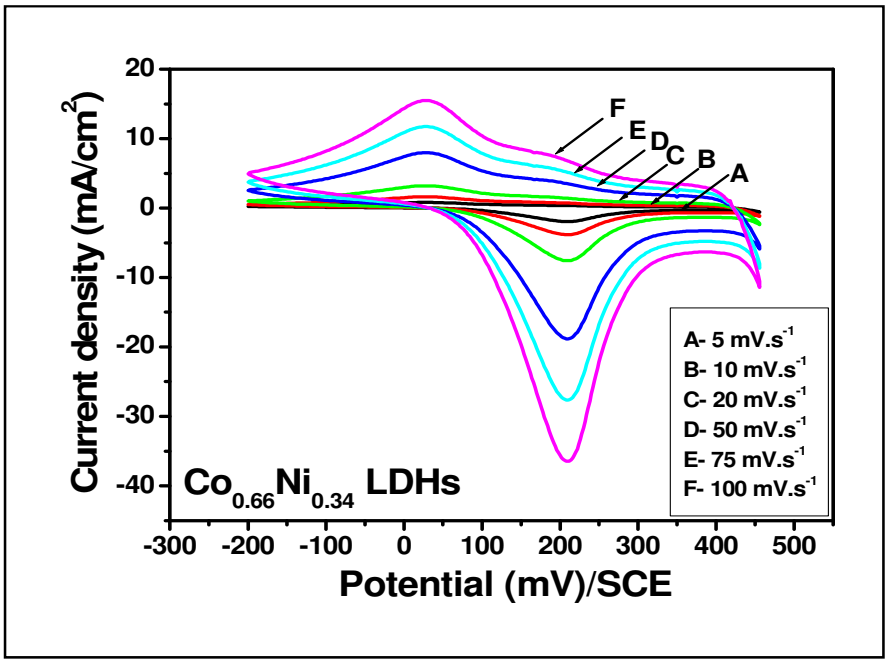


**Fig. 3.15** The CV curves of $Co_{0.66}Ni_{0.34}$ LDH electrode at different scanning rates in 2M KOH.

The effect of the scan rate 5 to 100 mV.s$^{-1}$ on supercapacitor was examined in 2M KOH within potential window of -200 to +500 mV/SCE. It was

observed that the current under curve is gradually increased with increase in scan rate, which showed direct proportion between voltammetric current and scan rate of voltammograms and hence signify an ideally capacitive behaviour [41].

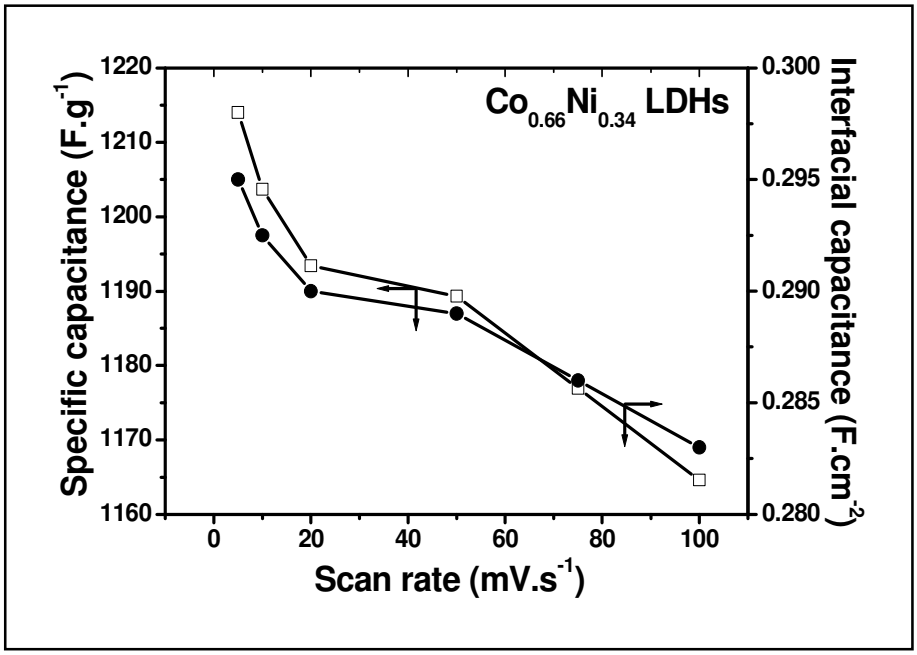


**Fig. 3.16:** Variation of specific and interfacial capacitance with scan rate for $Co_{0.66}Ni_{0.34}$ LDH electrode.

Figure 3.16 showed variation of specific capacitance and interfacial capacitance values with scan rate. The specific and interfacial capacitance values are decreased from 1213 to 1164 $F.g^{-1}$ and 0.295 to 0.283 $F.cm^{-2}$, respectively, as the scan rate was increased from 5 to 100 $mV.s^{-1}$ (Table 3.6). The decrease in capacitance value in accordance with the scan rate can be attributed to the presence of inner active sites, which cannot precede the redox transitions completely; probably due to the diffusion effect of proton within the electrode at higher scan rate of CV. Hence, the specific capacitance obtained at the slowest scan rate is believed to be

closest to that of full utilization of the electrode material. The maximum supercapacitance obtained for $Co_{0.66}Ni_{0.34}$ LDH electrode at 5 $mV.s^{-1}$ scan rate is ~1213 $F.g^{-1}$.

**Table 3.6 Effect of scan rate on interfacial and specific capacitances of $Co_{0.66}Ni_{0.34}$ LDHs.**

| Scan rate ($mV.s^{-1}$) | $Co_{0.66}Ni_{0.34}$ LDHs | |
|---|---|---|
| | Interfacial capacitance ($F.cm^{-2}$) | Specific capacitance ($F.g^{-1}$) |
| 5 | 0.295 | 1213 |
| 10 | 0.2925 | 1203 |
| 20 | 0.29 | 1193 |
| 50 | 0.289 | 1189 |
| 75 | 0.286 | 1176 |
| 100 | 0.283 | 1164 |

### 3.B.3.5 Charge-Discharge Study:

The electrode of $Co_{0.66}Ni_{0.34}$ LDH was used for galvanostatic charge–discharge cycling between 0 and +350 mV/SCE in 2M KOH solution at a current density of 5 $mA.cm^{-2}$. Figure 3.17 showed the characteristic curves of potential variation with cycling time of $Co_{0.66}Ni_{0.34}$ LDH electrode. One can observe redox characteristics in the charge–discharge curves which are directly related to the redox peaks in the CV curves. It can be seen that, the charge profile is symmetric and curved, suggesting a pseudocapacitive characteristic. From Fig. 3.17, it is observed that, time periods of charge

and discharge are almost the same, which means high reversibility and high Coulomb efficiency.

The electrical parameters, coulomb efficiency (η%), specific energy (SE) and specific power (SP) are estimated by using equations (3.8), (3.9) and (3.10), respectively. Coulomb efficiency (η%) of $Co_{0.66}Ni_{0.34}$ LDH electrode is found to be 93.87 %. The specific energy of 104 Wh/Kg and specific power of 1.44 KW/kg indicates significance of $Co_{0.66}Ni_{0.34}$ LDH electrode material for supercapacitor application.

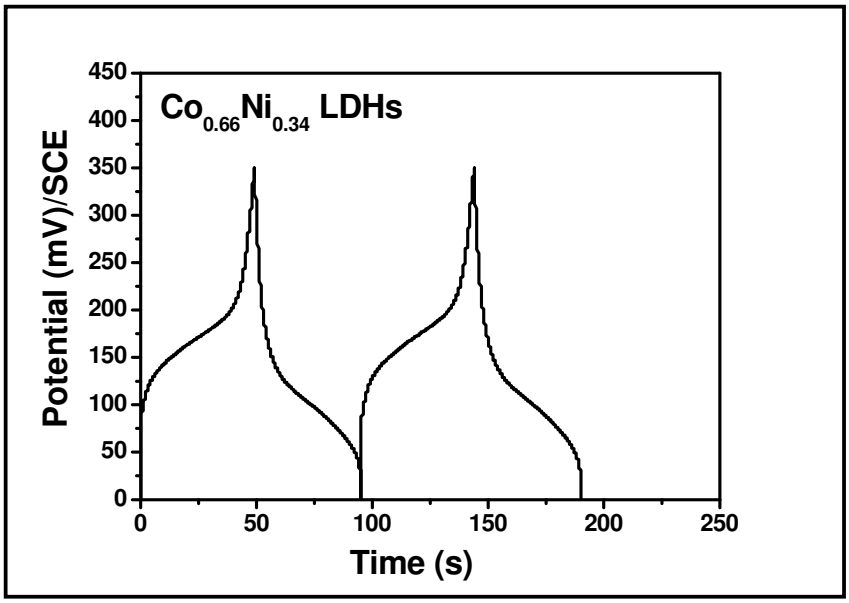


**Figure 3.17:** Galvanostatic charge–discharge curves of $Co_{0.66}Ni_{0.34}$ LDH electrode in 2M KOH electrolyte.

### 3.B.3.6 Electrochemical Impedance Analysis (EIS study):

Electrical conduction and ion transfer were investigated by electrochemical impedance spectroscopy (EIS) analysis. Figure 3.18 illustrated the complex–plane impedance plot of $Co_{0.66}Ni_{0.34}$ LDH electrode also known as Nyquist plot, for $Co_{0.66}Ni_{0.34}$ LDH; where Z' and Z'' are the real and imaginary parts of the impedance, respectively. It consists of a dispersed semi-circle in the higher frequencies, which is related to charge

transfer processes (Faradaic reaction kinetics) at the electrode electrolyte interfaces. And further its transition to a linear part with slope close to $45^0$ along the imaginary axis (Z'') at low frequencies indicates the characteristics of electrode controlled by the diffusive resistivity of the electrolyte due to a Warburg impedance (a limiting diffusion process). And this is not useful for charge storage. Theoretically, the net double-layer capacitance originated from reversible physical sorption must offer a parallel line to the imaginary axis of Nyquist plot [42]. Here the small deviation of experimental curve from the theoretical approach probably attributed to the different penetration depth of the alternating current signal in virtue of pore size distribution at the electrode arise unusual capacitance [43, 44] and the redox reaction at the $Co_{0.66}Ni_{0.34}$ LDH electrode gives rise to pseudocapacitance. The contact resistance between $Co_{0.66}Ni_{0.34}$ LDH particles and the current collector known as ESR is found 1.2 Ω as shown in the inset of Fig. 3.18 at magnified scale. This revealed that nano-flaked morphology leads to the low charge transfer resistance.

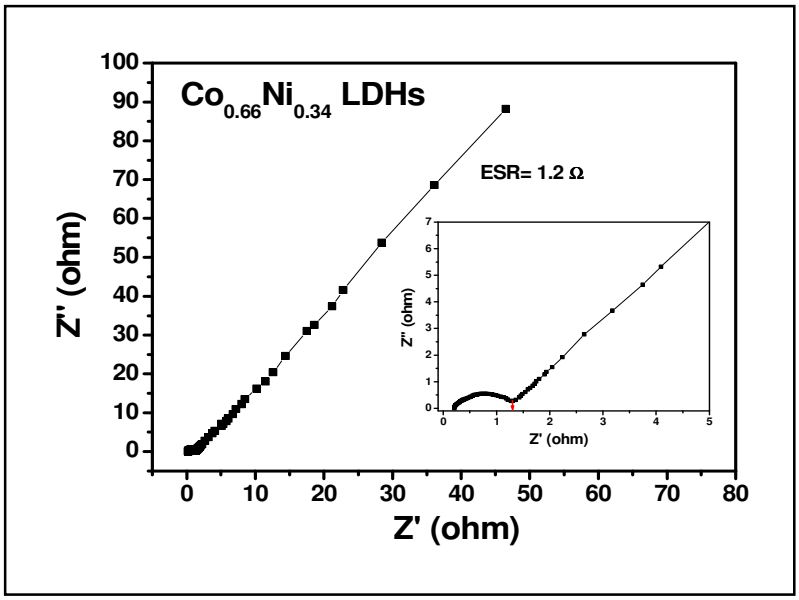


**Figure 3.18:** Nyquist plot of $Co_{0.66}Ni_{0.34}$ LDH electrode in 2M KOH.

### 3.B.3.5 Stability Study:

The stability of $Co_{0.66}Ni_{0.34}$ LDH electrode in 2M KOH was tested by CV. Fig. 3.19 showed the CV curves for 5th and 10000th number cycle. The current under curve is decreased by ~ 23% up to 10000 cycles. Hence, the stability of electrode retained to 77% after 10000th cycles at scan rate 100 $mV.s^{-1}$. We found that, our system can withstand about 10000 cycles without a considerable decrease in the capacity, exemplifying the stable nature of $Co_{0.66}Ni_{0.34}$ LDH electrode in energy storage application. Due to the loss of active material during the early charging discharging cycles in the electrolyte, decrement in the specific and interfacial capacitance values with higher number of cycles of $Co_{0.66}Ni_{0.34}$ LDH electrode was observed.

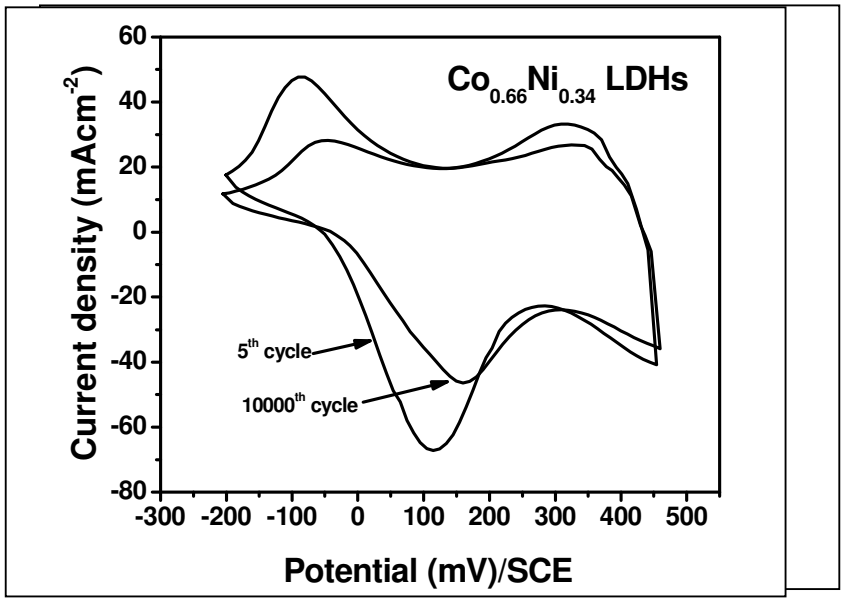


**Fig. 3.19:** Voltamomgrams of $Co_{0.66}Ni_{0.34}$ LDH electrode at scan rate 100 $mV.s^{-1}$ for 5th and 10000th cycles.

### Conclusions

The current chapter concluded that, the $Co_{1-x}Ni_x$ LDHs electrodes prepared by potentiodynamic method showed promising supercapacitor behavior. The nanostructured porous $Co_{1-x}Ni_x$ layered double hydroxides

($Co_{1-x}Ni_x$ LDHs), which exhibit both $Co(OH)_2$ and $Ni(OH)_2$, have been successfully deposited in the thin film form by potentiodynamic mode owing randomly oriented nano-flakes like morphology. The increase of Ni content (x = 0, 0.34, 0.46, 0.59, 0.76 and 1) in $Co_{1-x}Ni_x$ LDHs affects emerging surface morphological aspect. The $Co_{1-x}Ni_x$ LDHs films are superhydrophilic in nature. The $Co_{1-x}Ni_x$ LDHs showed higher pseudocapacitive performance than that of individual performance of $Co(OH)_2$ and $Ni(OH)_2$. The supercapacitance value increased with increase in electrolyte concentration and decreased with the scan rate. Maximal specific capacitance for $Co_{1-x}Ni_x$ LDHs electrode was found ~1213 $F.g^{-1}$, attaining specific energy of 104 Wh/kg and specific power of 1.44 KW/kg with ~ 94% of coulomb efficiency for composition $Co_{0.66}Ni_{0.34}$ LDH in 2M KOH electrolyte. The stability of electrode retained to 77% after $10000^{th}$ cycles. Therefore, $Co_{0.66}Ni_{0.34}$ LDH composition is more feasible and found to be potential candidate for supercapacitor application.

**References:**


1 F.Y. Cheng, J. Chen, X.L. Gou, P.W. Shen, Adv. Mater., 17 (2005) 2753.

2 M. Holzapfel, H. Buqa, W. Scheifele, P. Novaka, F.M. Petrat, Chem. Commun., 152 (2005) 1566.

3 K. Kang, Y.S. Meng, J. Breger, C.P. Grey, G. Ceder, Science, 311 (2006) 977.

4 J. Cho, Y.W. Kim, B. Kim, J.G. Lee, B. Park, Angew. Chem. Int. Ed., 42 (2003) 1618.

5 J. Ismail, M.F. Ahmed, P.V. Kamath, J. Power Sources, 36 (1991) 507.

6 V. Gupta, S. Gupta, N. Miura, J. Power Sources, 175 (2008) 680.

7 Y. Kobayashi, X.L. Ke, H. Hata, P. Schiffer, T.E. Mallouk, Chem. Mater., 20 (2008) 2374.

8 C. Delmas, Y. Borthomieu, J. Solid State Chem., 104 (1993) 345.

9 W.E.G. Hansal, B. Tury, M. Halmdienst, M.L. Varsanyi, W. Kautek, Electrochim. Acta, 52 (2006) 1145.

10 M. Murthy, G.S. Nagarajan, J.W. Weidner, J.W. Van Zee, J. Electrochem. Soc., 143 (1996) 2319.

11 V. Sudha, M.V. Sangaranarayanan, J. Phys. Chem. B, 106 (2002), 2699.

12 M.P. Pardave, I. González, A.B. Soto, E.M. Arce, J. Electroanal.Chem., 443 (1998) 125.

13 A.B. Soto, E.M. Arce, M.P. Pardave, I. Gonzalez, Electrochim. Acta, 41 (1996) 2647.

14 Y. Wang, F. Zhang, S. Xu, X. Wang, D.G. Evans, X. Duan, Ind. Eng. Chem. Res., 47 (2008) 5746.

15 Z. Liu, R. Ma, M. Osada, K. Takada, T. Sasaki, J. Am. Chem. Soc., 127 (2005) 13869.

16 A.C. Scheinost, D.L. Sparks, J. Collod. Interface Sci., 223 (2000) 167.

17 L.D. Guerlou, C. Denage, C. Delmas, J. Power Sources, 52 (1994) 269.

18 L. Bing, Y. Huatang, Z. Yunshi, Z. Zuoxiang, S. Deying, J. Power Sources, 79 (1999) 277.

19 K. Nakamoto, Infrared and Raman spectra of inorganic and coordination compounds. New York: Wiley; 1986.

20 A.H. Zimmerman, J. Power Sources, 12 (1984) 233.

21 F. Portemer, A.D. Vidal, M. Figlarz, J. Electrochem. Soc., 139 (1992) 671.

22 P.V. Kamath, G.N. Subbanna, J. Appl. Electrochem., 22 (1992) 478.

23 X.M. Ni, Q.B. Zhao, B.B. Li, J. Cheng, H.G. Zheng, Solid State Commun., 137 (2006) 585.

24 G.S. Illia, M. Jobbagy, A.E. Regazzoni, M.A. Blesa, Chem. Mater., 11 (1999) 3140.

25 Z. Hu, Y. Xie, Y. Wang, H. Wu, Y. Yang, Z. Zhang, Electrochim. Acta, 54 (2009) 2737.

26 L.T. Lam, R. Louey, J. Power Sources, 158 (2006) 1140.

27 J.R. Miller, Electrochim. Acta, 52 (2006) 1703.

28 B.E. Conway, Electrochemical Supercapacitors, Kluwer–Plenum, New York 1999.

29 V. Gupta, T. Kusahara, H. Toyama, S. Gupta, N. Miura, Electrochem. Commun., 9 (2007) 2315.

30 S.R.S. Prabaharan, R. Vimla, Z. Zainal, J. Power Sources, 161 (2006) 730.

31 C.C. Hu, W.C. Chen, Electrochem. Acta, 49 (2004) 3469.

32 Z. Fan, J. Chen, K. Cui, F. Sun, Y. Xu, Y. Kuang, Electrochem. Acta, 52 (2007) 2959.

33 D.D. Zhao, S.S. Bao, W.J. Zhou, H.L. Li, Electrochem. Commun., 9 (2007) 869.

34 Y.Y. Liang, S.J. Bao, H.L. Li, J. Solid State Electrochem., 11 (2007) 571.

35 T.N. Ramesh, M. Rajamathi, P.V. Kamath, Solid State Ionics, 5 (2003) 751

36 Q.L. Fang, D.A. Evans, S.L. Roberson, J.P. Zheng, J. Electrochem. Soc., 148 (2001) A833.

37 K.R. Prasad, N. Munichandraiah, J. Power Sources, 112 (2002) 443.

38 W. Yong-gang, Z. Xiao-gang, Electrochim. Acta, 49 (2004) 1957.

39 E. Frackowiak , F. Beguin, Carbon, 39 (2001) 937.

40 H.K. Xin, Z. Xiaogang, L. Juan, Electrochim. Acta, 51 (2006) 1289.

41 J.N. Broughton, M.J. Brett, Electrochem. Solid State Lett., 5 (2002) A279.

42 S. Sarangapani, B.V. Tilak, C.P. Chen, J. Electrochem. Soc., 143 (1996) 3791.

43 J.M. Honig, in Electrodes of Conductive Metallic Oxides, S. Trasatti, Editor Elsevier, Amsterdam (1980), Part A, Chap. 1, p. 1.

44 J.W. Long, K.E. Swider, C.I. Merzbacher, D.R. Rolison, Langmuir, 15 (1999) 780.

# CHAPTER IV

## Preparation, Characterization and Supercapacitance Evaluation of $Co_{1-x}Ni_x$ LDHs Films Deposited By Galvanostatic Mode

## CHAPTER IV

# SECTION (I)

# PREPARATION AND CHARACTERIZATION OF $Co_{1-x}Ni_x$ LDHs FILMS DEPOSITED BY GALVANOSTATIC MODE

## 4.A.1 Introduction:

In previous chapter, we have successfully deposited $Co_{1-x}Ni_x$ LDHs thin films by potentiodynamic mode of electrodeposition and studied their supercapacitive properties. In order to study the effect of, constant current density on structural, morphological properties of $Co_{1-x}Ni_x$ LDHs thin films we have continued with galvanostatic mode of electrodeposition. Kong et al. used in-situ spectroscopic ellipsometry to investigate the electrochemical deposition of nickel hydroxide films by galvanostatic mode [1]. The research has sought to model the electrochemical precipitation process [2], quantify the effects of experimental operating conditions on film growth [3, 4] and characterize the electrochemical behaviour of the deposit [5-7].

This chapter deals with preparation and characterization of $Co_{1-x}Ni_x$ LDHs thin films by galvanostatic mode in order to check the effect on the structural and morphological properties. This chapter includes two sections. In section (I) preparation and characterization of $Co_{1-x}Ni_x$ LDHs thin films via galvanostatic deposition with effect of composition variation on structural, morphological and wettability properties have been examined. In section (II) the supercapacitive evaluation of $Co_{1-x}Ni_x$ LDHs thin films have been studied.

## 4.A.2 Experimental Setup For $Co_{1-x}Ni_x$ LDHs Thin Films Deposition:

The description of experimental setup for deposition of $Co_{1-x}Ni_x$ LDHs thin films is given in the chapter no. 3 (section 3.A.2).

### 4.A.3 Experimental Details:

The galvanostatic electrodeposition of $Co_{1-x}Ni_x$ LDHs thin films were carried out from aqueous precursor solution bath of cobalt and nickel nitrate. In order to deposit $Co_{1-x}Ni_x$ LDHs, molar concentration of cobalt and nickel nitrate precursors were varied from 0.05 M to 0.2 M. The deposition was performed at different constant current densities from 1 to 5 $mA.cm^{-2}$ at various bath temperatures from 300 K to 333 K. Out of which, the room temperature (300 K) deposition carried out in 0.1 M nitrate precursor's solution at constant current density value 2 $mA.cm^{-2}$ results smooth, uniform and good quality thin films with high adhesion.

**Table 4.1: Optimized preparative conditions for galvanostatic deposition of $Co_{1-x}Ni_x$ LDHs thin films.**

| Film | $Co_{1-x}Ni_x$ LDHs | | | | | |
|---|---|---|---|---|---|---|
| Medium | Aqueous | | | | | |
| Bath composition | $Co(NO_3)_2.6H_2O$:$Ni(NO_3)_2.6H_2O$ | | | | | |
| | 1.0:0.0 | 0.75:0.25 | 0.60:0.40 | 0.50:0.50 | 0.25:0.75 | 0.0:1.0 |
| Total quantity | 30 ml | | | | | |
| pH | ~6 | | | | | |
| Current density | 2 $mA.cm^{-2}$ | | | | | |
| Temperature | 300 K | | | | | |
| Substrate | Stainless steel | | | | | |

The baths were prepared by varying composition of $Co(NO_3)_2$:$Ni(NO_3)_2$ solution as 1.0:0.0, 0.75:0.25, 0.60:0.40, 0.50:0.50, 0.25:0.75 and 0.0:1.0; for the galvanostatic deposition of $Co_{1-x}Ni_x$ LDHs onto cost effective stainless steel. Table 4.1 showed the optimized preparative parameters for galvanostatic deposition of $Co_{1-x}Ni_x$ LDHs films feasible for supercapacitor application.

### 4.A.4 Results and Discussion:

#### 4.A.4.1 Galvanostatic Deposition of $Co_{1-x}$ $Ni_x$ LDHs and Film Formation:

Figure 4.1 shows the potential-time curves for 0.1 M solutions of $Ni(NO_3)_2$, $Co(NO_3)_2$ and $Co(NO_3)_2$ + $Ni(NO_3)_2$ at bath compositions 0.0:1.0, 1.0:0.0 and 0.5:0.5 on stainless steel substrate, respectively at current density 2 $mA.cm^{-2}$.

From potential-time curves it is observed that, during the galvanostatic (cathodic) deposition, the potential increases instantaneously in negative manner and after a sudden small decrease, it reaches a steady-state potential value. The potential is seen to be stabilized at shorter duration at supplied current density of 2 $mA.cm^{-2}$. This trend is a typical characteristic pertaining to the growth mechanism of the $Co_{1-x}Ni_x$ LDHs film formation. The nature of the plot determines the nucleation and growth of $Co_{1-x}Ni_x$ LDHs thin films. Initially potential was raised suddenly to -1050 mV/SCE due to the activation of space charge region for cobalt nitrate bath. And with increase in nickel content this potential shifts towards less negative value upto -870 mV/SCE, afterwards started to decrease at one point at which the continuous growth of $Co_{1-x}Ni_x$ LDHs is observed. In presence of Ni, the potential of nucleation part was lower and the current density versus time variation was steady. In addition, the steady flow of potential after nucleation process, implying uniform growth of $Co_{1-x}Ni_x$ LDHs.

The electrochemical reaction mechanism involved in the formation of $Co_{1-x}Ni_x$ LDHs can be explained through the electrogeneration of base route.

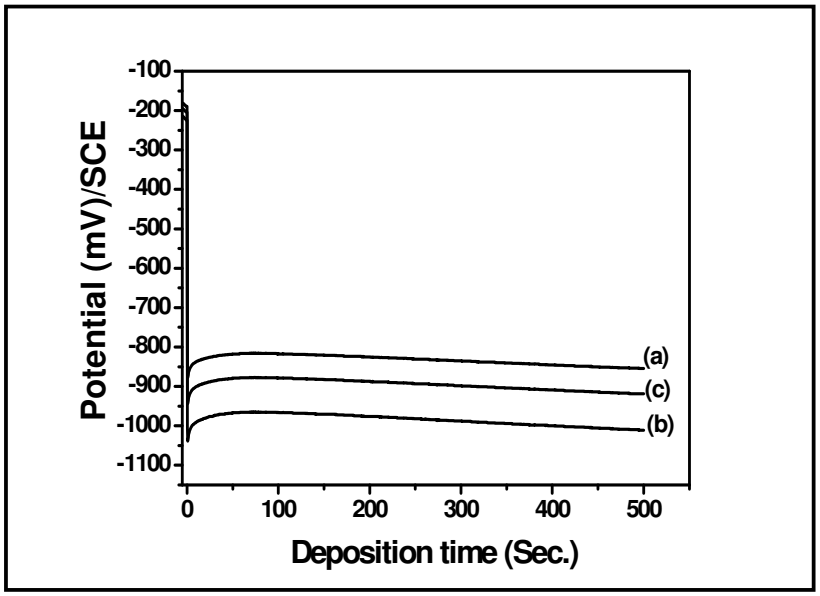


**Figure 4.1** A potential-time transients (galvanostatic curves) for 0.1 M solution of (a) $Ni(NO_3)_2$, (b) $Co(NO_3)_2$ and (c) $Co(NO_3)_2$+$Ni(NO_3)_2$ with bath composition 0.0:1.0, 1.0:0.0 and 0.5:0.5 onto stainless steel substrate atcurrent density 2 $mA.cm^{-2}$.

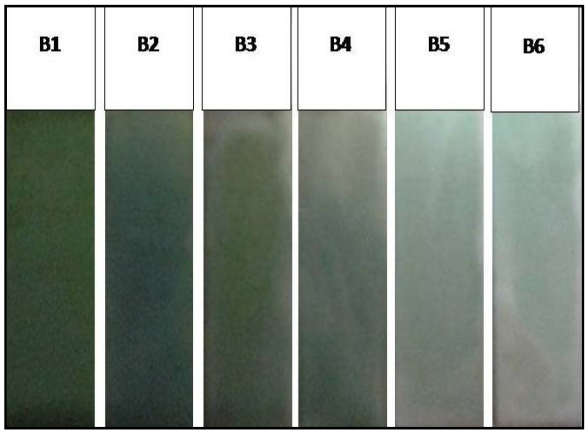


**Figure. 4.2:** Photograph of $Co_{1-x}$ $Ni_x$ LDHs thin films with $Co(NO_3)_2$:$Ni(NO_3)_2$ bath compositions B1 (1.0:0.0), B2 (0.75:0.25), B3 (0.6:0.4), B4 (0.5:0.5), B5 (0.25:0.75), B6 (0.0:1.0).

At the moment the power is on, the cathode (stainless steel) substrate is conductive and $OH^-$ ions are generated over its entire surface by the reduction of nitrate anion species. This increases the local pH near cathode which is promoting $Co_{1-x}Ni_x$ LDHs deposition.

When the electromigrated metal ions (Co and Ni) reach the cathodic surface, the $Co_{1-x}Ni_x$ LDHs film starts growing. Therefore, at constant current value of 2 $mA.cm^{-2}$, the deposition of greenish coloured, uniform and well adherent $Co_{1-x}Ni_x$ LDHs thin film with various compositions were obtained as shown in Fig. 4.2.

### 4.A.4.2 Thickness Measurement:

Figure 4.3 showed variation of deposited weight of $Co_{1-x}Ni_x$ LDHs for different bath compositions of $Co(NO_3)_2$:$Ni(NO_3)_2$ solution.. The thickness in terms of weight of $Co_{1-x}Ni_x$ LDHs film deposited is carried out at fixed (cathodic) current density of 2 $mA.cm^{-2}$ for optimized time period of 500 s at room temperature.

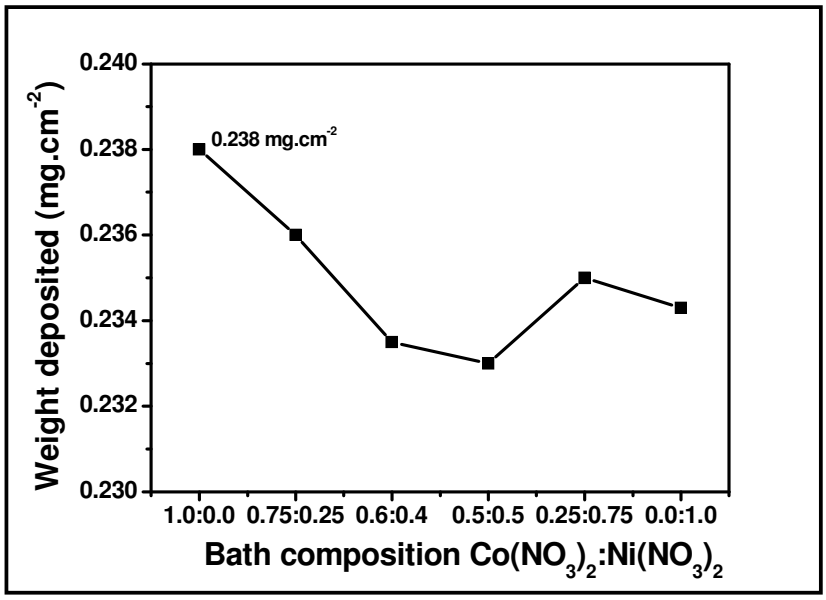


**Figure 4.3:** $Co_{1-x}Ni_x$ LDHs thin film thickness for various bath compositions of $Co(NO_3)_2$:Ni $(NO_3)_2$.

The thickness varied accordingly bath composition of cobalt and nickel nitrate solutions (from 1.0:0.0 to 0.0:1.0) within range of 0.233 to

0.238 mg.cm$^{-2}$. The maximum thickness of $Co_{1-x}Ni_x$ LDHs film was obtained for 1.0:0.0 composition, i.e. deposition rate of solitary $Co(OH)_2$ is more. From Fig. 4.3 it is observed that, with increase in the Ni proportion, thickness of $Co_{1-x}Ni_x$ LDHs film decreased gradually to 0.233 mg.cm$^{-2}$ for 0.5:0.5 bath composition and again increased up to solitary deposition of $Ni(OH)_2$.

This implied that, for constant deposition current and deposition time the rate of deposition decreases with increasing Ni content in $Co_{1-x}Ni_x$ LDHs and beyond it increased to solitary deposition of $Ni(OH)_2$.

### 4.A.4.3 Structural Characterization:

The structural analysis of deposited films was carried out by X-ray diffraction technique. The XRD patterns with various compositions of $Co_{1-x}Ni_x$ LDHs films onto stainless steel substrate are shown in Fig 4.4. The origin of diffraction peaks correspond to the characteristic reflections of LDHs materials with a series of (00l) peaks arising from the basal reflection appearing as narrow symmetric lines at low angle in the 2θ range 10°-90°.

The major peaks in diffraction patterns indicated crystalline structure of the $Co_{1-x}Ni_x$ LDHs thin films, wherein B1 and B6 are individual $Co(OH)_2$ and $Ni(OH)_2$, respectively. The diffraction peaks are directly associated to good crystallinity of the deposited films of $Co_{1-x}Ni_x$ LDHs. The strong diffraction peaks among them correspond with SS substrate are indexed with the star occurred at 2θ values ~50.7° and ~74.6°. In particular, the reflections of the planes (001), (100), (101) and (110) are the basis for peaks appearing at 2θ values of ~12° (7.3 Å), ~34° (2.63 Å), ~43.5° (2.07 Å), ~60° (1.50 Å), respectively; which jointly associates with formation only α-$Co(OH)_2$ and α-$Ni(OH)_2$ in support with JCPDS card no. 74-1057 and 38-0715, respectively [8].

The d-spacing of β-$Co(OH)_2$ and β-$Ni(OH)_2$ has a lower value (~ 4.6 Å) than that of α-phase and consistent with a close packing of hydroxide layers. Whilst the d-spacing of α-$Co(OH)_2$, α-$Ni(OH)_2$ and the LDHs samples is in average greater than 7 Å [9]. It was hard to differentiate between the two phases, due to similar structures and very close occurrence of their diffraction peaks [10].

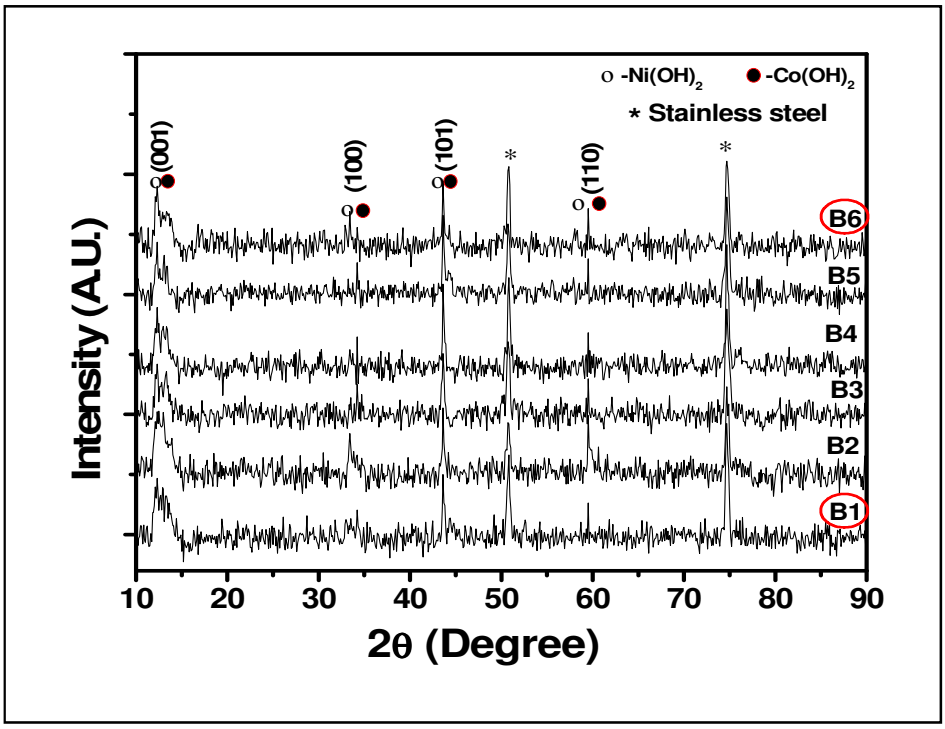


**Figure 4.4:** X-ray diffractograms of $Co_{1-x}Ni_x$ LDHs thin films for various bath compositions of $Co(NO_3)_2$:$Ni(NO_3)_2$ on stainless steel substrate.

### 4.A.4.4 FT-IR study:

The FT-IR absorption spectra of $Co_{1-x}Ni_x$ LDHs thin films is additional support to XRD study within range 4000–400 $cm^{-1}$ as shown in Fig. 4.5. In the spectra B1 (1.0:0.0), B4 (0.5:0.5) and B6 (0.0:1.0); broad peak around 3480 $cm^{-1}$ is attributed to O-H stretching mode due to existence of hydrogen bonding between H atoms and intercalated

anions or water molecules within the layer [11, 12]. The peak at 1645 $cm^{-1}$ corresponds to angular deformation of molecular water. The band around 1376 $cm^{-1}$ is characteristics of interlayer $NO_3^-$ anions stretching [13]. The origination of small peak at 670 and 648 $cm^{-1}$ can be ascribed to Co-$O^{2-}$ and δ Ni-O-H vibration, respectively. While the individual occurrence of bands near 466 and 435 $cm^{-1}$ corresponds to stretching vibration of Ni-O and Co-O in B6 and B1, respectively are also observed in B4 sample spectrum [14]. Therefore, obtained FT-IR spectra are also supportive to the formation of cobalt and nickel hydroxide phases in galvanostatic deposit.

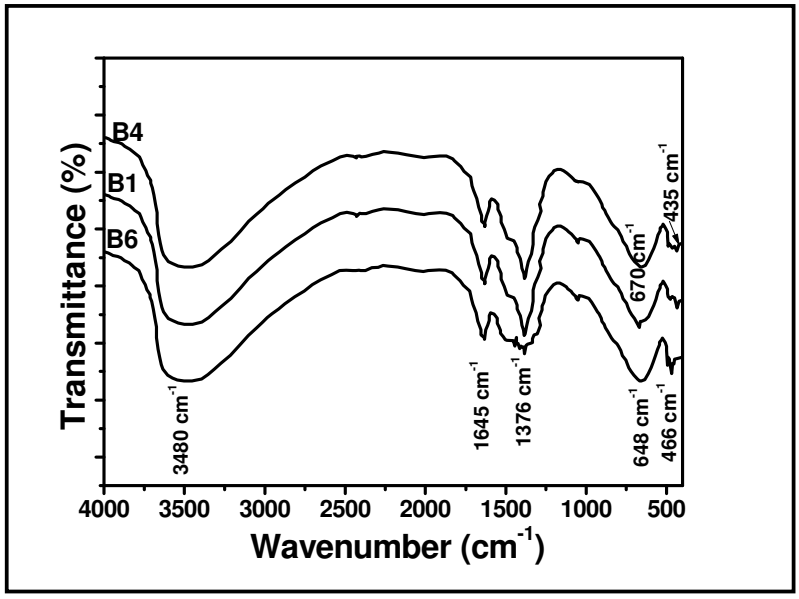


**Figure 4.5:** FT-IR spectra of $Co_{1-x}Ni_x$ LDHs for B1 (1.0:0.0), B4 (0.5:0.5) and B6 (0.0:1.0) bath compositions of $Co(NO_3)_2$:$Ni(NO_3)_2$.

### 4.A.4.5 Surface Morphological (SEM) and Compositional Studies (EDS):

The surface morphologies of the $Co_{1-x}Ni_x$ LDHs thin films were investigated by scanning electron microscopy (SEM) and the micrographs of various bath compositions at ×10,000 magnifications are shown in Fig. 4.6 (B1-B6). From the SEM images, it is clearly observed that, the

galvanostatic deposition significantly altered the morphology of $Co_{1-x}Ni_x$ LDHs along with different compositions. The $Co_{1-x}Ni_x$ LDHs thin films showed composition dependent microstructure owing randomly grown nano-flakes like morphology.

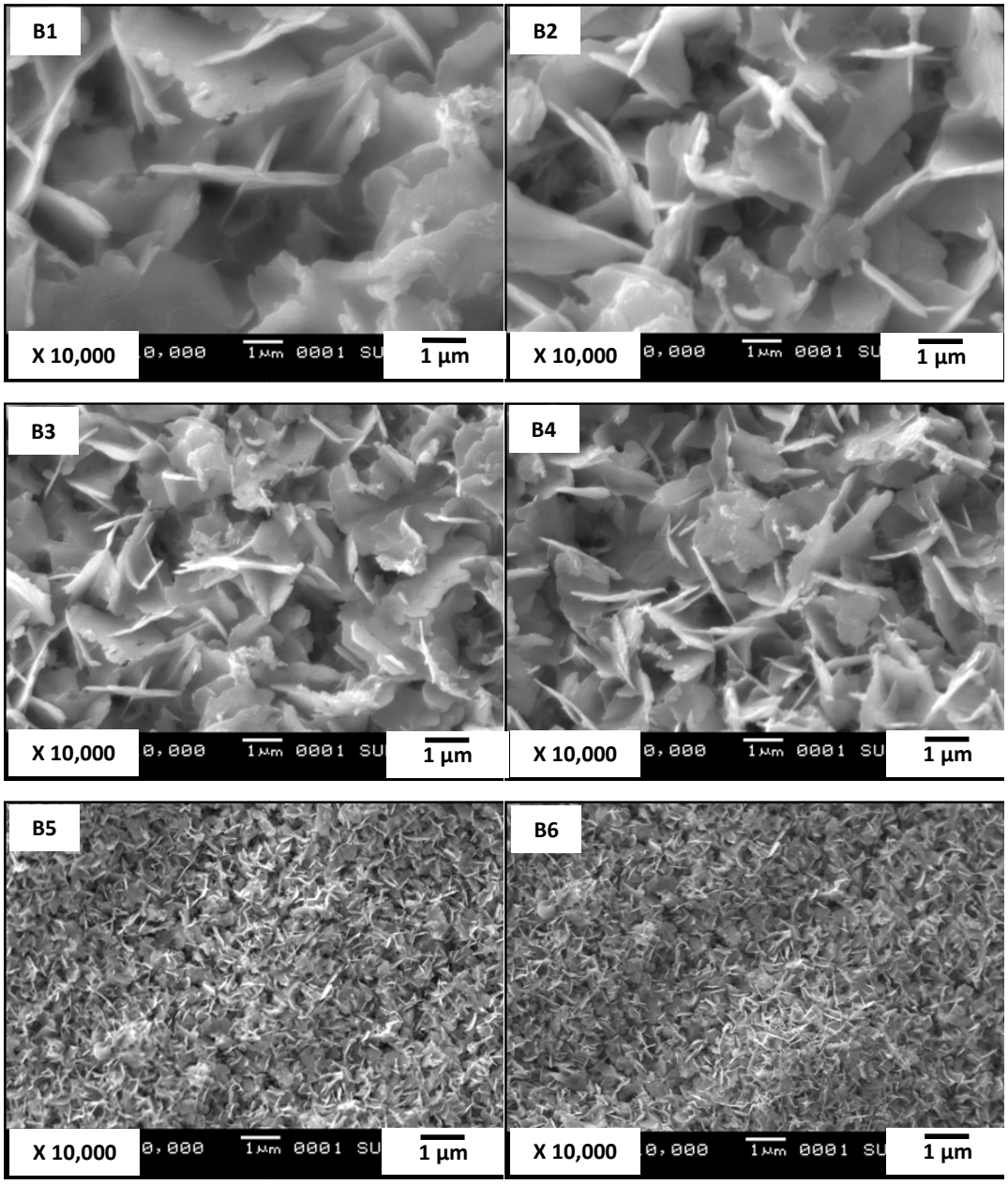


**Figure 4.6:** SEM micrographs of $Co_{1-x}Ni_x$ LDHs thin film for samples B1 (1.0:0.0), B2 (0.75:0.25), B3 (0.6:0.4), B4 (0.5:0.5), B5 (0.25:0.75) and B6 (0.0:1.0) at X 10,000 magnification.

Herein, obtained morphology is more compact and distinct as compared with earlier obtained morphologies by potentiodynamically deposited $Co_{1-x}Ni_x$ LDH films. As there is not significant decay and fluctuation in potential were observed during galvanostatic deposition of $Co_{1-x}Ni_x$ LDH; however, in case of such decrease in potential during the galvanostatic deposition can ascribed to the formation of pores on the deposited layer, due to the field assisted dissolution of the film. Hence, emerging morphologies for galvanostatic mode of deposition of $Co_{1-x}Ni_x$ LDH showed thicker and larger sized flakes owing compact nature with less porosity.

The sample B1 showed morphology of (cobalt hydroxide) with microstructure seized with thicker nano sheets with bigger flakes size. The change observed for sample B2 with increase of Ni content in $Co_{1-x}Ni_x$ LDHs, was only the slight decrease in sheet width and flake size. As Ni content in $Co_{1-x}Ni_x$ LDHs was increased, the growing microstructure get shrinked and morphology became more and more compact with reduction in flake size and sheet width as shown in Fig. 4.6 (B1-B6). Among them sample B5 and B6 were Ni rich compositions of $Co_{1-x}Ni_x$ LDHs showed more compact microstructure with fine, thin and sharp flaked morphology incorporated collective growth. The increased Ni amount may stimulate flakes growth collectively and merging them to form compact shrinked microstructure with decrease in the individual size of flakes and flake width.

Thus the results signified that, the Ni content in $Co_{1-x}Ni_x$ LDHs transforms the surface morphological properties of $Co_{1-x}Ni_x$ LDH electrode [10]. The observed results are in good agreement with the earlier $Co_{1-x}Ni_x$ LDHs films deposited by potentiodynamic mode.

Table 4.2 shows the atomic percentages (at %) of the elements Co and Ni in $Co_{1-x}Ni_x$ LDHs, obtained by energy-dispersive X-ray spectroscopy (EDS). The elemental composition specify that the $Co_{1-x}Ni_x$ LDHs are

composed of $Co(OH)_2$ and $Ni(OH)_2$ in concert. From the EDS data it is found that, the amount of oxygen (not shown in table) was quite high than the Co and Ni combined. The slightly higher content of oxygen may be due to water of hydration as well as absorbed water [10]. From EDS analysis, the formula of $Co_{1-x}Ni_x$ LDHs would be $[Co(OH)_2]_{1-x}[Ni(OH)_2]_x$ with x= 0, 0.18, 0.27, 0.51, 0.64 and 1, found from the galvanostatic deposition of $Co(NO_3)_2$:$Ni(NO_3)_2$ solutions for compositions 1.0:0.0, 0.75:0.25, 0.60:0.40, 0.50:0.50, 0.25:0.75 and 0.0:1.0 for samples B1 to B6, respectively.

**Table 4.2: EDS analysis of Co, Ni in galvanostatically deposited $Co_{1-x}Ni_x$ LDHs, for various compositions of $Co(NO_3)_2$ and $Ni(NO_3)_2$.**

| Sample | Co:Ni | Co (at%) | Ni (at%) | (x) in $[Co(OH)_2]_{1-x}[Ni(OH)_2]_x$ |
|---|---|---|---|---|
| B2 | 0.75:0.25 | 40.54 | 8.9 | 0.18 |
| B3 | 0.60:0.40 | 38.66 | 14.3 | 0.27 |
| B4 | 0.50:0.50 | 11.62 | 12.1 | 0.51 |
| B5 | 0.25:0.75 | 15.11 | 26.3 | 0.64 |

### 4.A.4.6 Surface Wettability Study:

Wettability test is carried out to investigate the interaction between the electrolyte and $Co_{1-x}Ni_x$ LDHs thin films. Figure 4.7 (a-e) showed the photographs of water contact with the $Co_{1-x}Ni_x$ LDHs thin films. The morphological evolution by the galvanostatic deposition has significant impact on the surface wettabilty properties of the $Co_{1-x}Ni_x$ LDHs thin films. From Fig. 4.7 (a-e) it is clearly seen that for samples B1 to B6, water drop set resting on the surface of $Co_{1-x}Ni_x$ LDHs film, with contact angle values varied from 19° to 34 °, respectively. The increase in water contact angle values can be incorporated to increase in Ni content in the $Co_{1-x}Ni_x$ LDHs, offered gradual increase in compacticity of film surfaces and diminished porosity of microstructures.

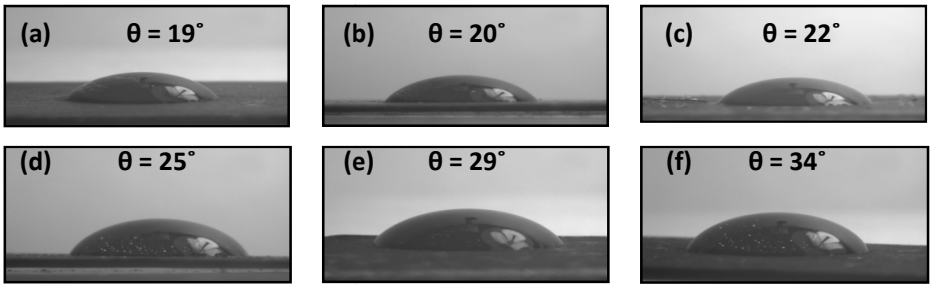


**Figure 4.7:** Measurement of water contact angle of $Co_{1-x}Ni_x$ LDHs samples (a) B1 (1.0:0.0), (b) B2 (0.75:0.25), (c) B3 (0.60:0.40), (d) B4 (0.50:0.50), (e) B5 (0.25:0.75) and (f) B6 (0.0:1.0).

In general, surface wettability study depicted hydrophilic behaviour of $Co_{1-x}Ni_x$ LDHs films, which possess high surface energy and enhances with decrease in flake size. Also hydrophilicity of the $Co_{1-x}Ni_x$ LDHs films can be linked with hydrous nature of layered hydroxides films. Hydrous bonding on the substrate surface is also origin for hydrophilic nature. Therefore, we observed that galvanostatically deposited $Co_{1-x}Ni_x$ LDHs films through increase in Ni proportion with modified morphologies lead to increase in contact angle values. Hydrophilic $Co_{1-x}Ni_x$ LDHs films are appropriate for supercapacitive application in which access of aqueous electrolyte ions to electrode surface occurs easily.

## SECTION (II)

## SUPERCAPACITIVE EVALUATION OF GALVANOSTATICALLY DEPOSITED $Co_{1-x}Ni_x$ LDHs THIN FILMS

### 4.B.1 Introduction:

In this current effort, $Co_{1-x}Ni_x$ LDHs thin films have been successfully deposited by galvanostatic mode and used as supercapacitor electrodes. Effect of electrolyte concentration and scan rate on supercapacitance of $Co_{1-x}Ni_x$ LDHs electrodes have been examined along with stability, charging–discharging and impedance characteristics.

### 4.B.2 Experimental Details and Supercapacitance Evaluation:

#### 4.B.2.1 Experimental Set Up for Supercapacitor Study:

The description of experimental setup for supercapacitance study of $Co_{1-x}Ni_x$ LDHs thin films is given in the chapter no. 3 (section 3.B.2.1).

### 4.B.3 Results and Discussion:

#### 4.B.3.1 Effect of Different Electrolytes:

The details of effect and basic needs concerning the use of appropriate electrolyte were described in the previous chapter no. 3 (Section 3.B.3.1). The aqueous KOH electrolyte is used, which attained the maximum current than that of other electrolytes. Therefore, KOH electrolyte is used for further study of supercapacitive properties of $Co_{1-x}Ni_x$ LDHs thin films.

#### 4.B.3.2 Supercapacitance of $Co_{1-x}Ni_x$ LDHs Film:

Figure 4.8 showed typical cyclic voltammograms of galvanostatically deposited $Co_{1-x}Ni_x$ LDHs electrode for various x values (x= 0.0 to 1.0) in aqueous 1M KOH electrolyte at scan rate of 50 $mV.s^{-1}$ within optimized potential window of -200 to +500 mV/SCE. All

voltammograms showed two redox peaks due to Faradaic reactions of $Co(OH)_2$ and $Ni(OH)_2$ depicts pseudocapacitive character of $Co_{1-x}Ni_x$ LDHs [15, 16].

Fig. 4.8 clearly indicated the shifts in the redox peaks in accordance with composition of the $Co_{1-x}Ni_x$ LDHs. The redox peaks get shifted towards more positive potential values with increase of Ni content in $Co_{1-x}Ni_x$ LDHs within specified voltage range. The quasi-reversible electron transfer process is observable in all voltammograms, signifying the measured capacitance is mainly due to redox mechanism [17]. The integral area and redox current is maximal for the $Co_{0.73}Ni_{0.27}$ LDH. Therefore, the $Co_{0.73}Ni_{0.27}$ LDH has an optimal characteristic of specific capacitance.

The supercapacitance values estimated from the voltammograms are 380, 511, 899, 663, 452 and 152 $F.g^{-1}$ of $Co_{1-x}Ni_x$ LDHs electrode for the x values 0.0, 0.18, 0.27, 0.51, 0.64 and 1.0, respectively (Table 4.3). It is clear from Fig. 4.8 that, solitary $Ni(OH)_2$ alone shows much lower capacitance than solitary $Co(OH)_2$. The performance of $Co_{1-x}Ni_x$ LDHs for various x values along with specific and interfacial capacitance values is shown in Fig. 4.9. This could helpful for correct correlation in between capacitance and x values of $Co_{1-x}Ni_x$ LDHs. From Fig. 4.9 it was observed that, the combined supercapacitance of $Co_{1-x}Ni_x$ LDHs is much higher than single $Ni(OH)_2$ and $Co(OH)_2$. The $Co_{0.73}Ni_{0.27}$ LDH is found to be suitable combination of $Co_{1-x}Ni_x$ LDHs showed maximum supercapacitance of 899 $F.g^{-1}$. The Fig. 4.9, showed, increased in Ni content to x = 0.27 $Co_{1-x}Ni_x$ LDHs showed increased capacitance. But After that, further increased Ni content to x = 1.0 showed drastic decrease in supercapacitance value of 152 $F.g^{-1}$ up to solitary $Ni(OH)_2$.

The Fig. 4.9 showed graph of both interfacial and specific capacitance values against x (Ni) values in $Co_{1-x}Ni_x$ LDHs. The data revealed that the chemical composition also strongly influences the

electrochemical performance of combined material besides of morphology, valence state and other factors.

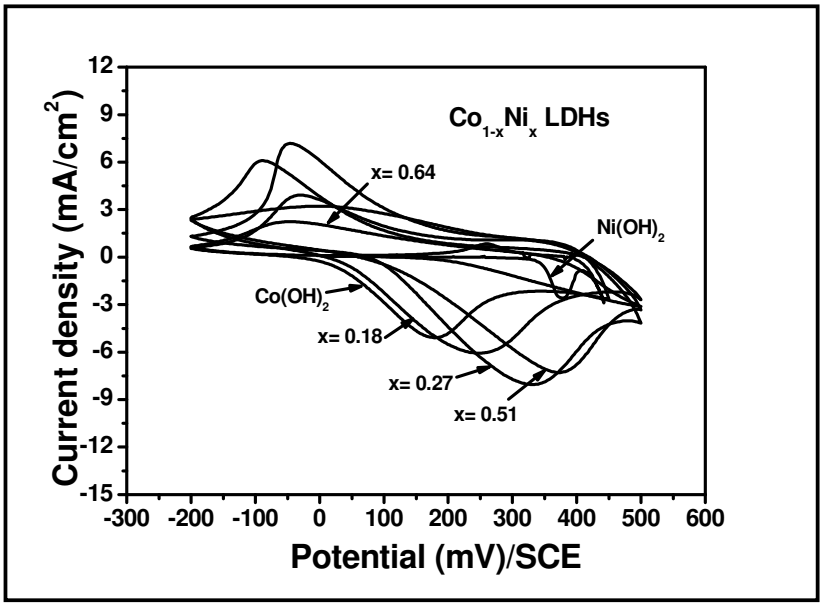


**Figure 4.8:** Cyclic voltammograms at different 'x' (Ni) values in $Co_{1-x}$ $Ni_x$ LDHs thin film electrodes in the 1M KOH electrolyte.

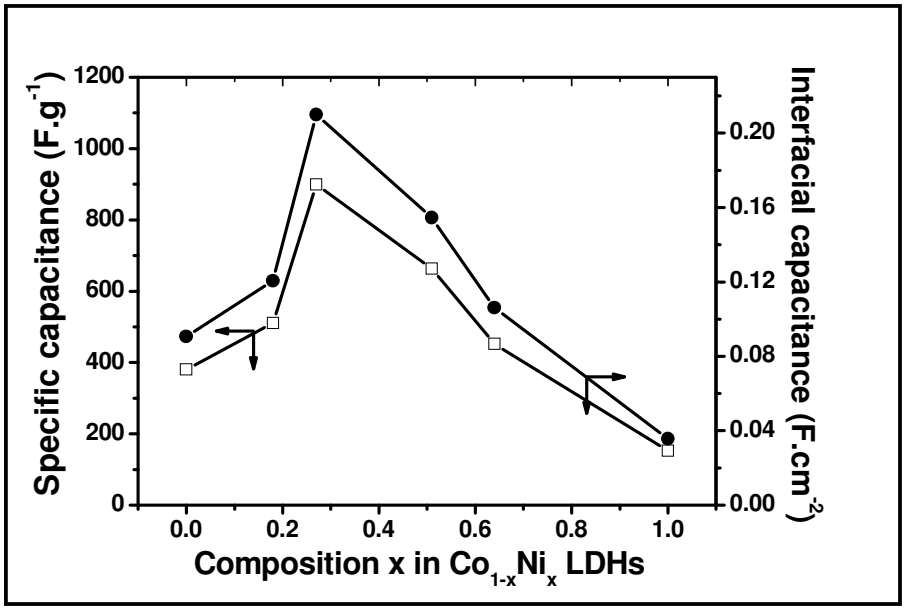


**Figure 4.9** Specific and interfacial supercapacitance at different 'x' (Ni) values in $Co_{1-x}Ni_x$ LDHs film electrodes in 1M KOH at 50 $mV.s^{-1}$ scan rate.

According to this study, chemical composition and deposition method is considered to be the most crucial aspect dealing with the supercapacitance of $Co_{1-x}Ni_x$ LDHs. Since now, only $Co_{0.73}Ni_{0.27}$ LDH film is used for further characterizations.

**Table 4.3 Specific and interfacial capacitances at different 'x' (Ni) values of $Co_{1-x}Ni_x$ LDHs film electrodes.**

| $Co_{1-x}Ni_x$ LDH | Interfacial capacitance ($F.cm^{-2}$) | Specific capacitance ($F.g^{-1}$) |
|---|---|---|
| $Co_{1.0}Ni_{0.0}$ LDH | 0.0906 | 380 |
| $Co_{0.82}Ni_{0.18}$ LDH | 0.1206 | 511 |
| $Co_{0.73}Ni_{0.27}$ LDH | 0.210 | 899 |
| $Co_{0.49}Ni_{0.51}$ LDH | 0.1546 | 663 |
| $Co_{0.36}Ni_{0.64}$ LDH | 0.1062 | 452 |
| $Co_{0.0}Ni_{1.0}$ LDH | 0.0356 | 152 |

### 4.B.3.3 Effect of Electrolyte Concentration:

The concentration effect of KOH electrolyte on supercapacitance of $Co_{0.73}Ni_{0.27}$ LDH electrode was studied at 50 $mV.s^{-1}$ scan rate in the potential range of -200 to +500 mV/SCE. The CVs of $Co_{0.73}Ni_{0.27}$ LDH electrode in KOH electrolyte for different concentrations (0.5 to 2M) is shown in Fig. 4.10. It is observed that, current value under the curve rises with increase in the KOH electrolyte concentration from 0.5 to 2M. The voltammogram of $Co_{0.73}Ni_{0.27}$ LDH showed saturation beyond 2M KOH concentration. The variation of interfacial and specific capacitance with electrolyte concentration at scan rate 50 $mV.s^{-1}$ for $Co_{0.73}Ni_{0.27}$ LDH electrode is shown in Fig. 4.11. The specific and interfacial capacitance values are increased from 728 to 1006 $F.g^{-1}$ and 0.17 to 0.235 $F.cm^{-2}$, respectively, with respect to increased electrolyte concentration from 0.5 to 2M (Table 4.4). As electrolyte concentration increased the current

under curve is also increased resulted into increasing supercapacitance value of $Co_{0.73}Ni_{0.27}$ LDH electrode. This can be ascribed to the increase in $K^+$ ions in the electrolyte. Electrostatic interactions causes ions in electrolyte solution

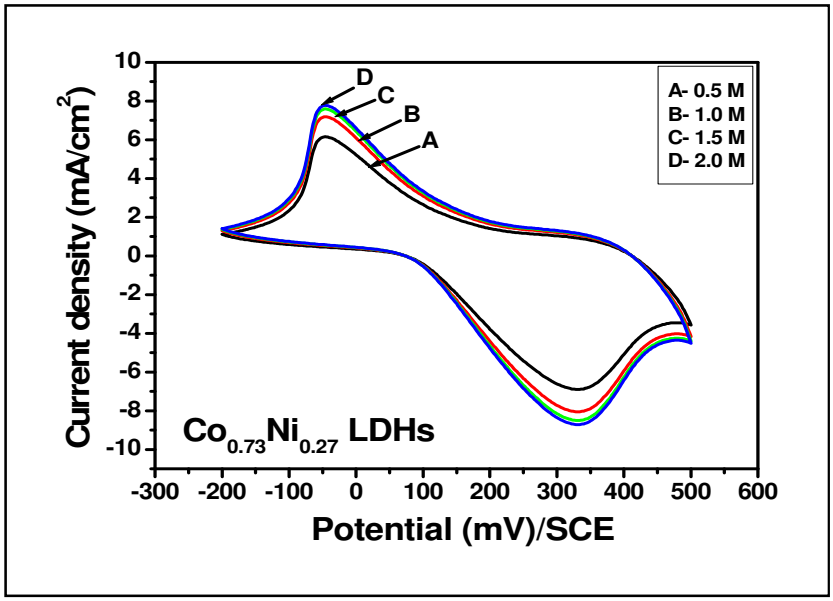


**Fig. 4.10** The CV curves of $Co_{0.73}Ni_{0.27}$ LDH electrode at different KOH electrolyte concentrations at 50 mV.s$^{-1}$.

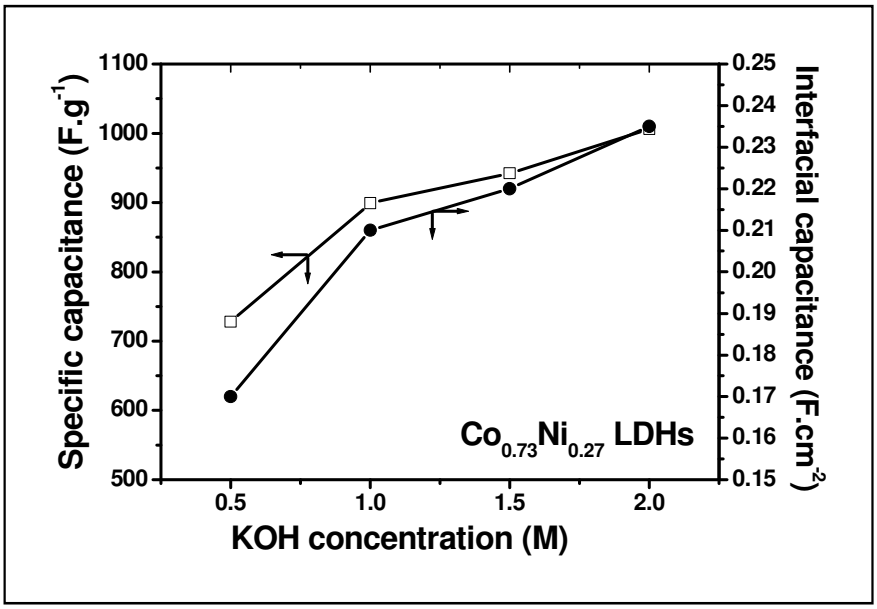


**Fig. 4.11** Variation of specific and interfacial capacitance with KOH concentration at scan rate 50 mV.s$^{-1}$ for $Co_{0.73}Ni_{0.27}$ LDH electrode.

transferred to electrode of opposite polarity to compensate the charge on the electrode due to electric field across the electrodes in electrolyte solution. The specific and interfacial capacitances are increased with increasing the concentration of KOH electrolyte.

**Table 4.4 Effect of electrolyte concentration on interfacial and specific capacitances of $Co_{0.73}Ni_{0.27}$ LDHs.**

| KOH Concentration (M) | $Co_{0.73}Ni_{0.27}$ LDHs | |
|---|---|---|
| | Interfacial capacitance ($F.cm^{-2}$) | Specific capacitance ($F.g^{-1}$) |
| 0.5 | 0.17 | 728 |
| 1.0 | 0.21 | 899 |
| 1.5 | 0.22 | 942 |
| 2.0 | 0.235 | 1006 |

### 4.B.3.4 Effect of Scan Rate:

The voltammetric responses of $Co_{0.73}Ni_{0.27}$ LDH electrode at different scan rates are shown in Fig. 4.12. The effect of the scan rate 5 to 100 $mV.s^{-1}$ on supercapacitor was examined in 2M KOH within voltage range of -200 to +500 mV/SCE. It was found that, the current under curve is progressively increased with increase in scan rate, revealed direct proportion between voltammetric currents and scan rate of voltammograms and hence imply an ideally capacitive behaviour [18].

Variation of specific capacitance and interfacial capacitance values with scan rate is shown in Fig. 4.13. The specific and interfacial capacitance values are decreased from 1023 to 994 $F.g^{-1}$ and 0.239 to 0.232 $F.cm^{-2}$, respectively, with increased scan rate from 5 to 100 $mV.s^{-1}$ (Table 4.5) The decrease in capacitance for higher scan rate can be ascribed to the presence of inner active sites, which cannot precede the

redox transitions completely; possibly because of the diffusion effect of proton within the electrode at higher scan rate of CV.

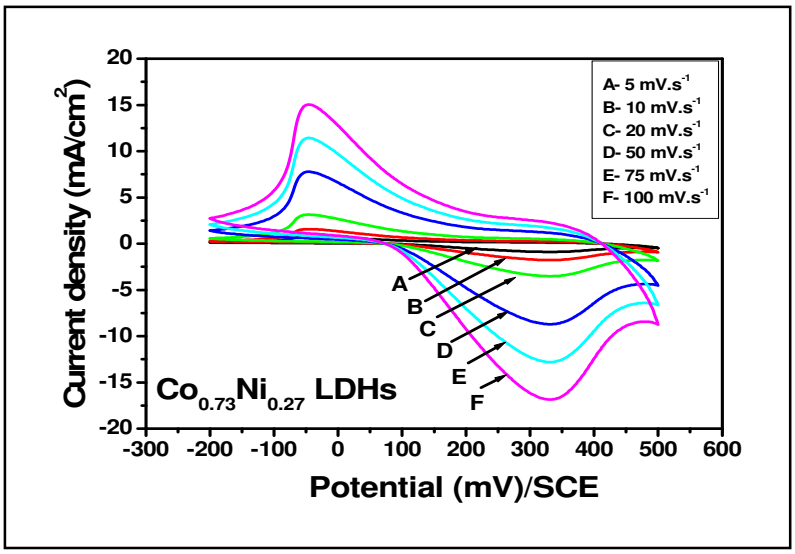


**Fig. 4.12:** The CV curves of $Co_{0.73}Ni_{0.27}$ LDH electrode at different scanning rates in 2M KOH.

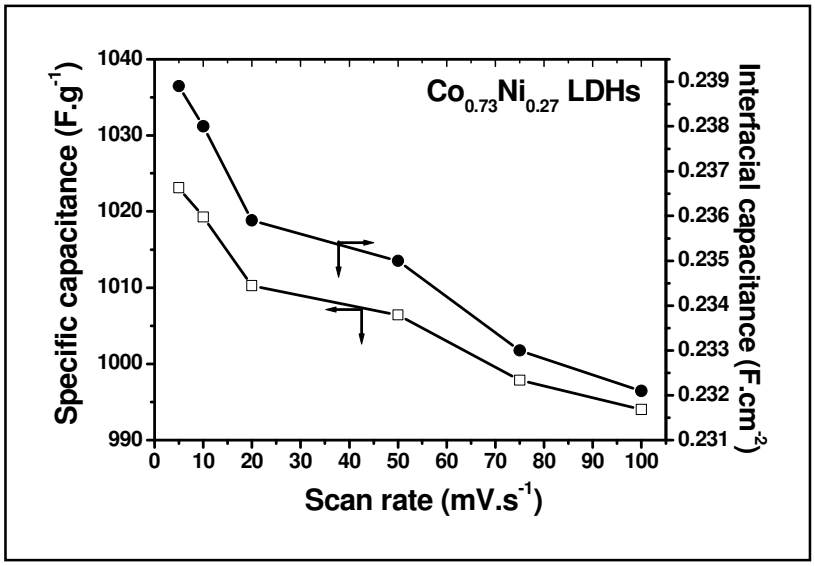


**Fig. 4.13:** Variation of specific and interfacial capacitance with scan rate for $Co_{0.73}Ni_{0.27}$ LDH electrode.

Hence, the specific capacitance obtained at the slowest scan rate is understood to be closest to that of full utilization of the electrode material.

The maximum supercapacitance obtained for $Co_{0.73}Ni_{0.27}$ LDH electrode at 5 $mV.s^{-1}$ scan rate is ~1023 $F.g^{-1}$.

**Table 4.5 Effect of scan rate on interfacial and specific capacitances of $Co_{0.73}Ni_{0.27}$ LDHs.**

| Scan rate ($mV.s^{-1}$) | $Co_{0.73}Ni_{0.27}$ LDHs | |
|---|---|---|
| | Interfacial capacitance ($F.cm^{-2}$) | Specific capacitance ($F.g^{-1}$) |
| 5 | 0.2389 | 1023 |
| 10 | 0.238 | 1019 |
| 20 | 0.2359 | 1010 |
| 50 | 0.235 | 1006 |
| 75 | 0.233 | 997 |
| 100 | 0.2321 | 994 |

### 4.B.3.5 Charge-Discharge Study:

The electrode of $Co_{0.73}Ni_{0.27}$ LDH was used for galvanostatic charge–discharge cycling between 0 and +350 mV/SCE in 2M KOH solution at a current density of 5 $mA.cm^{-2}$. Figure 4.14 shows the characteristic curves of potential variation with cycling time of $Co_{0.73}Ni_{0.27}$ LDH electrode. The redox characteristics in the charge–discharge curves which are directly related to the redox peaks in the CV curves. At the instance of electric current reversing from charging to discharging way, a sharp voltage drop at this high current rate (straight line) can be observed due to the polarization of electrode. Apart from this potential drop, the discharging curve is essentially quite linear. From Fig. 4.14 it is observed that, time periods of charge and discharge are nearly same, which signifies high reversibility and high coulomb efficiency.

The electrical parameters, coulomb efficiency (η%), specific energy (SE) and specific power (SP) are estimated by using equations (3.8), (3.9) and (3.10) in chapter no. 3 (Section 3.B.2.1), respectively. Coulomb efficiency (η%) of $Co_{0.73}Ni_{0.27}$ LDH electrode is found to be ~85 %. The specific energy of 65 Wh/kg and specific power of 1.45 KW/kg indicates significance of $Co_{0.73}Ni_{0.27}$ LDH electrode material for supercapacitor application.

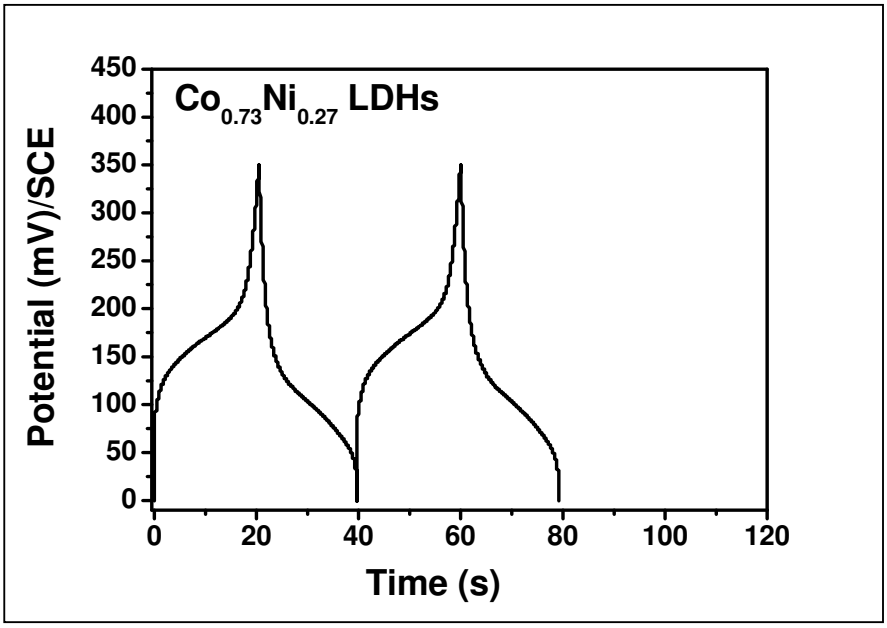


**Figure 4.14:** Galvanostatic charge–discharge curves of $Co_{0.73}Ni_{0.27}$ LDH electrode in 2M KOH electrolyte.

### 4.B.3.6 Electrochemical Impedance Analysis (EIS study):

Electrical conduction and ion transfer were investigated by electrochemical impedance spectroscopy (EIS) analysis. Figure 4.15 illustrated the complex–plane impedance plot of $Co_{0.73}Ni_{0.27}$ LDH electrode also known as Nyquist plot, for $Co_{0.73}Ni_{0.27}$ LDH; where Z' and Z'' are the real and imaginary parts of the impedance, respectively. It consists of a dispersed semi-circle in the higher frequencies, which is related to charge transfer processes (Faradaic reaction kinetics) at the electrode electrolyte

interfaces. And further its transition to a linear part with slope close to 45° along the imaginary axis (Z'') at low frequencies indicates the characteristics of electrode controlled by the diffusive resistivity of the electrolyte due to a Warburg impedance (a limiting diffusion process). And this is not useful for charge storage. Theoretically, the net double-layer capacitance originated from reversible physical sorption must offer a parallel line to the imaginary axis of Nyquist plot [19]. Here, the small deviation of experimental curve from the theoretical approach probably attributed to the different penetration depth of the alternating current signal in virtue of pore size distribution at the electrode arise unusual capacitance [20, 21] and the redox reaction at the $Co_{0.73}Ni_{0.27}$ LDH electrode gives rise to pseudocapacitance.

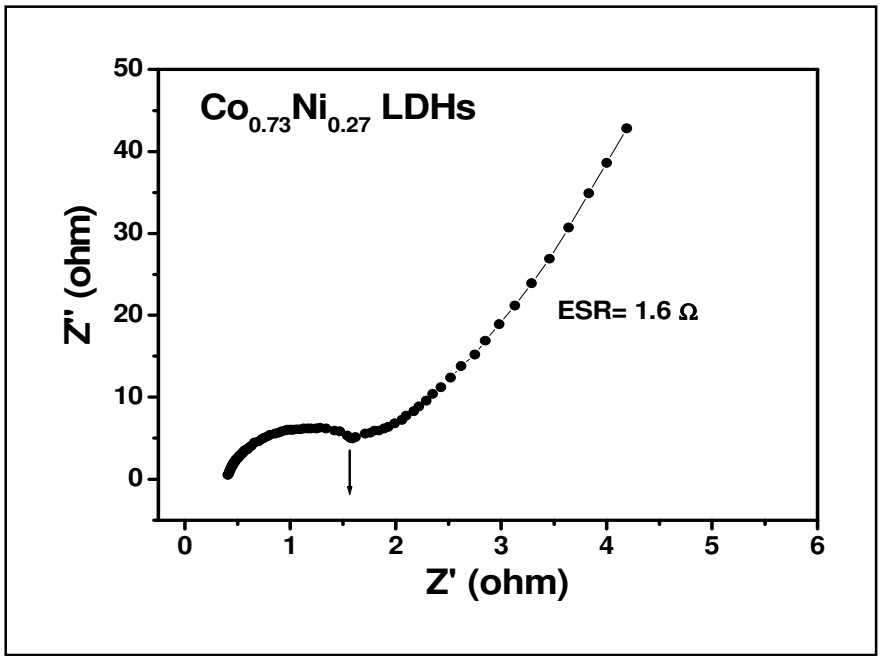


**Figure 4.15:** Nyquist plot of $Co_{0.73}Ni_{0.27}$ LDH electrode in 2 M KOH.

The contact resistance between $Co_{0.73}Ni_{0.27}$ LDH particles and the current collector known as ESR is found 1.6 Ω as shown in the Fig. 4.15. This revealed that thicker nano-flaked morphology leads to the quite high

charge transfer resistance than that of for $Co_{1-x}Ni_x$ LDH deposited poentiodynamically.

### 4.B.3.7 Stability Study:

The stability of $Co_{0.73}Ni_{0.27}$ LDH electrode in 2M KOH was tested by CV. Fig. 4.16 showed the CV curves for 5th and 10000th number cycle.

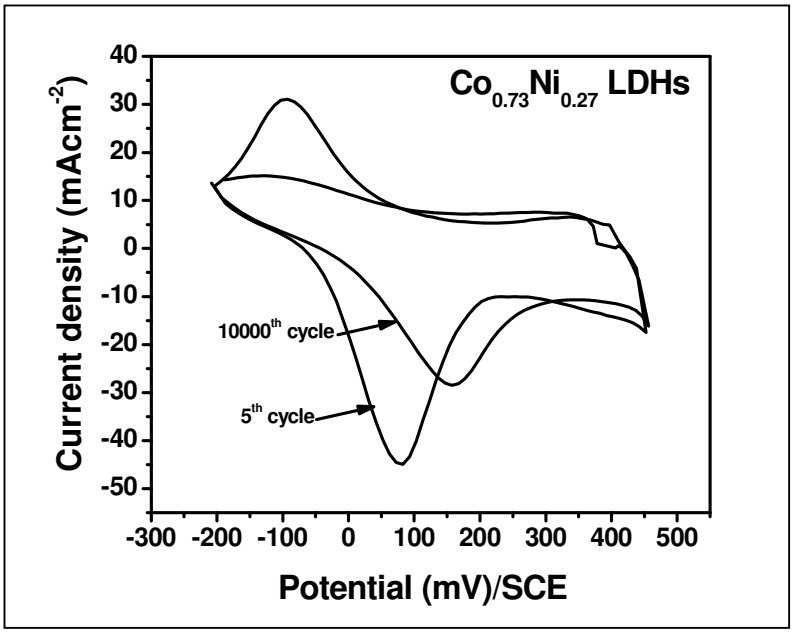


**Fig. 4.16:** Voltamomgrams of $Co_{0.73}Ni_{0.27}$ LDH electrode at scan rate 100 $mV.s^{-1}$ for 5th and 10000th cycles.

The current under curve is decreased by ~ 29% up to 10000 cycles. The 71% stability is retained after 10000th cycles in 2 M KOH at 100 $mV.s^{-1}$. This revealed that, our system can withstand about 10000 cycles without a significant decrease in the capacity, exemplifying the stable nature of $Co_{0.73}Ni_{0.27}$ LDH electrode in energy storage application. Due to the loss of active material, decrement in the specific and interfacial capacitance values with higher number of cycles of $Co_{0.73}Ni_{0.27}$ LDH electrode was observed.

## Conclusions

The current chapter concluded that, the $Co_{1-x}Ni_x$ LDHs electrodes prepared by galvanostatic method showed significant supercapacitor behavior. The thicker microstructured $Co_{1-x}Ni_x$ layered double hydroxides ($Co_{1-x}Ni_x$ LDHs), with various compositions of Co and Ni (in combination $Co(OH)_2$ and $Ni(OH)_2$), has been successfully deposited in the thin film form by galvanotstatic mode. The deposition method changes the emerged morphology of $Co_{1-x}Ni_x$ LDHs films significantly have randomly oriented thicker flakes microstructure. The increase of Ni content in $Co_{1-x}Ni_x$ LDHs for x = 0, 0.18, 0.27, 0.51, 0.64 and 1 affect on emerging surface morphological aspect of the LDHs material films. The $Co_{1-x}Ni_x$ LDHs films showed hydrophilic behaviour. An individual pseudocapacitive performance of $Co(OH)_2$ and $Ni(OH)_2$ is found to be lower than the $Co_{1-x}Ni_x$ LDHs. The supercapacitance value increased with increase in electrolyte concentration and decreased with the scan rate. Maximal specific capacitance for $Co_{1-x}Ni_x$ LDHs electrode was found ~1023 $F.g^{-1}$, attaining specific energy of 65 Wh/kg and specific power of 1.45 KW/kg with ~ 85% of coulomb efficiency for composition $Co_{0.73}Ni_{0.27}$ LDH in 2M KOH electrolyte. The stability of electrode retained to 71% after $10000^{th}$ cycles. Therefore, $Co_{0.73}Ni_{0.27}$ LDH composition is more feasible and found to be potential candidate for supercapacitor application.

**References:**


1 F. Kong, R. Kostecki, F. McLarnon, R.H. Muller, Thin Solid Films, 313 (1998) 775.

2 M. Murthy, G.S. Nagarajan, J.W. Weidner, J.W. Van Zee, J. Electrochem. Soc., 143 (1996) 2319.

3 C.C. Streinz, A.P. Hartman, S. Motupally, J.W. Weidner, J. Electrochem. Soc., 142 (1995) 1084.

4 C.C. Streinz, S. Motupally, J.W. Weidner, J. Electrochem. Soc., 142 (1995) 4051.

5 R. Kostecki, F.R. McLarnon, J. Electrochem. Soc., 144 (1997) 485.

6 M.C. Bernard, M. Keddam, H. Takenouti, P. Bernard, S. Senyarich, J. Electrochem. Soc., 143 (1996) 2447.

7 M.C. Bernard, P. Bernard, M. Keddam, S. Senyarich, H. Takenouti, Electrochim. Acta, 41 (1996) 91.

8 Y. Wang, F. Zhang, S. Xu, X. Wang, D.G. Evans, X. Duan, Ind. Eng. Chem. Res., 47 (2008) 5746.

9 A.C. Scheinost, D.L. Sparks, J. Collod. Interface Sci., 223 (2000) 167.

10 V. Gupta, S. Gupta, N. Miura, J. Power Sources, 175 (2008) 680.

11 K. Nakamoto, Infrared and Raman spectra of inorganic and coordination compounds. New York: Wiley; 1986.

12 A.H. Zimmerman, J. Power Sources, 12 (1984) 233.

13 F. Portemer, A.D. Vidal, M. Figlarz, J. Electrochem. Soc., 139 (1992) 671.

14 G.S. Illia, M. Jobbagy, A.E. Regazzoni, M.A. Blesa, Chem. Mater., 11 (1999) 3140.

15 Y.Y. Liang, S.J. Bao, H.L. Li, J. Solid State Electrochem., 11 (2007) 571.

16 E. Frackowiak, F. Beguin, Carbon, 39 (2001) 937.

17 H.K. Xin, Z. Xiaogang, L. Juan, Electrochim. Acta, 51 (2006) 1289.

18 J.N. Broughton, M.J. Brett, Electrochem. Solid State Lett., 5 (2002) A279.

19 S. Sarangapani, B.V. Tilak, C.P. Chen, J. Electrochem. Soc., 143 (1996) 3791.

20 J.M. Honig, in Electrodes of Conductive Metallic Oxides, S. Trasatti, Editor Elsevier, Amsterdam (1980), Part A, Chap. 1, p. 1.

21 J.W. Long, K.E. Swider, C.I. Merzbacher, D.R. Rolison, Langmuir, 15 (1999) 780.

# CHAPTER V

## Preparation, Characterization and Supercapacitance Evaluation of $Co_{1-x}Ni_x$ LDHs Films Deposited By Potentiostatic Mode

## CHAPTER V

**SECTION (II)**

**SUPERCAPACITIVE EVALUATION OF POTENTIOSTATICALLY DEPOSITED $Co_{1-x}Ni_x$ LDHs THIN FILMS**

## SECTION (I)

## PREPARATION AND CHARACTERIZATION OF $Co_{1-x}Ni_x$ LDHs FILMS DEPOSITED BY POTENTIOSTATIC MODE

### 5.A.1 Introduction:

This chapter deals with the preparation and characterization of $Co_{1-x}Ni_x$ LDHs thin films by potentiostatic mode that is under application of constant voltage. This chapter is divided into two sections. Section (I) covers preparation and characterization of $Co_{1-x}Ni_x$ LDHs thin films via potentiostatic deposition in which effect of composition variation on structural, morphological and wettability properties have been examined. In section (II) the supercapacitive performance of $Co_{1-x}Ni_x$ LDHs thin films have been investigated.

A recent synthesis of $Co_xNi_{1-x}$ LDHs by Gupta et al. via potentiostatic deposition route showed a maximum specific capacitance of 2104 $F.g^{-1}$ [1]. On the other hand, in the case of Co–Al LDHs, a maximum specific capacitance of 684 $F.g^{-1}$ was observed by Wang et al. [2]. Liang et al. obtained a specific capacitance of 479 $F.g^{-1}$ in the case of $Co(OH)_2$–$Ni(OH)_2$/Y-zeolite composites [3]. For related ternary Ni–Co–Al LDHs with Ni/Co = 4:6, prepared using a chemical co-precipitation route by Liu et al. showed a much higher specific capacitance of 960 $F.g^{-1}$ [4]. Hu et al. synthesized $Co_xNi_{1-x}$ LDHs for supercapacitor materials by a simple chemical co-precipitation route using polyethylene glycol as the structure directing reagent [5].

### 5.A.2 Experimental Setup For $Co_{1-x}Ni_x$ LDHs Thin Films Deposition:

The description of experimental setup for deposition of $Co_{1-x}Ni_x$ LDHs thin films is given in the chapter no. 3 (section 3.A.2).

### 5.A.3 Experimental Details:

The potentiostatic electrodeposition of $Co_{1-x}Ni_x$ LDHs thin films were carried out from aqueous precursor solution bath of cobalt and nickel nitrate. In order to deposit $Co_{1-x}Ni_x$ LDHs, molar concentration of cobalt and nickel nitrate precursors were varied from 0.05 M to 0.2 M. The deposition was performed at different constant potentials from -750 to -1100 mV/SCE at various bath temperatures from 300 K to 333 K. Out of which, the room temperature (300 K) deposition carried out in 0.1 M nitrate precursor's solution at constant potential value -900 mV/SCE results smooth, uniform and good quality thin films with high adhesion.

**Table 5.1: Optimized preparative conditions for potentiostatic deposition of $Co_{1-x}Ni_x$ LDHs thin films.**

| Film | $Co_{1-x}Ni_x$ LDHs | | | | | |
|---|---|---|---|---|---|---|
| Medium | Aqueous | | | | | |
| Bath composition | $Co(NO_3)_2.6H_2O$:$Ni(NO_3)_2.6H_2O$ | | | | | |
| | 1.0:0.0 | 0.75:0.25 | 0.60:0.40 | 0.50:0.50 | 0.25:0.75 | 0.0:1.0 |
| Total quantity | 30 ml | | | | | |
| pH | ~6 | | | | | |
| Potential | -900 mV/SCE | | | | | |
| Temperature | 300 K | | | | | |
| Substrate | Stainless steel | | | | | |

The baths were prepared by varying composition of $Co(NO_3)_2$:$Ni(NO_3)_2$ solution as 1.0:0.0, 0.75:0.25, 0.60:0.40, 0.50:0.50, 0.25:0.75 and 0.0:1.0;

for the potentiostatic deposition of $Co_{1-x}Ni_x$ LDHs onto cost effective stainless steel. Table 5.1 showed the optimized preparative parameters for potentiostatic deposition of $Co_{1-x}Ni_x$ LDHs films feasible for supercapacitor application.

### 5.A.4 Results and Discussion:

#### 5.A.4.1 Potentiostatic Deposition of $Co_{1-x}$ $Ni_x$ LDHs and Film Formation:

Chronoamperometry was used to study the electrodeposition process of materials. Based on the voltammetric experiment, it was possible to define a suitable potential to promote potentiostatic deposition of $Co_{1-x}Ni_x$ LDHs thin films. Figure 5.1 presents a current-time transients (potentiostatic curves) for 0.1 M solutions of $Ni(NO_3)_2$, $Co(NO_3)_2$ and $Co(NO_3)_2$ + $Ni(NO_3)_2$ at bath compositions 0.0:1.0, 1.0:0.0 and 0.5:0.5 on stainless steel substrate, respectively during the formation of the $Co_{1-x}Ni_x$ LDHs films on the stainless steel substrate at potential value of -900 mV/SCE. The experimental profiles show typical nucleation and growth features. The ascendant part of current-time transient increases until it reaches a maximum. The initial rise in cathodic current density is due to increased charge transport phenomena known also as space charge activation. With increase in Ni content the cathodic current value increases as shown in Fig 5.1.

The process of electrodeposition occurs by the model of three-dimensional nucleation and growth and that the clusters of the new phase have a slight hump as observed for current-time transient of $Co_{1-x}Ni_x$ LDHs shown in Fig. 5.1. The small amplitude cathodic polarization will uphold the process of surface renewal and further improve the reproducibility of the measurements. However, the experiments in which a large number of nuclei are formed shortly after the beginning of the transient, for these potentiostatic steps an “induction time” is observed. The induction time is

a direct consequence of the need of clusters of ad-atoms to grow to a critical size required for the onset of the new phase [6].

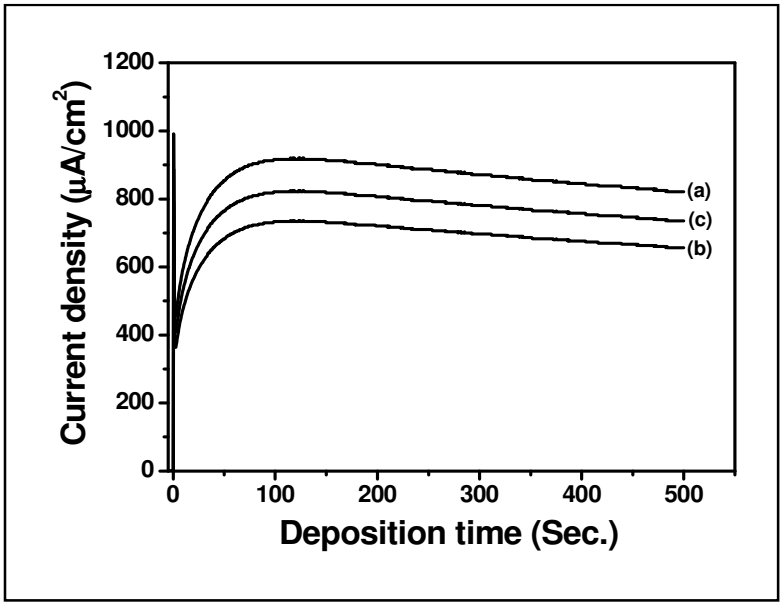


**Figure 5.1** A current-time transients (potentiostatic curves) for 0.1 M solution of (a) $Ni(NO_3)_2$, (b) $Co(NO_3)_2$ and (c) $Co(NO_3)_2$+$Ni(NO_3)_2$ with bath composition 0.0:1.0, 1.0:0.0 and 0.5:0.5 onto stainless steel substrate at potential value of -900 mV/SCE.

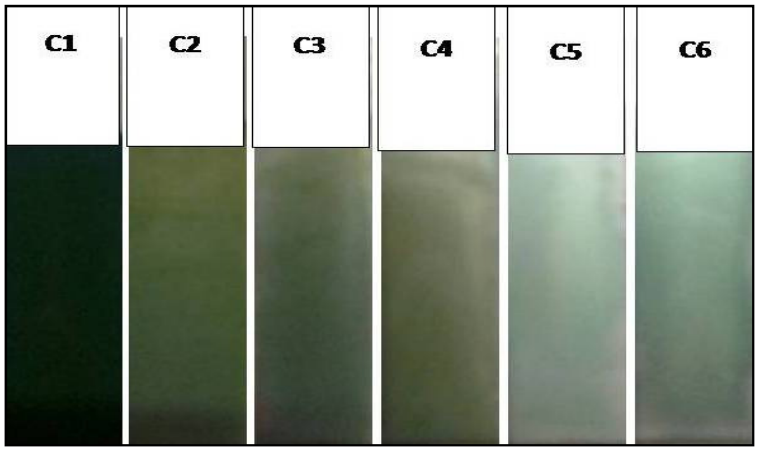


**Fig. 5.2:** Photograph of $Co_{1-x}$ $Ni_x$ LDHs thin films with $Co(NO_3)_2$:$Ni(NO_3)_2$ bath compositions C1 (1.0:0.0), C2 (0.75:0.25), C3 (0.6:0.4), C4 (0.5:0.5), C5 (0.25:0.75), C6 (0.0:1.0).

The gradual decrease in current density after hump can be attributed to the nucleation process of $Co_{1-x}Ni_x$ LDHs film and dominance of mass transport activity. Onwards, time dependent slight current decay is observed in potentiostatic curve as current is diffusion controlled. The nature of current density after nucleation process, implying uniform growth of deposit.

At negative potentials, nitrate ions get reduced on the cathodic surface (stainless steel substrate) to produce hydroxide ions. The generation of $OH^-$ at the cathode increases the local pH and this reaction is helpful for to formation of cobalt-nickel hydroxides via reduction [7].

Therefore, at constant potential value of -900 mV/SCE, the deposition of greenish coloured, uniform and well adherent $Co_{1-x}Ni_x$ LDHs thin film with various compositions were obtained as shown in Fig. 5.2.

**5.A.4.2 Thickness Measurement:**

Figure 5.3 showed shows variation of deposited weight of $Co_{1-x}Ni_x$ LDHs for different bath compositions of $Co(NO_3)_2$:$Ni(NO_3)_2$ solution. The thickness in terms of weight of $Co_{1-x}Ni_x$ LDHs film deposited is carried out at fixed cathodic potential value of -900 mV/SCE for optimized time period of 500 s at room temperature. The thickness varied accordingly bath composition of cobalt and nickel nitrate solutions (from 1.0:0.0 to 0.0:1.0) within range of 0.237 to 0.246 $mg.cm^{-2}$. The maximum thickness obtained for bath composition 1.0:0.0 of $Co_{1-x}Ni_x$ LDHs film i.e. deposition rate of solitary $Co(OH)_2$ is more.

From Fig. 5.3 it is observed that, with increase of the Ni content, thickness in $Co_{1-x}Ni_x$ LDHs film decreased gradually to 0.237 $mg.cm^{-2}$ for 0.25:0.75 molar ratio and again increased for solitary deposition of $Ni(OH)_2$. This implied that, for constant deposition potential and deposition time, the rate of deposition decreases with increasing Ni content for $Co_{1-x}Ni_x$ LDHs excluding solitary deposition of $Ni(OH)_2$.

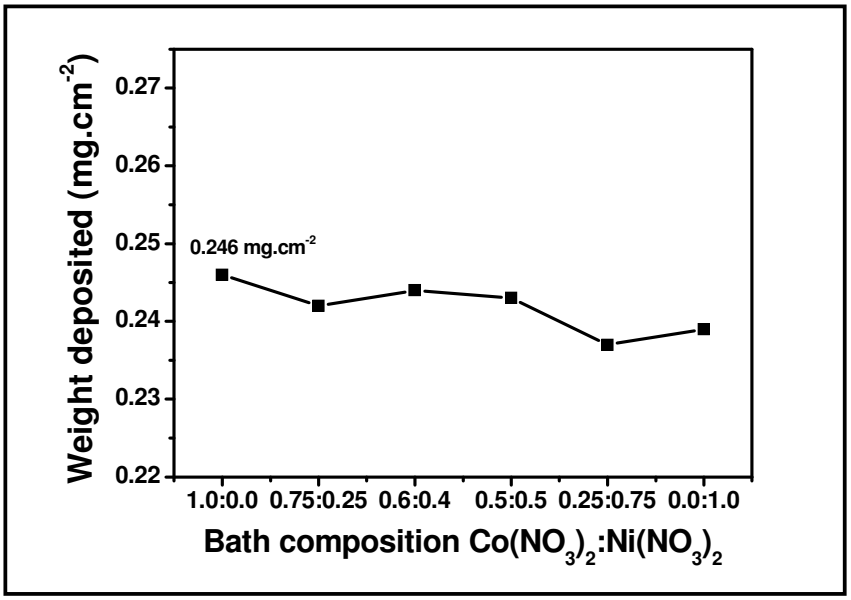


**Figure 5.3:** $Co_{1-x}$ $Ni_x$ LDHs thin film thickness for various bath compositions of $Co(NO_3)_2$:Ni $(NO_3)_2$.

### 5.A.4.3 Structural Characterization:

The X-ray diffraction technique was used for structural analysis of deposited films. The XRD patterns with various compositions of $Co_{1-x}Ni_x$ LDHs films onto stainless steel substrate are shown in Fig 5.4. The diffraction peaks correspond to the characteristic reflections of LDHs materials in the 2θ range 10°-90°, with a series of (00l) peaks arising from the basal reflection appearing as narrow symmetric lines at low angle.

The six peaks in diffraction patterns revealed crystalline nature of the $Co_{1-x}Ni_x$ LDHs thin films, wherein C1 and C6 are individual $Co(OH)_2$ and $Ni(OH)_2$, respectively.

The diffraction peaks are directly linked to good crystallinity of the deposited films of $Co_{1-x}Ni_x$ LDHs. Among them strong diffraction peaks associated with stainless steel substrate are occurred at 2θ values ~50.7° and ~74.60° are indexed with the star. In particular, the peaks appearing at 2θ values of ~12° (7.5 Å), ~34° (2.68 Å), ~43.59° (2.07 Å), ~60° (1.57 Å) are due to the reflections of the planes (001), (100), (101) and (110), respectively; which mutually associates with α-$Co(OH)_2$ and α-$Ni(OH)_2$

formation only in support with JCPDS card no. 74-1057 and 38-0715, respectively [8].

The β-phase of $Co(OH)_2$ and $Ni(OH)_2$ have a lower d-spacing(~ 4.6 Å) than that of α-phase and consistent with a close packing of hydroxide layers. whilst the d-spacing of α-$Co(OH)_2$ and α-$Ni(OH)_2$ and the LDHs samples is greater than 7 Å [9]. It was hard to distinguish between the two phases, since they have similar structures and their diffraction peaks are very close [1].

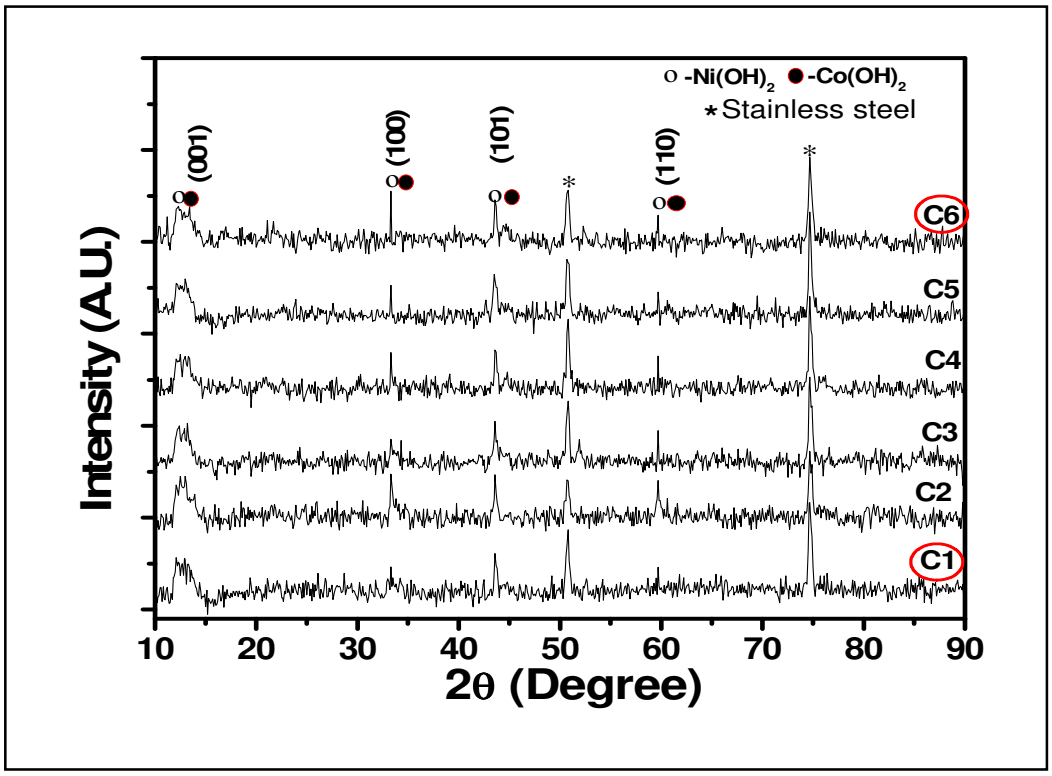


**Figure 5.4:** X-ray diffractograms of $Co_{1-x}Ni_x$ LDHs thin films for various bath compositions of $Co(NO_3)_2$:$Ni(NO_3)_2$ on stainless steel substrate.

### 5.A.4.4 FT-IR study:

The FT-IR absorption spectra of $Co_{1-x}Ni_x$ LDHs thin films is additional support to XRD study within range 4000–400 $cm^{-1}$ as shown in Fig. 5.5.

In the spectra C1 (1.0:0.0), C4 (0.5:0.5) and C6 (0.0:1.0); peak around 3420 $cm^{-1}$ is a characteristic of O-H stretching vibrations of inter layer water molecules within the deposited hydroxides. A sharp peak centered at around 3140 $cm^{-1}$ is attributed to O-H stretching mode of the free M-OH (here in M=Ni/Co) groups [10, 11]. The peak at 1650 $cm^{-1}$ corresponds to bending vibration of molecular water. The band around 1378 $cm^{-1}$ is characteristics of interlayer $NO_3^-$ anions stretching [12]. The origination of small peaks at 780, 556 and 468 $cm^{-1}$ due to stretching vibration of Ni-O in C6. The band at 498 $cm^{-1}$ can be attributed to δ(OH) vibration [13, 14]. Whereas, occurrence of band at 436 $cm^{-1}$ corresponds to stretching vibration Co-O in C1. Both the characteristic bondings were found in C4 sample spectrum [15]. Hence, obtained FT-IR spectra showed typical features of α-$Co(OH)_2$ and α-$Ni(OH)_2$ in the potentiostatic deposit.

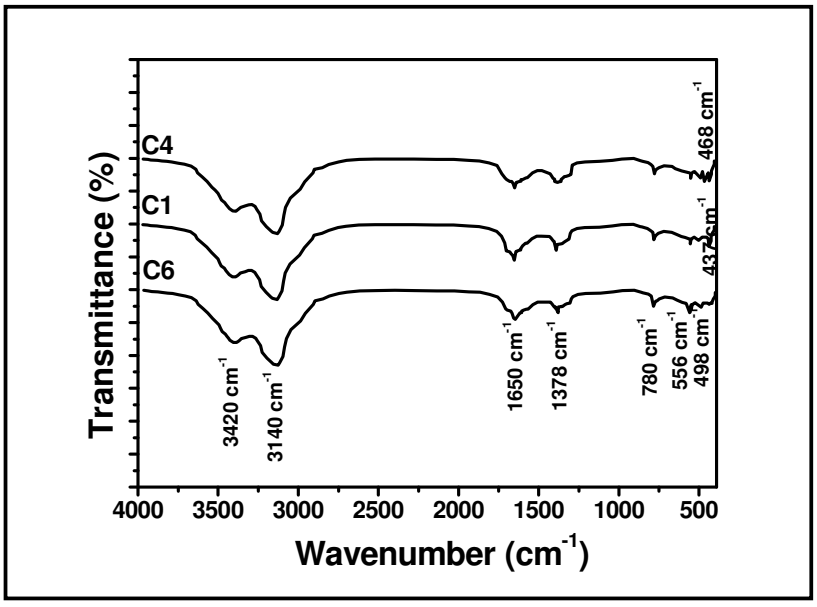


**Figure 5.5:** FT-IR spectra of $Co_{1-x}Ni_x$ LDHs for A1 (1.0:0.0), A4 (0.5:0.5) and A6 (0.0:1.0) bath compositions of $Co(NO_3)_2$:$Ni(NO_3)_2$.

### 5.A.4.5 Surface Morphological (SEM) and Compositional Studies (EDS):

The surface morphologies of the $Co_{1-x}Ni_x$ LDHs thin films were investigated by scanning electron microscopy (SEM) and the micrographs

of various bath compositions at ×50,000 magnifications are shown in Fig. 5.6 (C1-C6). From the SEM micrographs it is clearly observed that, the $Co_{1-x}Ni_x$ LDHs with various compositions have major impact on the resulting morphology.

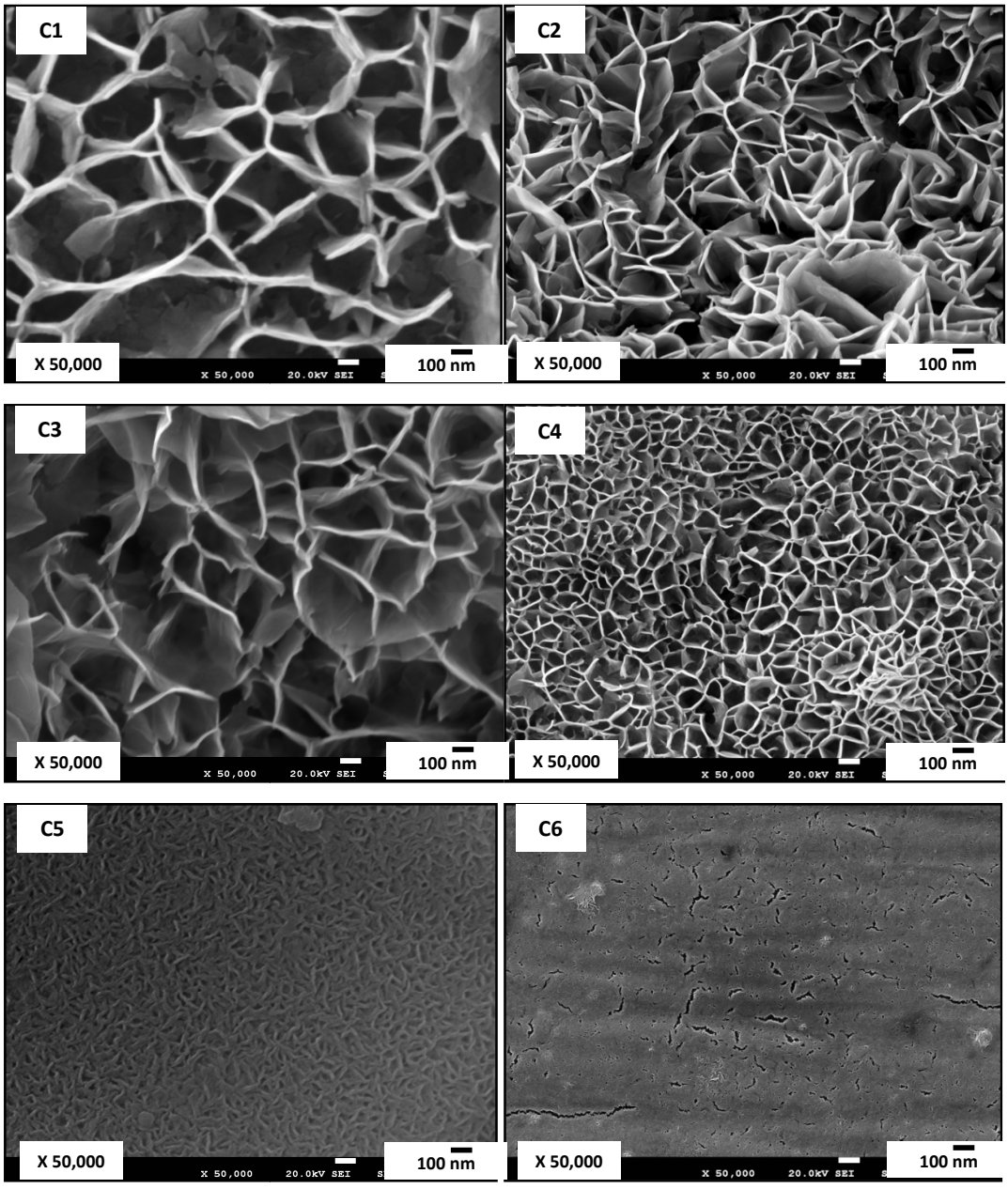


**Figure 4.A.6:** SEM micrographs of $Co_{1-x}Ni_x$ LDHs thin film for samples C1 (1.0:0.0), C2 (0.75:0.25), C3 (0.6:0.4), C4 (0.5:0.5), C5 (0.25:0.75) and C6 (0.0:1.0) at X50,000 magnification.

The $Co_{1-x}Ni_x$ LDHs thin films showed composition dependent porous natured microstructure owing nano-flaked flower like morphology. The sample B1 showed more porous morphology of (cobalt hydroxide) with microstructure seized with thicker nano sheets of width~ 35 nm revealed bigger flakes size. There was not significant change observed for sample C2 with increase of Ni proportion in $Co_{1-x}Ni_x$ LDHs. Only the slight decrease in sheet width of nano-flaked walls is noticed. The porosity of sample fairly decreased and some sort of improvement in the grown microstructure was observed.

The sample C2 showed fine and sharp microstructure than C1. However, as Ni content in $Co_{1-x}Ni_x$ LDHs was increased, the growing microstructure get shrink and morphology became more and more compact as shown in Fig. 5.6 (C2-C6).

Sample C5 and C6 were Ni rich compositions of $Co_{1-x}Ni_x$ LDHs showed more compact microstructure and morphology incorporated with collection of bunched flakes. The grown bunched nano-flakes have small flake size with very thinner flake width. For sample C6 (nickel hydroxide) more compact morphology was observed along with some void spaces. The decrease in sheet width of nano-flakes for C1 to C4 was observed from ~ 35 nm to ~ 16 nm. This could support to the conclusion of shrinking and thinning of microstructure with increased Ni content in $Co_{1-x}Ni_x$ LDHs samples. The increased Ni amount may stimulate flakes grown collectively in bunches and merging to form compact microstructure with decrease in the individual size of flakes and flake width.

Thus the results signified that, the Ni content in $Co_{1-x}Ni_x$ LDHs transforms the surface morphological properties of $Co_{1-x}Ni_x$ LDH electrode [1]. Highly porous microstructure is potential candidate for supercapacitor application can offer huge surface area. It squeezes loosely packed structure which is important for the electrolyte ions to access the active

materials in Faradaic reaction, which may contribute to improve of capacitive performance.

**Table 5.2: EDS analysis of Co, Ni in potentiostatically deposited $Co_{1-x}Ni_x$ LDHs, for various compositions of $Co(NO_3)_2$ and $Ni(NO_3)_2$.**

| Sample | Co:Ni | Co (at%) | Ni (at%) | (x) in $Co(OH)_2]_{1-x}[Ni(OH)_2]_x$ |
|---|---|---|---|---|
| C2 | 0.75:0.25 | 57.74 | 9.83 | 0.14 |
| C3 | 0.60:0.40 | 58.34 | 11.93 | 0.17 |
| C4 | 0.50:0.50 | 38.59 | 24.22 | 0.39 |
| C5 | 0.25:0.75 | 22.49 | 35.67 | 0.62 |

Table 5.2 showed the atomic percentages (at %) of the elements Co and Ni in $Co_{1-x}Ni_x$ LDHs, obtained by Energy-dispersive X-ray spectroscopy (EDS). The elemental composition specify that the $Co_{1-x}Ni_x$ LDHs are composed of $Co(OH)_2$ and $Ni(OH)_2$ together. From the EDS statistic it is found that, the amount of oxygen (not shown in table) was quite high than the Co and Ni combined. The slightly higher content of oxygen may be due to water of hydration as well as absorbed water [1]. From EDS analysis, the formula of $Co_{1-x}Ni_x$ LDHs would be $[Co(OH)_2]_{1-x}[Ni(OH)_2]_x$ with x= 0, 0.14, 0.17, 0.39, 0.62 and 1, found from the potentiostatic deposition of $Co(NO_3)_2$:$Ni(NO_3)_2$ solutions for compositions 1.0:0.0, 0.75:0.25, 0.60:0.40, 0.50:0.50, 0.25:0.75 and 0.0:1.0 for samples C1 to C6, respectively.

### 5.A.4.6 Surface Wettability Study:

Figure 5.7 showed the photographs of water contact with the $Co_{1-x}Ni_x$ LDHs thin films. From Fig. 5.7 (a) it is clearly seen that for samples C1 to C4, water drop set entirely flat, get spread and quite absorbed by $Co_{1-x}Ni_x$ LDHs film surface due to the porous or open microstructure. The samples C1-C4 showed superhydrophilic behaviour with water contact angle < 5° by wetting of $Co_{1-x}Ni_x$ LDHs film surface. Further for Ni rich

samples C5 and C6 resting of water drop was observed having water contact angle of 12˚ and 17˚, respectively as shown in Fig. 5.7 (b, c).

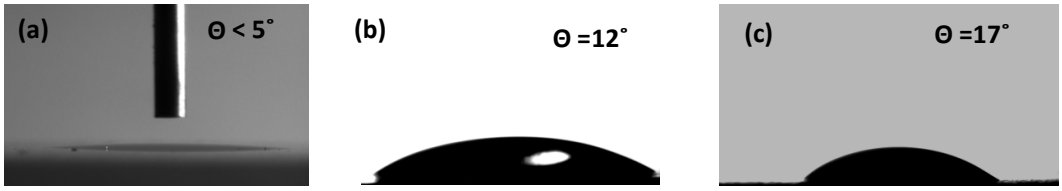


**Figure 5.7:** Measurement of water contact angle of $Co_{1-x}Ni_x$ LDHs samples (a) C1 (1.0:0.0), C2 (0.75:0.25), C3 (0.60:0.40), C4 (0.50:0.50), (b) C5 (0.25:0.75) and (c) C6 (0.0:1.0).

The increase in water contact angle values can be incorporated attributed to nanosized and compact structure of the $Co_{1-x}Ni_x$ LDHs samples. In general surface wettability study depicted superhydrophilic behaviour of $Co_{1-x}Ni_x$ LDHs films, which possess high surface energy and enhances with decrease in particle size. Superhydrophilicity of the $Co_{1-x}Ni_x$ LDHs films can also be linked with hydrous nature of layered hydroxides films. Hydrous bonding on the substrate surface also basis for superhydrophilic nature. Therefore, we observed that increase in Ni proportion in $Co_{1-x}Ni_x$ LDHs can lead to slight increase in contact angle values. Superhydrophilic $Co_{1-x}Ni_x$ LDHs films are appropriate for supercapacitive application in which access of aqueous electrolyte ions to electrode surface occurs easily.

## SECTION (II)

## SUPERCAPACITIVE PERFORMANCE OF POTENTIOSTATICALLY DEPOSITED $Co_{1-x}Ni_x$ LDHs THIN FILMS

### 5.B.1 Introduction:

In this current effort, $Co_{1-x}Ni_x$ LDHs thin films have been successfully deposited by potentiostatic mode and used as supercapacitor electrodes. Effect of electrolyte concentration and scan rate on supercapacitance of $Co_{1-x}Ni_x$ LDHs electrodes has been examined along with stability, charging–discharging and impedance characteristics.

### 5.B.2 Experimental Particulars and Supercapacitance Evaluation:

#### 5.B.2.1 Experimental Set Up for Supercapacitor Study:

The description of experimental setup for supercapacitance study of $Co_{1-x}Ni_x$ LDHs thin films is given in the chapter no. 3 (section 3.B.2.1).

### 5.B.3 Results and Discussion:

#### 5.B.3.1 Effect of Different Electrolytes:

The details of consequence and basic needs regarding the use of suitable electrolyte were described in the previous chapter no. 3 (Section 3.B.3.1). The aqueous KOH electrolyte is used, which attained the maximum current than that of other electrolytes. Therefore, KOH electrolyte is used for further study of supercapacitive properties of $Co_{1-x}Ni_x$ LDHs thin films.

#### 5.B.3.2 Supercapacitance of $Co_{1-x}Ni_x$ LDHs Film:

Fig. 5.8 showed typical cyclic voltammograms of potentiostatically deposited $Co_{1-x}Ni_x$ LDHs electrode for various x values (x= 0.0 to 1.0) in aqueous 1M KOH electrolyte at scan rate of 50 $mV.s^{-1}$ within optimized potential window of -200 to +500 mV/SCE. All voltammograms showed

two strong redox peaks characteristic due to Faradaic reactions of $Co(OH)_2$ and $Ni(OH)_2$ reveals pseudocapacitive behaviour of $Co_{1-x}Ni_x$ LDHs [3, 16].

Fig. 5.8 clearly indicated the shifts in the redox peaks in accordance with composition of the $Co_{1-x}Ni_x$ LDHs. The redox peaks get shifted towards more positive potential values with increase of Ni content in $Co_{1-x}Ni_x$ LDHs within specified voltage range. It can be seen that, the oxidation and reduction peaks for the $Co_{0.86}Ni_{0.14}$ LDH are at ~ +200 mV/SCE and +10 mV/SCE, respectively, whereas for the $Co_{0.38}Ni_{0.62}$ LDH, the peaks are at +380 mV/SCE and +220 mV/SCE for the oxidation and reduction reactions, respectively. The quasi-reversible electron transfer process is observable in all CV curves, indicating that the measured capacitance is mainly based on redox mechanism [17]. The integral area and redox current is maximal for the $Co_{0.83}Ni_{0.17}$ LDH. Therefore, the $Co_{0.83}Ni_{0.17}$ LDH has an optimal characteristic of specific capacitance.

The recorded voltammograms provide a measure of a supercapacitor's charge-response with changing voltage and is a measure of evaluating capacitance. The supercapacitance values estimated from the voltammograms are 1321, 1294, 1513, 1235, 584 and 686 $F.g^{-1}$ of $Co_{1-x}Ni_x$ LDHs electrode for the x values 0.0, 0.14, 0.17, 0.39, 0.62 and 1.0, respectively (table 5.3). It is clear from Fig. 5.8 that, solitary $Ni(OH)_2$ alone shows lower capacitance than that of solitary $Co(OH)_2$. The performance of $Co_{1-x}Ni_x$ LDHs for various x values along with specific and interfacial capacitance values is shown in Fig. 5.9. This could helpful for correct correlation in between capacitance and x values of $Co_{1-x}Ni_x$ LDHs. From Fig. 5.9 it was observed that, the combined supercapacitance of $Co_{1-x}Ni_x$ LDHs is much higher than individual $Ni(OH)_2$ and $Co(OH)_2$. The $Co_{0.83}Ni_{0.17}$ LDH is found to be suitable combination of $Co_{1-x}Ni_x$ LDHs showed highest supercapacitance of 1513 $F.g^{-1}$. The increased in Ni proportion to x = 0.14 in $Co_{1-x}Ni_x$ LDHs showed decrease in capacitance. But After that, further

increased Ni content to x = 0.17 showed drastic increase in supercapacitance value of to 1513 $F.g^{-1}$.

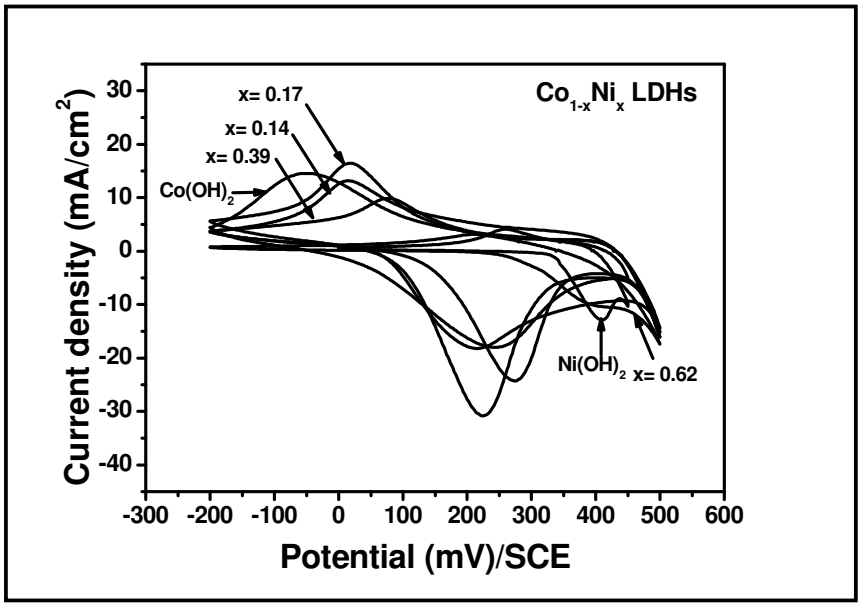


**Figure 5.8:** Cyclic voltammograms at different 'x' (Ni) values in $Co_{1-x}Ni_x$ LDHs thin film electrodes in the 1M KOH electrolyte.

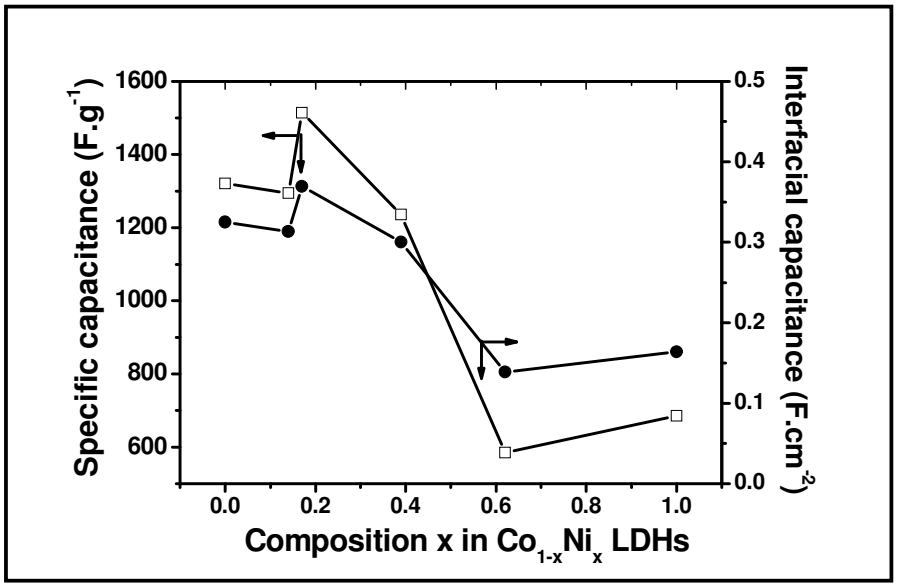


**Figure 5.9** Specific and interfacial supercapacitance at different 'x' (Ni) values in $Co_{1-x}Ni_x$ LDHs film electrodes in 1M KOH at 50 $mV.s^{-1}$ scan rate.rate.

While next to it up to x= 0.62 capacitance decreased drastically to value 584 $F.g^{-1}$. But solitary $Ni(OH)_2$ showed quite higher value of supercapacitance 686 $F.g^{-1}$.

The Fig. 5.9 showed graph of both specific and interfacial capacitance values versus x (Ni) values in $Co_{1-x}Ni_x$ LDHs. The data showed that the chemical composition also strongly influences the electrochemical performance of combined material besides of morphology, valence state and other factors. According to this study, chemical composition is considered to be the most crucial aspect dealing with the supercapacitance of $Co_{1-x}Ni_x$ LDHs. Since now, only $Co_{0.83}Ni_{0.17}$ LDH film is used for further characterizations.

**Table 5.3 Specific and interfacial capacitances at different 'x'(Ni) values in $Co_{1-x}Ni_x$ LDHs film electrodes.**

| $Co_{1-x}Ni_x$ LDH | Interfacial capacitance ($F.cm^{-2}$) | Specific capacitance ($F.g^{-1}$) |
|---|---|---|
| $Co_{1.0}Ni_{0.0}$ LDH | 0.325 | 1321 |
| $Co_{0.86}Ni_{0.14}$ LDH | 0.3112 | 1294 |
| $Co_{0.83}Ni_{0.17}$ LDH | 0.3694 | 1513 |
| $Co_{0.61}Ni_{0.39}$ LDH | 0.3002 | 1235 |
| $Co_{0.38}Ni_{0.62}$ LDH | 0.1386 | 584 |
| $Co_{0.0}Ni_{1.0}$ LDH | 0.164 | 686 |

### 5.B.3.3 Effect of Electrolyte Concentration:

The effect of KOH electrolyte concentration on supercapacitance of $Co_{0.83}Ni_{0.17}$ LDH electrode was studied at 50 $mV.s^{-1}$ sweep rate within the voltage range of -200 to +500 mV/SCE. The voltammograms of $Co_{0.83}Ni_{0.17}$ LDH electrode in KOH electrolyte for different concentrations (0.5 to 2M) is shown in Fig. 5.10. It is found that, current value under the curve

increases with increase in the KOH electrolyte concentration from 0.5 to 2M. The voltammogram of $Co_{0.83}Ni_{0.17}$ LDH showed saturation beyond 2M KOH concentration.

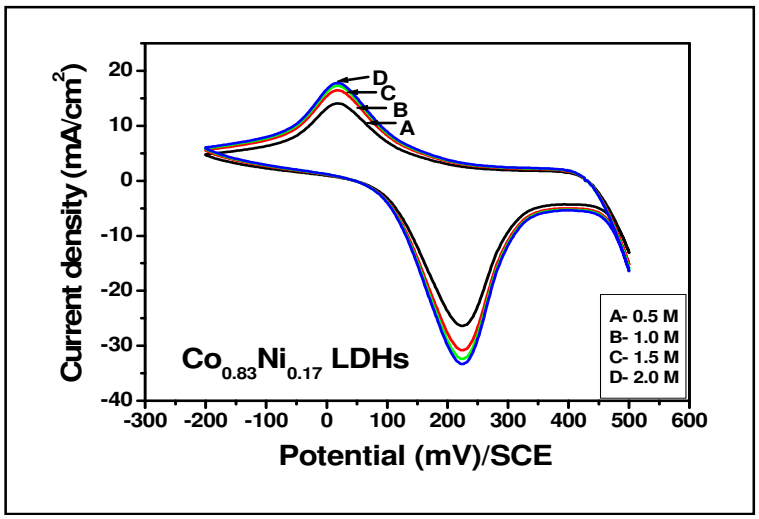


**Fig. 5.10** The CV curves of $Co_{0.87}Ni_{0.17}$ LDH electrode at different KOH electrolyte concentrations at 50 mV.s$^{-1}$.

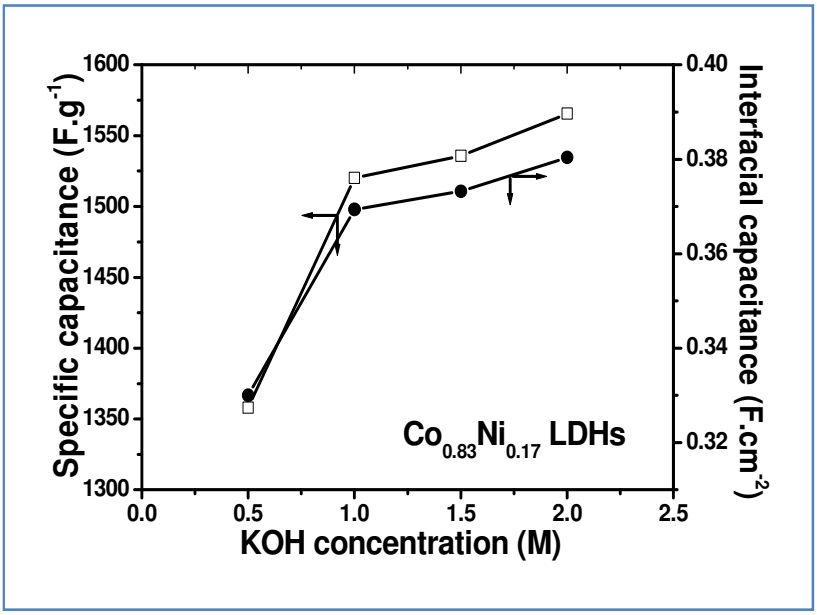


**Fig. 5.11** Variation of specific and interfacial capacitance with KOH concentration at scan rate 50 mV.s$^{-1}$ for $Co_{0.83}Ni_{0.17}$ LDH electrode.

The variation of specific and interfacial capacitance with electrolyte concentration at scan rate 50 $mV.s^{-1}$ for $Co_{0.83}Ni_{0.17}$ LDH electrode is shown in Fig. 5.11. The specific and interfacial capacitance values are increased from 1358 to 1565 $F.g^{-1}$ and 0.33 to 0.38 $F.cm^{-2}$, respectively, in accordance with electrolyte concentration increased from 0.5 to 2M (Table 5.4).

As electrolyte concentration increased, the current under curve is also increased resulted into increasing supercapacitance value of $Co_{0.83}Ni_{0.17}$ LDH electrode. This can be ascribed to the increase in $K^+$ ions in the electrolyte. The applied potential difference across the electrodes in electrolyte solution results in redox reactions and development of charge on of the electrode surface. Electrostatic interactions causes ions in electrolyte solution transferred to electrode of opposite polarity to compensate the charge on the electrode. The specific and interfacial capacitances are increased with increasing the concentration of KOH electrolyte.

**Table 5.4 Effect of electrolyte concentration on interfacial and specific capacitances of $Co_{0.83}Ni_{0.17}$ LDHs.**

| KOH Concentration (M) | $Co_{0.83}Ni_{0.17}$ LDHs | |
|---|---|---|
| | Interfacial capacitance ($F.cm^{-2}$) | Specific capacitance ($F.g^{-1}$) |
| 0.5 | 0.33 | 1358 |
| 1.0 | 0.3694 | 1520 |
| 1.5 | 0.3732 | 1535 |
| 2.0 | 0.3804 | 1565 |

### 4.B.3.4 Effect of Scan Rate:

The voltammetric responses of $Co_{0.83}Ni_{0.17}$ LDH electrode at different scan rates are shown in Fig. 5.12. The effect of the scan rate 5 to 100 $mV.s^{-1}$ on supercapacitor was examined in 2M KOH within voltage range of -200 to

+500 mV/SCE. It was found that the current under curve is progressively increased with increase in scan rate, revealed direct proportion between voltammetric currents and scan rate of voltammograms and hence imply an ideally capacitive behaviour [18].

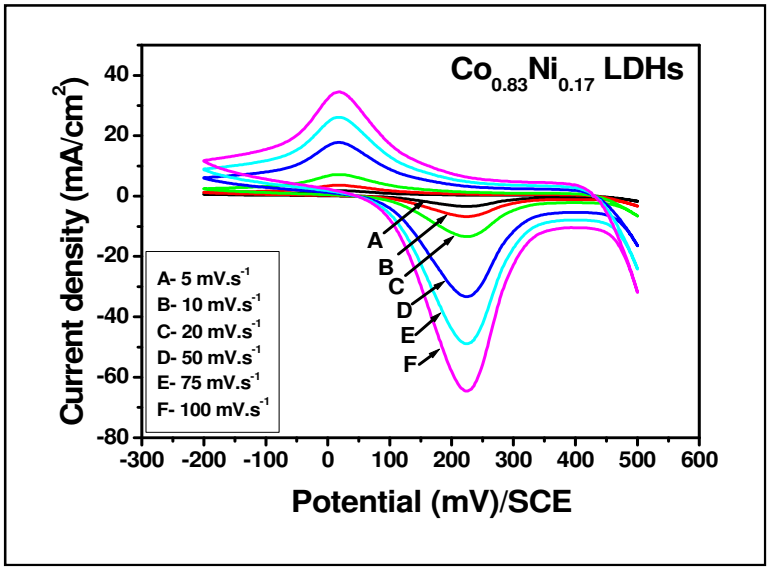


**Fig. 5.12:** The CV curves of $Co_{0.83}Ni_{0.17}$ LDH electrode at different scanning rates in 2M KOH.

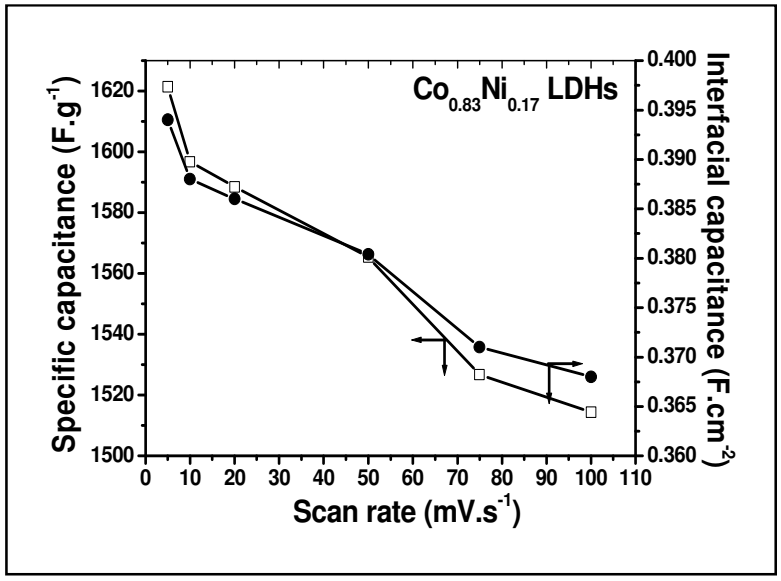


**Fig. 5.13:** Variation of interfacial and specific capacitance with scan rate for $Co_{0.83}Ni_{0.17}$ LDH electrode.

Variation of specific capacitance and interfacial capacitance values with scan rate is shown in Fig. 5.13. The specific and interfacial capacitance values are decreased from 1621 to 1514 $F.g^{-1}$ and 0.394 to 0.368 $F.cm^{-2}$, respectively, with increased scan rate from 5 to 100 $mV.s^{-1}$ (Table 5.5) The decrease in capacitance for higher scan rate can be ascribed to the presence of inner active sites, which cannot precede the redox transitions completely; possibly because of the diffusion effect of proton within the electrode at higher scan rate of CV. Hence, the specific capacitance obtained at the slowest scan rate is supposed to be closest to that of full consumption of the electrode material. The maximum supercapacitance obtained for $Co_{0.83}Ni_{0.17}$ LDH electrode at 5 $mV.s^{-1}$ scan rate is ~1621 $F.g^{-1}$.

**Table 5.5 Effect of scan rate on interfacial and specific capacitances of $Co_{0.83}Ni_{0.17}$ LDHs.**

| Scan rate ($mV.s^{-1}$) | $Co_{0.83}Ni_{0.17}$ LDHs | |
|---|---|---|
| | Interfacial capacitance ($F.cm^{-2}$) | Specific capacitance ($F.g^{-1}$) |
| 5 | 0.394 | 1621 |
| 10 | 0.388 | 1596 |
| 20 | 0.386 | 1588 |
| 50 | 0.3804 | 1565 |
| 75 | 0.371 | 1526 |
| 100 | 0.368 | 1514 |

### 5.B.3.5 Charge-Discharge Study:

The electrode of $Co_{0.83}Ni_{0.17}$ LDH was used for galvanostatic charge–discharge cycling between 0 and +350 mV/SCE in 2M KOH solution at a current density of 5 $mA.cm^{-2}$. Figure 5.14 showed the characteristic curves of potential variation with cycling time of $Co_{0.83}Ni_{0.17}$ LDH electrode. It can

be seen that the charge profile is symmetric and curved, suggesting a pseudocapacitive characteristic. From Fig. 5.14, it is observed that, time periods of charge and discharge are almost the same, which means high reversibility and high coulomb efficiency.

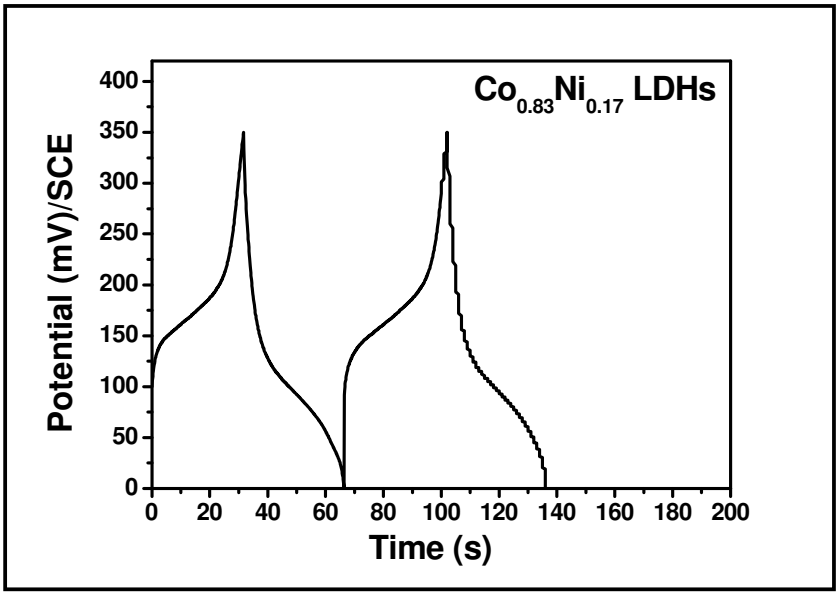


**Figure 5.14:** Galvanostatic charge–discharge curves of $Co_{0.83}Ni_{0.17}$ LDH electrode in 2M KOH electrolyte.

The electrical parameters, coulomb efficiency (η%), specific energy (SE) and specific power (SP) are estimated by using equations (3.8), (3.9) and (3.10), respectively. Coulomb efficiency (η%) of $Co_{0.83}Ni_{0.17}$ LDH electrode is found to be 95.27 %. The specific energy of 141 Wh/kg and specific power of ~1.5 KW/kg indicates significance of $Co_{0.83}Ni_{0.17}$ LDH electrode material for supercapacitor application.

### 5.B.3.6 Electrochemical Impedance Analysis (EIS study):

In order to investigate the electrochemical characteristics of the supercapacitor electrode/electrolyte interface in a quantitative manner, ac impedance spectroscopic measurement was performed. Figure 5.15

showed the respective Nyquist plot of supercapacitor cell assemblies based on the high surface area film of $Co_{0.83}Ni_{0.17}$ LDH in the 1M KOH aqueous solution known as complex-plane plot where Z' and Z'' are the real and imaginary parts of the impedance, respectively. The plot composed of a semi-circle in the higher frequencies, which is related to Faradaic reaction kinetics (charge transfer processes) at the electrode electrolyte interfaces. Further its transition to a linear part with slope close to $45^0$ along the imaginary axis (Z'') at low frequencies is due to a Warburg impedance (a limiting diffusion process) is not useful for charge storage [1].

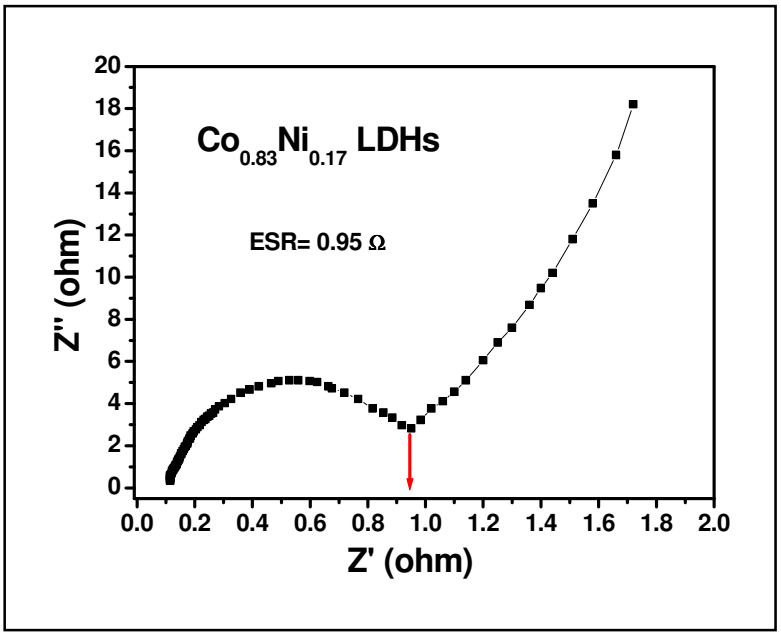


**Figure 5.15:** Nyquist plot of $Co_{0.83}Ni_{0.17}$ LDH electrode in 2M KOH.

According to theory, the net double-layer capacitance originated from reversible physical sorption should offer a parallel line to the imaginary axis of Nyquist plot [19]. Here the slight deviation of experimental curve from the theoretical behaviour possibly ascribed to the different penetration depth of the alternating current signal in virtue of pore size distribution at the electrode arise unusual capacitance [20, 21] and the redox reaction at the $Co_{0.83}Ni_{0.17}$ LDH electrode gives rise to

pseudocapacitance. The contact resistance between $Co_{0.83}Ni_{0.17}$ LDH particles and the current collector known as ESR is found 0.95 Ω. This revealed that thinner nano-flaked morphology offers very low resistance for charge transfer.

### 5.B.3.7 Stability Study:

The stability of $Co_{0.83}Ni_{0.17}$ LDH electrode in 2M KOH was tested by CV. Fig. 5.16 showed the CV curves for 5th and 10000th number cycle.

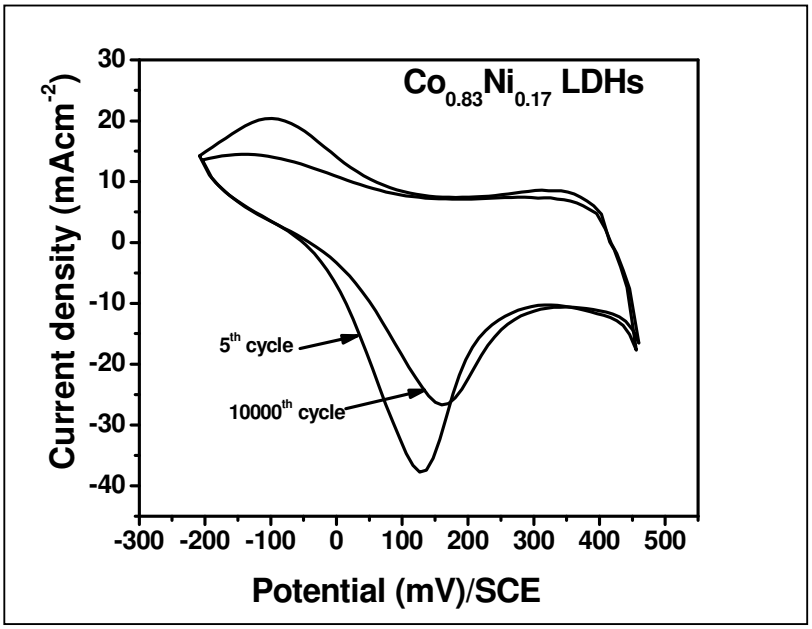


**Fig. 5.16:** Voltammograms of $Co_{0.83}Ni_{0.17}$ LDH electrode at scan rate 100 $mV.s^{-1}$ for 5th and 10000th cycles.

The current under curve is decreased by ~ 20% up to 10000 cycles. Hence, the stability of electrode retained to 80% after 10000th cycles. This revealed that, our system can withstand about 10000 cycles without a significant decrease in the capacity, exemplifying the stable nature of $Co_{0.83}Ni_{0.17}$ LDH electrode in energy storage application. The small decrement in the specific and interfacial capacitance values with higher number of cycles of $Co_{0.83}Ni_{0.17}$ LDH electrode was observed due to the loss of active material.

## Conclusions

The current chapter concluded that the $Co_{1-x}Ni_x$ LDHs electrodes prepared by potentiostatic method show significant supercapacitor behavior. The nanostructured porous $Co_{1-x}Ni_x$ layered double hydroxides ($Co_{1-x}Ni_x$ LDHs), with various compositions of Co and Ni (in combination $Co(OH)_2$ and $Ni(OH)_2$), have been successfully deposited in the thin film form by potentiotstatic mode. The deposition method emerged morphology of $Co_{1-x}Ni_x$ LDHs films significantly have randomly oriented nano-flakes like thinner microstructure. The increase of Ni content in $Co_{1-x}Ni_x$ LDHs for x = 0, 0.14, 0.17, 0.39, 0.62 and 1 affect on emerging surface morphological aspect of the LDHs material films. The $Co_{1-x}Ni_x$ LDHs films showed superhydrophilic behaviour. An individual pseudocapacitive performance of $Co(OH)_2$ and $Ni(OH)_2$ is found to be lower than the $Co_{1-x}Ni_x$ LDHs. The supercapacitance value increased with increase in electrolyte concentration and decreased with the scan rate. Maximal specific capacitance for $Co_{1-x}Ni_x$ LDHs electrode was found ~1621 $F.g^{-1}$, attaining specific energy of 141 Wh/Kg and specific power of 1.5 KW/kg with ~ 95% of coulomb efficiency for composition $Co_{0.83}Ni_{0.17}$ LDH in 2M KOH electrolyte. The stability of electrode retained to 80% after $10000^{th}$ cycles. Therefore, $Co_{0.83}Ni_{0.17}$ LDH composition is more feasible and found to be potential candidate for supercapacitor application.

**References:**


1 V. Gupta, S. Gupta, N. Miura, J. Power Sources, 175 (2008) 680.

2 Y. Wang, W. Yang, S. Zhang, D.G. Evans, X. Duan, J. Electrochem. Soc., 152 (2005) A2130.

3 Y.Y. Liang, S.J. Bao, H.L. Li, J. Solid State Electrochem., 11 (2007) 571.

4 X.M. Liu, Y.H. Zhang, X.G. Zhang, S.H. Fu, Electrochim. Acta, 49 (2004) 3137.

5 Z.A. Hu, Y.L. Xie, Y.X. Wang, H.Y. Wu, Y.Y. Yang, Z.Y. Zhang, Electrochimica Acta, 54 (2009) 2737.

6 B. Scharifker, G. Hills, Electrochim. Acta, 28 (1983) 879.

7 M. Murthy, G.S. Nagarajan, J.W. Weidner, J.W. Zee, J. Electrochem. Soc., 143 (1996) 2319.

8 Y. Wang, F. Zhang, S. Xu, X. Wang, D.G. Evans, X. Duan, Ind. Eng. Chem. Res., 47 (2008) 5746.

9 A.C. Scheinost, D.L. Sparks, J. Collod. Interface Sci., 223 (2000) 167.

10 K. Nakamoto, Infrared and Raman spectra of inorganic and coordination compounds. New York: Wiley; 1986.

11 A.H. Zimmerman, J. Power Sources, 12 (1984) 233.

12 F. Portemer, A.D. Vidal, M. Figlarz, J. Electrochem. Soc., 139 (1992) 671.

13 P.V. Kamath, G.N. Subbanna, J. Appl. Electrochem., 22 (1992) 478.

14 X.M. Ni, Q.B. Zhao, B.B. Li, J. Cheng, H.G. Zheng, Solid State Commun., 137 (2006) 585.

15 G.S. Illia, M. Jobbagy, A.E. Regazzoni, M.A. Blesa, Chem. Mater., 11 (1999) 3140.

16 E. Frackowiak , F. Beguin, Carbon, 39 (2001) 937.

17 H.K. Xin, Z. Xiaogang, L. Juan, Electrochim. Acta, 51 (2006) 1289.

18 J.N. Broughton, M.J. Brett, Electrochem. Solid State Lett., 5 (2002) A279.

19 S. Sarangapani, B.V. Tilak, C.P. Chen, J. Electrochem. Soc., 143 (1996) 3791.

20 J.M. Honig, in Electrodes of Conductive Metallic Oxides, S. Trasatti, Editor Elsevier, Amsterdam (1980), Part A, Chap. 1, p. 1.

21 J.W. Long, K. E. Swider, C.I. Merzbacher, D.R. Rolison, Langmuir, 15 (1999) 780.

# CHAPTER VI

## Summary and Conclusions

In the energy storage field, supercapacitors have greater power density than common batteries and can be deeply discharged without any adverse effect on working life time. And compared to dielectric capacitors, supercapacitors have higher energy density. Thus, supercapacitors are becoming attractive energy storage systems predominantly for applications involving high power requirements. For example, hybrid systems consisting of batteries and supercapacitors are being pursued for electric vehicle propulsion. In such hybrid systems, supercapacitors can provide the peak power during acceleration and therefore, the batteries can be optimized primarily for higher energy density and better cycle life. Supercapacitors are also attractive for many other applications such as power sources for camera flash equipment, lasers, pulsed light generators and as backup power source for computer memory.

Numerous applications are demanding local storage or local generation of electric energy. This may be required in portable or remote equipment, since the supply of power may be interrupted or since the main power supply is not able to deliver the peak power. Local generation of energy by diesel generator, fuel cell, gas turbine, photovoltaic, etc normally means a more complex system than a storage system, but it is most adequate if a large amount of energy is needed for a long time. For this purpose the considerable amount of energy is required in the form of pulse; the conventional capacitor does not satisfy this requirement. So supercapacitors are developed to come to meet the above requirements. In comparison to energy storage and battery systems, which also have high specific energy and power, supercapacitors offer distinct advantages. Supercapacitors have no rotating parts, are very safe device, do not require cooling and other supplementary installations, have a large modularity with respect to voltage and capacitance, low self- discharge, high cycle life, light weight, can be produced at low costs, do not need any servicing and do not contain any environmentally hazardous material.

Supercapacitors can be charged by two different mechanisms: (1) electrical double-layer charging and (2) redox-type charge transfer. In double-layer charging, the electrical charge is stored at the interface between the electrode and electrolyte; thus, such devices are termed electrical double layer capacitors (EDLC). The capacitance of the double layer supercapacitor devices ranges from a few milli-Farads to several Farads per cell. However, to create a workable energy storage device, it is important to further increase the capacities of double layer capacitors. In contrast, redox-type charge transfer arises from reversible Faradaic reactions taking place at the interface between the electrode and electrolyte in an appropriate potential range; these devices are termed pseudocapacitors or redox capacitors. The redox capacitors show higher capacitance than EDLCs due to redox reactions involving exchange of protons, with less emphasis on surface area results in higher utilization of electrode material. The key to increase the energy density of an electrochemical capacitor is to develop electrode materials capable of providing redox reactions. The conducting polymers and metal oxides/hydroxides come under this category. Therefore, metal oxides/hydroxides (of Co, Ni, Fe, Mn, Sn, V, Mo, etc) have long been considered as the most promising materials for supercapacitors. Initially noble metal oxides, such as $RuO_2$ have exhibited prominent properties among various pseudocapacitive materials. Hu et al. reported that the specific capacitance of $RuO_2$ was even as high as 1500 $F.g^{-1}$ in $RuO_2$/AC composite electrode. However, the high cost of Ru has retarded its commercial acceptance as electrode material in electrochemical capacitors. This limitation has encouraged finding other cheaper materials with similar capacitive behaviour to $RuO_2$. Therefore, extensive attempts have been taken to make out substitute and economical electrode materials with suitable electrochemical properties. Late development of

metal hydroxides with high specific capacitances has regenerated great interest in such materials.

Metal hydroxides are often layered materials with large interlayer spacing. They can have very high theoretical specific capacitances. Especially, cobalt and nickel hydroxides have very high potential specific capacitances due to their redox reaction character and layered structures with large interlayer spacing. Bimetallic Co-Ni hydroxide compounds are isostructural with brucite-like cobalt hydroxides, which have been prepared via various methods including coprecipitation, electroprecipitation or homogeneous precipitation. Compared with Co-Fe hydroxides, Co-Ni hydroxides are air stable and can crystallize in a brucite-like phase with continuously variable Ni content; these features make them suitable for studying the oxidative intercalation reaction and for gaining insight into the mechanism. Although nickel-rich Co-Ni LDHs have been prepared from cobalt-substituted nickelate by applying the chimie douce reaction, the synthesis of Co-Ni LDHs with well-developed morphology has not yet been realized. Highly crystallized Co-Ni LDHs are desirable for achieving unilamellar Co-Ni hydroxide nanosheets through exfoliation, which may provide an effective way to improve their electrochemical and catalytic performance. Therefore, applying the oxidative intercalation approach to the Co-Ni hydroxides is of great importance. A recent synthesis of the potentiostatic deposition route showed a maximum specific capacitance of 2104 $F.g^{-1}$. Also Hu et al. prepared $Co_xNi_{1-x}$ LDHs by chemical co-precipitation method and obtained specific capacitance of 1809 $F.g^{-1}$.

Among various physical and chemical deposition methods for thin film preparation, electrodeposition is more advantageous. It enables us to deposit relatively uniform thin films onto large area substrates of complex shape. The interesting feature of electrodeposition is that deposition could

be employed as one of the step in the preparation of oxides or semiconductors. Basically, for the higher specific capacitance value, it is greatly valuable to consider not only the crystallinity and surface properties but also the textural properties of active electrode materials such as surface morphology, surface area, pore volume and pore size. In the point of controlling surface morphology of active materials, electrodeposition method easily make active materials with different morphology by adjusting precursors i.e. addition of foreign elements.

Electrochemical synthesis of hydroxide film is economical and suitable for large-scale applications. It essentially consists metallic or alloyed films are formed with appropriate compositions onto conducting substrates. Keeping this view in mind, the efforts will be given on the electrodeposition and characterization of $Co_{1-x}Ni_x$ LDHs thin films from aqueous medium and finally their use in electrochemical supercapacitors. The different Ni content in $Co_{1-x}Ni_x$ LDHs alters the surface morphology which further improves the pseudo-capacitive property of $Co_{1-x}Ni_x$ LDHs electrode.

The aim of the present study concerns with the synthesis of $Co_{1-x}Ni_x$ LDHs thin films using different modes of electrodeposition method in order to reduce electrode material cost. The work has been distributed in seven chapters. $Co_{1-x}Ni_x$ LDHs films have been deposited using three different modes of electrodeposition i.e. potentiodynamic, galvanostatic and potentiostatic modes from aqueous baths. Different preparative parameters such as deposition potential, current density, deposition time, concentration of electrolyte bath, etc were optimised to get feasible film electrodes for supercapacitor applications. The structural, surface morphological, compositional, wettability properties of $Co_{1-x}Ni_x$ LDHs electrodes were studied and finally these were used as an electrode in supercapacitors.

**CHAPTER I** is the introductory chapter, provides general information about need of power sources, basic terminology of supercapacitor and the need of thin film and thin film supercapacitors. Superiority of electrodeposition method than other methods for deposition of metal hydroxide films is focused. The introduction to layered double hydroxides (LDHs) materials along with literature survey on synthesis and supercapacitor cobalt-nickel LDHs with specific capacitance is involved. The orientation and purpose of the dissertation are stated at the end of the chapter.

Details about the theoretical background of electrodeposition, electrochemical supercapacitors and experimental characterizations techniques are described in **CHAPTER II**. Chapter II is divided into three main sections staring with the introduction of thin film and its classification. In **section I** theoretical background of electrodeposition, basics of electrodeposition along with three different modes of electrodeposition (i.e. Potentiodynamic, Galvanostatic and Potentiostatic modes) have been described. The next **section II** concerned with the characterization techniques, such as, thickness measurement, X-ray diffraction (XRD), FT-IR spectroscopy, scanning electron microscopy (SEM), energy dispersive X-rays spectroscopy (EDS) and surface wettability test.

Thickness of the deposited film was measured in terms of deposited weight per unit area of the films. The structural study was carried out by means of XRD and FT-IR techniques. The morphology of the produced thin films was studied by means of scanning electron microscopy. Surface wettabilty is carried out to study the electrode electrolyte interaction. Surface wettability was studied in terms of contact angle measurement. In **section III**, theoretical aspects of supercapacitors are described.

In **CHAPTER III** potentiodynamic deposition, characterization and supercapacitive properties of $Co_{1-x}Ni_x$ LDHs thin films have been described. This chapter has been divided in two sections. **Section I** deals with preparation of $Co_{1-x}Ni_x$ LDHs thin films from an aqueous medium. Various preparative parameters are optimized to get well adherent and uniform $Co_{1-x}Ni_x$ LDHs films feasible for supercapacitor applications. All the depositions have been carried out using Potentiostat 263A EG and G. Deposition potentials of $Co_{1-x}Ni_x$ LDHs were determined from cyclic voltammetry (CV) curves. The optimized preparative parameters are listed in Table 6.1. The effect of Ni content on structural, morphological, wettability properties of $Co_{1-x}Ni_x$ LDHs films has been studied. The structural investigations from XRD revealed that the formation of nanocrystalline $Co_{1-x}Ni_x$ LDHs thin films on stainless steel substrates. The diffraction peaks in the 2θ range 10°-90° correspond to the characteristic reflections of LDHs materials, with a series of (00l) peaks appearing as narrow symmetric lines at low angle, arising from the basal reflection. the peaks appearing at 2θ values of 12.21° (7.4 Å), 34° (2.65 Å), 43.59° (2.07Å), 60° (1.55Å) are due to the reflections of the planes (001), (100), (101) and (110), respectively; which corresponds to both α-$Co(OH)_2$ and α-$Ni(OH)_2$ formation. On the basis of FT-IR spectra, it is concluded that the potentiodynamic mode results in to the formation of $Co_{1-x}Ni_x$ LDH films. The morphological property showed that surface morphology of the $Co_{1-x}Ni_x$ LDHs electrode strongly dependent on the content of Ni present. The $Co_{1-x}Ni_x$ LDHs possessed the randomly oriented nanoflake like morphology. From the SEM studies revealed that, as Ni proportion in $Co_{1-x}Ni_x$ LDH was increased, the growing morphology become more compact, less porous comprising decrease in flake size along with shrinking flake width. From EDS analysis, the formula of $Co_{1-x}Ni_x$ LDHs would be $[Co(OH)_2]_{1-x}[Ni(OH)_2]_x$ with x= 0, 0.34, 0.46, 0.59, 0.76 and 1, obtained from the deposition carried out in $Co(NO_3)_2$:$Ni(NO_3)_2$ solutions of bath

compositions 1.0:0.0, 0.75:0.25, 0.60:0.40, 0.50:0.50, 0.25:0.75 and 0.0:1.0. Surface wettability in terms contact angle shows the superhydrophilic nature of the films and with increasing Ni content the hydrophilicity decreases. Thus, $Co_{1-x}Ni_x$ LDHs with different 'x' (Ni) significantly affects the surface properties and potentiodynamic mode of electrodeposition is constructive for preparation of large area nanocrystalline, hydrous $Co_{1-x}Ni_x$ LDHs electrodes.

In **Section II** of chapter III the supercapacitive properties of nanocrystalline, hydrous $Co_{1-x}Ni_x$ LDHs thin films have been investigated. The three-electrode configuration systems with platinum as a counter, $Co_{1-x}Ni_x$ LDHs as working and saturated calomel (SCE) as a reference electrode were used. Initially, an electrolyte was optimised among various electrolytes viz. $Na_2SO_4$, NaCl, KCl, $H_2SO_4$, NaOH, KOH, etc. It was observed that $Co_{1-x}Ni_x$ LDHs films show better supercapacitor nature in aqueous KOH electrolyte within the voltage range -200 to +500 mV/SCE. The performances were studied in terms of interfacial and specific capacitances, in order to check effect of electrolyte, scan rate. The electrochemical impedance measurement (in the frequency range $10^5$ to $10^{-2}$ Hz) of $Co_{1-x}Ni_x$LDHs electrode was performed. The impedance measurement was further analyzed by plotting the Nyquist plot.

The effects of Ni content on supercapacitive properties of $Co_{1-x}Ni_x$ LDHs thin films have been investigated. The effect of concentration of electrolyte (0.5 – 2.0 M), scan rate (5 – 100 $mV.s^{-1}$), number of cycles (10000) etc on the supercapacitance values has been studied. The charging and discharging times of $Co_{1-x}Ni_x$ LDHs electrodes were obtained using chronopotentiometry (CP). The values of supercapacitance, specific power, specific energy, coulomb efficiency and electrochemical series resistance of electrodes etc. were calculated using the formulae and the resulting values are enlisted in table 6.2. It is seen that $Co_{0.66}Ni_{0.34}$ LDHs showed maximum supercapacitance value 1102 $F.g^{-1}$ among $Co_{1-x}Ni_x$ LDHs

electrodes. Hence $Co_{0.66}Ni_{0.34}$ LDHs film is used for further characterization. It was observed that, as the concentration of KOH was increased from 0.5 to 2.0 M, the current under the CV curve of $Co_{0.66}Ni_{0.34}$ LDHs electrode was increased and the specific capacitance was increased from 996 $Fg^{-1}$ to 1189 $Fg^{-1}$. As the scan rate was increased from 5 to 100 $mV.s^{-1}$, the current under curve was increased but the specific capacitance was decreased from 1213 to 1164 $F.g^{-1}$. The cycle life i.e. stability studies revealed that the $Co_{0.66}Ni_{0.34}$ LDHs electrode was stable up to 10000 cycles with a slight change in capacitance values. The capacitance retained ratio obtained for $Co_{0.66}Ni_{0.34}$ LDHs is 77%. The specific energy and specific power obtained for $Co_{0.66}Ni_{0.34}$ LDHs is 104 Wh/kg, 1.44 KW/kg and coulomb efficiency 93.87%. The impedance analyses show that the charge transfer resistance is about 1.2 Ω. Thus from the above results it is clear that the $Co_{1-x}Ni_x$ LDHs electrodes are potential candidates showing psuedocapacitive properties with large capacitance.

**CHAPTER IV** deals with the galvanostatic deposition of $Co_{1-x}Ni_x$ LDHs thin films. This chapter is divided into two parts. **Section I** consists of synthesis and characterization $Co_{1-x}Ni_x$ LDHs thin films using galvanostatic mode of electrodeposition. The optimized preparative parameters are listed in Table 6.1 in order to get uniform and well adherent films. The XRD pattern revealed the formation of nanocrystalline $Co_{1-x}Ni_x$ LDHs thin films. The reflections of the planes (001), (100), (101) and (110) are the basis for peaks appearing at 2θ values of ~12° (7.3 Å), ~34° (2.63 Å), ~43.5° (2.07Å), ~60° (1.50Å), respectively; which jointly associates with formation only α-$Co(OH)_2$ and α-$Ni(OH)_2$. The formation of $Co_{1-x}Ni_x$ LDHs thin film was confirmed from the FT-IR spectra. Surface morphological study showed that with increasing Ni content the porosity of $Co_{1-x}Ni_x$ LDHs thin films decreased. $Co_{1-x}Ni_x$ LDHs possess microstructure seized with thicker nano sheets. From EDS analysis, the formula of $Co_{1-x}Ni_x$ LDHs would be $[Co(OH)_2]_{1-x}[Ni(OH)_2]_x$ with x= 0, 0.18,

0.27, 0.51, 0.64 and 1, found from the galvanostatic deposition of $Co(NO_3)_2$:$Ni(NO_3)_2$ solutions with bath compositions 1.0:0.0, 0.75:0.25, 0.60:0.40, 0.50:0.50, 0.25:0.75 and 0.0:1.0. Wettability test revealed that the contact angle increased from 19° to 34° as Ni content increased due to the compact surface of change in microstructres.

**Section II** of **CHAPTER IV** describes the supercapacitive properties of galvanostatically deposited $Co_{1-x}Ni_x$ LDHs thin films. The effects of Ni content on supercapacitive properties of $Co_{1-x}Ni_x$ LDHs thin films were studied. It is seen that $Co_{0.73}Ni_{0.27}$ LDHs showed maximum supercapacitance value 899 $F.g^{-1}$among $Co_{1-x}Ni_x$ LDHs electrodes. Hence $Co_{0.73}Ni_{0.27}$ LDHs film is used for further characterization. The $Co_{1-x}Ni_x$ LDHs thin film showed high electrochemical reversibility of redox transitions within -200 to +500 mV/SCE potential limits. It is seen that the specific capacitance increased with increase in electrolyte concentration from 728 to 1006 $F.g^{-1}$ and decreased with increase in scan rate from 1023 to 994 $F.g^{-1}$ for $Co_{0.73}Ni_{27}$ LDHs electrode. Further stability studies showed that the capacitance retained ratio 71% and coulomb efficiency is 85% which may be due to iR drop. The charge transfer resistance of the $Co_{0.73}Ni_{0.27}$ LDHs calculated from Nyquist plot is found to 1.6 Ω. The supercapacitive results are very less as compared to potentiodynamic mode.

**CHAPTER V** focuses on the potentiostatic deposition of nano $Co_{1-x}Ni_x$ LDHs thin films. This Chapter V contains two sections. **Section I** consists of potentiostatic deposition of $Co_{1-x}Ni_x$ LDHs thin films. The various preparative parameters are optimized in order to get uniform and well adherent films for supercapacitor application. The potentiostatically deposited $Co_{1-x}Ni_x$ LDHs films have been characterized. From the XRD patterns it revealed that $Co_{1-x}Ni_x$ LDHs films on to stainless steel substrate were nanocrystalline. From FT-IR spectra, it is confirmed that the potentiostatic mode results in to the formation of $Co_{1-x}Ni_x$ LDHs films.

Scanning electron micrographs showed that the surface morphology of the $Co_{1-x}Ni_x$ LDHs electrode alters due to Ni content variation. The porosity of $Co_{1-x}Ni_x$ LDHs films decreased with increase in Ni content. From EDS analysis, the formula of $Co_{1-x}Ni_x$ LDHs would be $[Co(OH)_2]_{1-x}[Ni(OH)_2]_x$ with x= 0, 0.14, 0.17, 0.39, 0.62 and 1, found from the potentiostatic deposition of $Co(NO_3)_2$:$Ni(NO_3)_2$ solutions with bath compositions 1.0:0.0, 0.75:0.25, 0.60:0.40, 0.50:0.50, 0.25:0.75 and 0.0:1.0. Surface wettability in terms contact angle shows the superhydrophilic nature of the films and with increasing Ni content the hydrophilicity decreases. Thus, $Co_{1-x}Ni_x$ LDHs with different 'x' (Ni) significantly affects the surface properties and potentiostatic mode of electrodeposition is constructive for preparation of large area nanocrystalline, hydrous $Co_{1-x}Ni_x$ LDHs electrodes.

In **section II** of **CHAPTER V**, nanocrystalline, hydrous $Co_{1-x}Ni_x$ LDHs thin films have been employed as supercapacitor electrode. The effects of Ni content on supercapacitive properties of $Co_{1-x}Ni_x$ LDHs thin films have been investigated. It is seen that $Co_{0.83}Ni_{17}$ LDHs showed maximum supercapacitance value 1513 $F.g^{-1}$ among $Co_{1-x}Ni_x$ LDHs electrodes. Hence $Co_{0.83}Ni_{0.17}$ LDHs film is used for further characterization. $Co_{1-x}Ni_x$ LDHs electrode showed pseudocapacitive behavior within the potential window -200 to +500 mV/SCE. The specific capacitance of $Co_{0.83}Ni_{0.17}$ LDHs increased from 1358 to 1565 $F.g^{-1}$ with increase in electrolyte concentration. Maximum specific capacitance found to be 1621 $F.g^{-1}$ at scan rate 5 $mV.s^{-1}$ for $Co_{0.83}Ni_{17}$ LDHs thin film. The stability study indicates the capacitance retained ration 80%. From galvanostatic charge-discharge it is confirmed that $Co_{0.83}Ni_{0.17}$ LDHs electrode exhibits the higher specific energy with higher specific power, so it can be used as supercapacitive electrode material. The values of specific energy specific power and coulomb efficiency of $Co_{0.83}Ni_{0.17}$ LDHs electrode are enlisted in table 6.2. Impedance analyses showed that the charge transfer resistance value 0.95 Ω.

$Co_{1-x}Ni_xLDHs$ electrode prepared by potentiostatic mode of electrodeposition showed best performance over other modes (i.e. potentiodynamic and galvanostatic).

In **CHAPTER VI,** all the results are summarized from above chapters and conclusions are made. It was concluded that we have successfully employed three different modes of electrodeposition (potentidynamic, galvanostatic and potentiostatic) for the preparation of $Co_{1-x}Ni_x$ LDHs thin films. The results obtained from **CHAPTER III, CHAPTER IV and CHAPTER V** suggest that the supercapacitive properties of $Co_{1-x}Ni_x$ LDHs thin films prepared by potentiostatic mode are most superior to other modes. The reason for such a high supercapacitive properties could be the deposition of $Co_{1-x}Ni_x$ LDHs occurs at constant potential of -900 mV/SCE. In this mode deposition occurs continuously. In the case of potentiodynamic mode, there is a break in the deposition between each potentiodynamic cycle and the deposition is discontinuous. Thus the potentiostatically deposited $Co_{1-x}Ni_x$ LDHs thin films are promising candidates for fabrication of high energy density and high power density supercapacitors.

**Fabrication of supercapacitive models:**

The steps involved in the fabrication of supercapacitive models based on $Co_{1-x}Ni_x$ LDHs electrodes are as follows:

- **Step-I**

For the deposition of $Co_{1-x}Ni_x$ LDHs electrodes the stainless steel (SS) substrates having area 12 $cm^2$ were cleaned as per the procedure given in chapter 3 (section 3.A.3). Overall results suggest that potentiostatically deposited $Co_{1-x}Ni_x$ LDHs electrodes have high supercapacitive properties hence we have chosen same mode of electrodeposition for preparation of electrodes for device fabrication. Following Fig. 6 (a) is the photographs of potentiostatically deposited $Co_{1-x}Ni_x$ LDHs thin films on SS substrates.

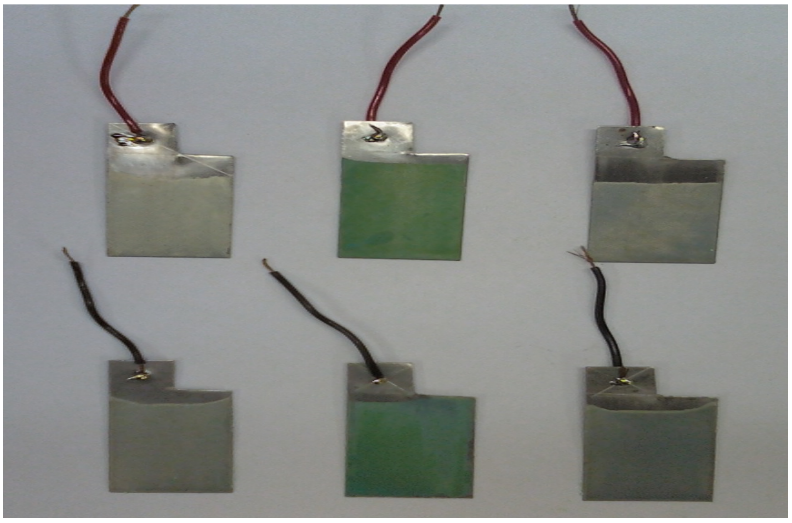

Fig. 6 (a)

- **Step-II**

In step II we make the connections to each film separately by soldering. Such 3 films were stickled by using two sided tape to form two separate bunches of electrodes as shown in the Fig. 6 (b).

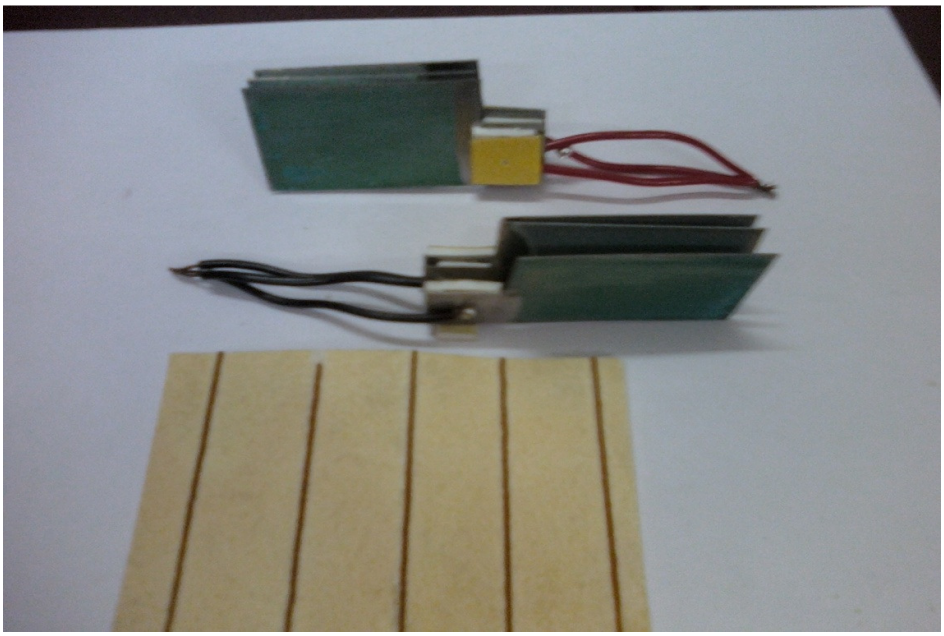

Fig. 6 (b)

Further these two bunches are connected in parallel to increase the capacitance and are separated by polypropylene separator as shown in Fig. 6 (c).

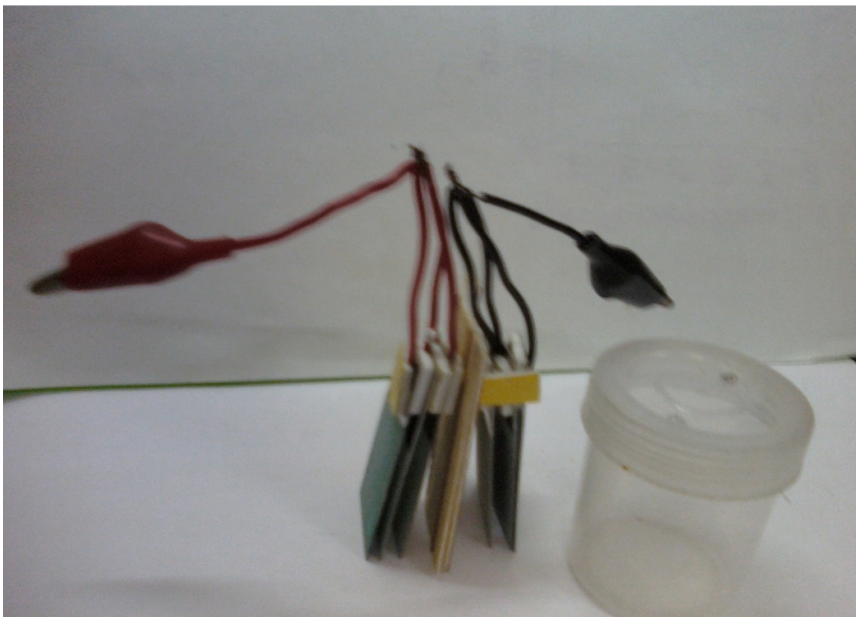

Fig. 6 (c)

Finally this assembly is dipped in plastic container having 2 M KOH as an electrolyte as shown in Fig. 6 (d). Final photograph of the device is as shown in Fig.6 (e).

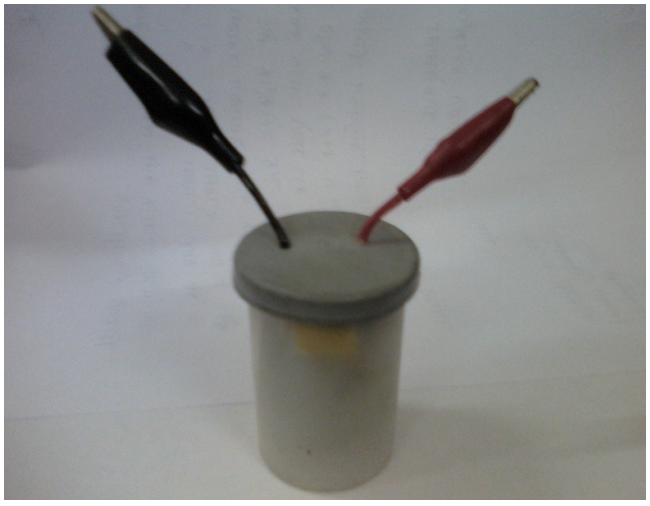

Fig. 6 (d)

Fig. 6 (e)

The maximum supercapacitance achieved by using device was 1296 $F.g^{-1}$.

In order to reduce the size of device deposition of $Co_{1-x}Ni_x$ LDHs thin films on to flexible stainless steel substrates have been carried out.

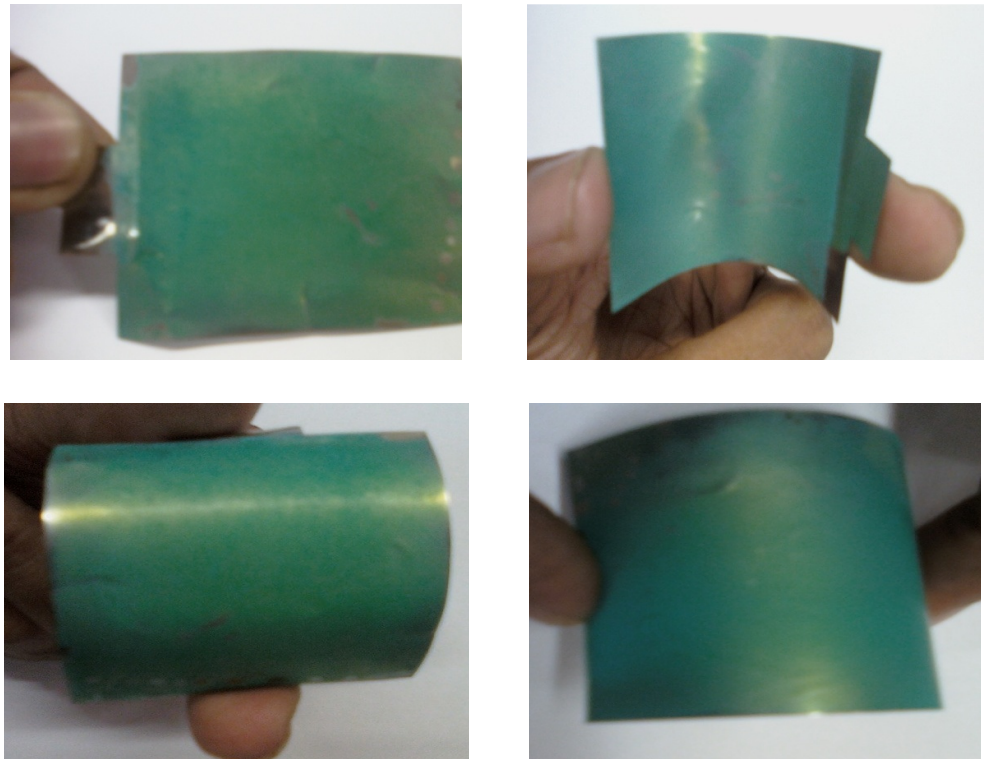

Fig. 6 (f) Photographs of potentiostatically deposited $Co_{1-x}Ni_x$ LDHs thin films on to flexible stainless steel substrates having area 20 $cm^2$

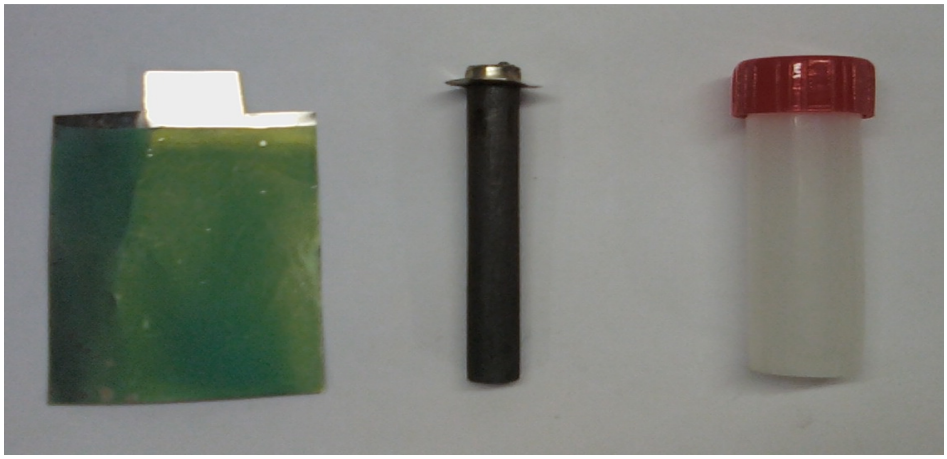

Fig. 6 (g) Photographs of required accessories for the fabrication of device i.e. $Co_{1-x}Ni_x$ LDHs electrode, graphite electrode and plastic container.

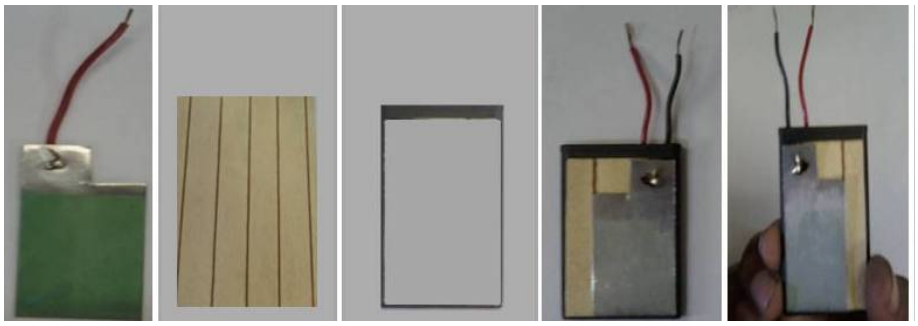

Fig. 6 (h) Photographs of required accessories for the fabrication of device with new model i.e. $Co_{1-x}Ni_x$ LDHs electrode, polypropylene separator and plastic frame.

Fig. 6 (i) Final photographs of supercapacitive model based on potentiostatically deposited $Co_{1-x}Ni_x$ LDHs electrodes

1) In case of symmetric mode (i.e. both cathode and anode is $Co_{1-x}Ni_x$ LDHs electrode) the maximum supercapacitance achieved by using device was 1316 $F.g^{-1}$.
2) In case of asymmetric mode (i.e. cathode is $Co_{1-x}Ni_x$ LDHs film and anode is graphite) the maximum supercapacitance achieved by using device was 1490 $F.g^{-1}$.

**Table 6.1. Optimized preparative parameters of potentiodynamic, galvanostatic and potentiostatic deposition of $Co_{1-x}Ni_x$ LDHs films**

| Sr. No. | Film | $Co_{1-x}Ni_x$ LDHs |
|---|---|---|
| 1 | Medium | Aqueous |
| 2 | Bath composition | $Co(NO_3)_2.6H_2O$ :$Ni(NO_3)_2.6H_2O$ |
| | | 1.0:0.0 |
| | | 0.75:0.25 |
| | | 0.60:0.40 |
| | | 0.50:0.50 |
| | | 0.25:0.75 |
| | | 0.0:1.0 |
| 3 | Total quantity | 30 ml |
| 4 | pH | ~6 |
| 5 | Potential range (mV/SCE) for Potentiodynamic mode | 0 to -1100 |
| 6 | Current density ($mA.cm^{-2}$) for galvanostatic mode | 2 |
| 7 | Potential (mV/SCE) for Potentiostatic mode | -900 |
| 8 | Temperature | 300 K |
| 9 | Substrate | Stainless steel |

**Table 6.2 Supercapacitive properties of $Co_{1-x}Ni_xLDHs$ thin films prepared by potentiodynamic, galvanostatic and potentiostatic modes of electrodeposition**

| **Modes ⟶** | **Potentiodynamic mode** | **Galvanostatic mode** | **Potentiostatic mode** |
|---|---|---|---|
| **Supercapacitive properties ↓** | $Co_{0.66}Ni_{0.34}$ LDHs | $Co_{0.73}Ni_{0.27}$ LDHs | $Co_{0.83}Ni_{0.17}$ LDHs |
| Supercapacitance ($F.g^{-1}$) | 1213 | 1023 | 1621 |
| Specific Energy (Wh/kg) | 104 | 65 | 141 |
| Specific Power (KW/kg) | 1.44 | 1.45 | 1.5 |
| Coulomb efficiency (%) | 94 | 85 | 95 |
| Capacitance retained ratio (%) | 77 | 71 | 80 |
| Impedance (Charge transfer resistance) (Ω) | 1.2 | 1.6 | 0.95 |